AN ULTRAFAST PHOTO-ELECTRON DIFFRACTOMETER

By

Peter Edward Diehr

A dissertation submitted in partial fulfillment
of the requirements for the degree of
Doctor of Philosophy
(Applied Physics)
in The University of Michigan
2009

Doctoral Committee:
Professor Roy Clarke, Co-chair
Emeritus Professor Gérard A. Mourou, Co-chair
Professor Massoud Kaviany
Professor Steven M. Yalisove
Associate Professor David A. Reis

For Della and the future

Acknowledgements

To all the people who helped or encouraged me, thanks! Ibrahim El-Kholy taught me how to build ultrafast electron guns, though we (and it) started out slowly enough. Paul Van Rompay helped for a year and more, both with experimental design and automation, and the management of vacuum chambers and Siamese cats. Paul Fairchild of Creative Machine Works assisted with mechanical design and machining expertise for vacuum systems; he also taught my son Eric how to talk to a block of metal and determine who is to be the master, as well as introducing me to Dan Gorzen of X-Ray and Specialty Instruments. Dan Gorzen has been very helpful with high voltage problems for the electron gun and the microchannel plate detectors. John Nees of CUOS was always friendly and helpful with the laser and optical questions, even the questions that shouldn't need to be asked. Pascal Rousseau of CUOS was very helpful with a number of instrumentation and computer support issues. Professor Eric Essene of Geology and Carl Henderson, John Mansfield, Kai Sun from both locations of the Electron Microbeam Analysis Laboratory were helpful and informative, assisting with equipment used for thin film preparation and their analysis. Codrin Cionca, among other things, helped with making better thin film samples. Vladimir Stoica collected reflectivity data from the platinum films. I also spent some time in enjoyable collaborations with Olivier Dubois, a visitor from France who worked with me at the very beginning. Also Davidé Boschetto of the *Laboratoire d'Optique Appliquée* LOA-ENSTA; we tried his bismuth sample, and together identified a number of improvements required in the system.

Of course this work would not have been possible without my advisors, Professor Roy Clarke and Emeritus Professor Gérard Mourou. They were both inspiring, though in different ways. Roy was very patient, and stuck by me through the good and the bad, especially after a serious illness; even when the transformer of the electron microscope I was repairing "blew up" and Randall Hall had to be evacuated! In the earlier days, I had

more than daily contact with Gérard, who provided both an example of a respected and successful scientist, but also much excellent and direct advice. I wish I had been able to follow more of it; I would have finished much sooner. Also on the committee from the beginning was Professor Peter Pronko, who ran my supervised project and taught this ex-swabbie how to be ultra-high vacuum clean, and even though he has now retired to the Coast Guard Auxiliary, I remember spending much time with him I was starting out. Professor David Reis, who I had as both an instructor and advisor will be missed … he was always available for discussions of items theoretical and experimental. Professor Steve Yalisove has also been a provider of advice and encouragement; as my work has progressed he has had a greater influence, and an indirect provider of laser support. Other faculty members have provided advice and support as well; in particular Professor Steven Rand, Professor Herbert Winful, and Professor Massoud Kaviany. Their support and interest has been much appreciated.

I have only thanked the people with a direct impact on my work, but there are others as well, from Marc Wilcox and Adrian Cavalieri, both members of the Mourou research group when I started, to Joel McDonald and Yoosuf Picard of the Yalisove research group. The staff of Applied Physics and Physics who provided support in their own way: Cyndi D'Agostino McNabb, Charles Sutton, and the redoubtable Ramon Isea-Torres.

And finally let me acknowledge the assistance of my own special corps of helpers, each with a particular skill of value to my project, my children: Christiana (machining and showing me how to do it), Mark (optics and photography and the cutting and pasting of delicate gold mesh), Eric (machine drawings), Sarah (encouragement), Brian (illustrations and animations), Kevin (photography, thin sample preparation and mounting). In addition the boys also helped with vacuum chamber cleaning after an accident introduced rotary pump oil into the main chamber. For all of that and more, thanks!

Table of Contents

List of Tables

List of Figures

List of Appendices

Abstract

AN ULTRAFAST PHOTO-ELECTRON DIFFRACTOMETER

By

Peter Edward Diehr

Co-Chairs: Roy Clarke and Gérard A. Mourou

Ultrafast laser pulses - optical pulses shorter than a picosecond - result in rapid processes occurring at both the surface and the interior of solid materials. Understanding these processes requires ultrafast probes; optical probes (reflectivity, spectral) are suitable for some surface studies, but the tracking of structural changes are well suited to x-ray and electron diffraction. An ultrafast photo-electron diffractometer is a tool for tracking structural changes such as thermal expansion, melting and super-heating, crystal phase changes, ionization, and more.

The design and operation of an ultrafast photo-electron diffractometer is detailed, and its successful operation is demonstrated by sub-picosecond recording of strain in a free-standing polycrystalline platinum film of 9 nm thickness subjected to a fluence of 2 mJ/cm^2 from 150 fs laser pulses. The temporal profile of the relative change of strain is

used to determine corresponding temperatures changes; for the (311) peak an increase of 70 K is noted within 10 ps. The increase in temperature takes place at a very nearly linear 7 K/ps. The (111) peak heats more rapidly, reaching 84 K in 6 ps, and is also nearly linear at 14 K/ps. A temporal relationship is found which connects the phonons in different directions with energy transport: the rate of change of temperature per phonon oscillation period is the same in both directions, indicating that thermalization of phonons in polycrystalline platinum is coupled to the actual vibration rate.

Reflectivity data shows rapid, coherent oscillations, but slower than acoustic phonons. These appear to be connected to the nanoparticle network structure of the ultrathin film; further work is planned to unravel these unexpected results.

A new, in-situ method for the determination of time-zero - when the pump and probe pulses are temporally coincident at the sample - is demonstrated, and shown to be quick, reliable, and precise to within half a picosecond.

Chapter 1

An Ultrafast Photo-Electron Diffractometer

Introduction

Laser pulses with sub-picosecond $\left(\leq 10^{-12} \text{ seconds}\right)$ pulse durations conveniently define the ultrafast time-domain. For reference note that picosecond pulse travels 300 μm per picosecond, which is 375 wave lengths for an 800 nm Ti:Sapphire ultrafast laser; for a 150 femtosecond pulse the length is 45 μm, or about 56 wavelengths. Focusing a 150 fs pulse with 100 microJoules of energy to a modest 200 μm diameter spot size delivers power at 10^{12} W/cm^2, a fluence of over 100 mJ/cm^2. "Ultrashort laser pulses offer high laser intensity and offer precise laser-induced breakdown threshold with reduced laser fluence. The ablation of materials with ultrashort pulses has a very limited heat-affected volume."[1] This is due to the rapid delivery of the pulse energy; the immediate transfer is through coupling of the electromagnetic light field to the electrons of the material, while the relatively massive atomic nuclei and their inner electrons are barely disturbed.

Two-Temperature Model and Molecular Dynamics

Anisimov *et al.*[2] utilizes a macroscopic model for the absorption of an ultrashort laser pulse by a metal surface. This is known as the two-temperature model, and is based upon energy balance and heat flow. The two temperatures refer to the non-equilibrium state of the system, where the electrons are rapidly elevated in temperature while the temperature of the ion cores lags behind. The laser pulse acts primarily through its electric field, and interacts directly with the electron gas of the metal. Since the pulse is so brief, the electrons absorb energy, but do not have time to lose any during the pulse. The resulting electron state has been characterized as plasma, caused by avalanche ionization[3]. The electron plasma is very hot, but the lattice remains at its initial temperature, taking up to several picoseconds to equilibrate. The heat capacity of the electron gas is very low, and as the electrons thermalize they lose energy to the lattice. That is, energy is transferred from the electrons to the phonons of the lattice. This gives a pair of coupled heat equations, which must be solved numerically. This two-temperature model has been implemented using a finite element integration scheme. This model has been successfully used not only with metals, but also with semiconductors[4]. However other channels exist for the loss of the electronic excitation, including ballistic transport of non-thermalized electrons, stress waves[5], and diffusive transport of thermalized electrons into the bulk[6 7].

When the two-temperature model is applied, an electron-phonon coupling parameter is required. Fitting the results of ultrafast diffraction studies by means of the Debye-Waller relation (see appendices) or ultrafast reflectivity measurements[8 6] can obtain this function.

Zhigilei incorporates the two-temperature model as an extension of molecular dynamics code: “where C and K are the heat capacities and thermal conductivities of the electrons and lattice as denoted by subscripts e and ℓ, and G is the electron-phonon coupling constant. The two-temperature equations are:

$$C_e(T_e)\frac{\partial T_e}{\partial t} = \nabla\bullet\left(K_e \nabla T_e\right) - G\left(T_e - T_\ell\right) + S\left(\vec{\mathbf{r}},t\right)$$
$$C_\ell(T_\ell)\frac{\partial T_\ell}{\partial t} = \nabla\bullet\left(K_\ell \nabla T_\ell\right) + G\left(T_e - T_\ell\right)$$

The source term $S\left(\vec{\mathbf{r}},t\right)$ is used to describe the local laser energy deposition per unit area and unit time during the laser pulse duration. The two-temperature model can be incorporated into the classical MD technique by adding an additional coupling term into the MD equations of motion […]. In this computational scheme, the diffusion equations are solved simultaneously with MD integration and the electron temperature enters the coupling term that is responsible for the energy exchange between the electrons and the lattice."[9]

Zhigilei and Dongare[9] describe how multiscale modeling of laser ablation can be performed, and how it applies to applications in nanotechnology. This includes three steps, each with its own model; only the first step is relevant to the current work:

1. Irradiation of the target surface by the ultrafast laser pulse is handled by molecular dynamics simulation including the two-temperature model described above; thermal effects are carried into the bulk material by the thermal diffusion equations. Boundary conditions such as traveling pressure waves are computed dynamically in order to suppress unphysical reflections.
2. Ejected (ablated) material forms a plume, which is followed only briefly with the molecular dynamics simulation – within a few nanoseconds it is passed over to a Monte Carlo code for long time scale evolution, measured in microseconds. This calculates velocity, angular distribution, and energy of the various species present in the plume. This differs from the traditional particle-in-cell (PIC) hydrodynamic codes[9] that are often used to follow plasma evolution. One major difference is that the Monte Carlo code handles chemistry, including the formation and destruction of clusters, which are of great interest in some applications.

3. Modeling of film growth occurs when the plume strikes the target. The detailed results of the plume simulation are passed on to a molecular dynamics simulation to handle the clusters as they build the film.

In particular this first step can be adapted to the simulation of the non-ablative laser-matter interactions of the Debye-Waller electron-phonon coupling experiment. The time-resolved diffraction data provides a step-by-step temporal map of the actual lattice temperature during the heating and the cooling stages; the coupled differential equations from the two-temperature model is applied to this lattice temperature data, using the conservation of energy as a constraint to imply the electron temperature. This leaves the electron-phonon coupling constant as the free parameter to be numerically fitted. As the temperatures equilibrate the system settles into the ordinary thermal diffusion equation. Over longer time scales radiative losses would also have to be accounted for, but they hardly contribute during the initial fraction of a nanosecond.

Time Resolved Structural Probes

The first time-domain ultrafast (picoseconds) structural probe experiment was performed in 1982[10] by using electron diffraction to study the physics of melting in the picosecond time scale. This study revealed for the first time a superheated (solid) phase for aluminum with a temperature of 1000 K above melting which lasted ~10 ps. A theory based on nucleation from laser induced dislocations was used to explain the observations.

Diffraction techniques as opposed to optical techniques provide direct information on lattice dynamics as a function of time. Heat transport and mechanical properties are closely associated with the generation and propagation of dislocations. Probing the structural changes on the pico- and sub-picosecond time scale requires x-ray or electron diffraction techniques.

Currently ultrashort time resolution techniques such as laser-based x-ray diffraction often require single crystals for investigation in order to improve the signal-to-noise ratio during the lengthy exposure times. Ultrafast electron diffraction affords the capability to study the case of polycrystalline and amorphous materials.

Probing matter with electrons instead of x-rays offers a number of significant advantages:

- Electron beams with a de Broglie wavelength corresponding to those of hard x-rays (100 keV) are easily obtainable.
- Monochromaticity of the beam is excellent, since $\Delta E/E$ can be as small as 10^{-4} to10^{-5}.
- Scattering cross-sections are extremely large, typically 10^4 to 10^8 times that of x-rays, which makes them ideal for probing the first atomic layers at a crystal surface.
- Use of the photoelectric effect to generate the electron pulses supports very high and adjustable repetition rates from single shot to greater than 100 MHz.
- Temporal resolution of 30 fs or better can be reached when using very high repetition rates.
- Electron diffraction setups (see **Figure 1-1**) are extremely compact and inexpensive as compared to their synchrotron x-ray diffraction counter-parts.

In addition, ultrathin films exhibit properties that differ from thicker films and bulk samples, and are sensitive to the presence of substrates. **Figure 1-2** exhibits a not-fully-dense nanophase which is typical of the films tested.

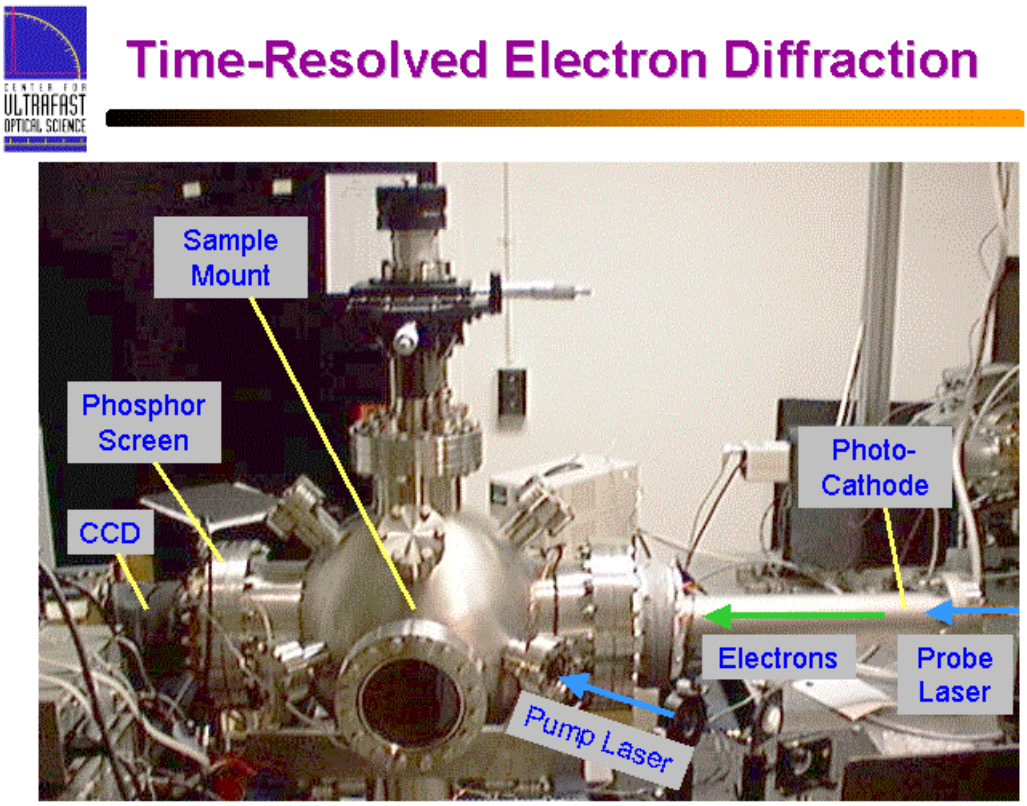

Figure 1-1 Time Resolved Photo-Electron Diffractometer; circa 2002.

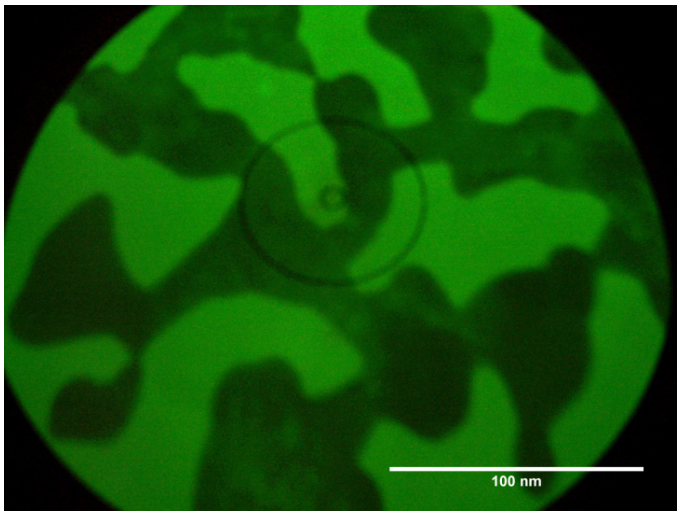

Figure 1-2 Evaporated gold film, 20 nm thick. TEM magnification is 135,000. Note that the "film" is actually a network of nanoparticles. The material constants differ from bulk samples.

Bragg Diffraction and Electron Wavelength

The wavelength of the electrons impinging upon the sample is found from the de Broglie relationship: $\lambda = h/p = h/\gamma m_e \beta c$; for 30 kV the wavelength is 0.0699 Å. Using Bragg's law (see **Figure 1-3**), $m\lambda = 2d_{hkl}\sin(\theta_{hkl})$; with the known value for the interplanar spacing for gold (4.07 Å), the transmission geometry is used to find the magnification of our experimental setup (see **Figure 1-4**), $m\lambda/d_{hkl} \approx R_{hkl}/L$, where R_{hkl} is the measured radius of a diffraction ring or spot pattern, and L is the distance from the sample to the imaging plane for the current setup.

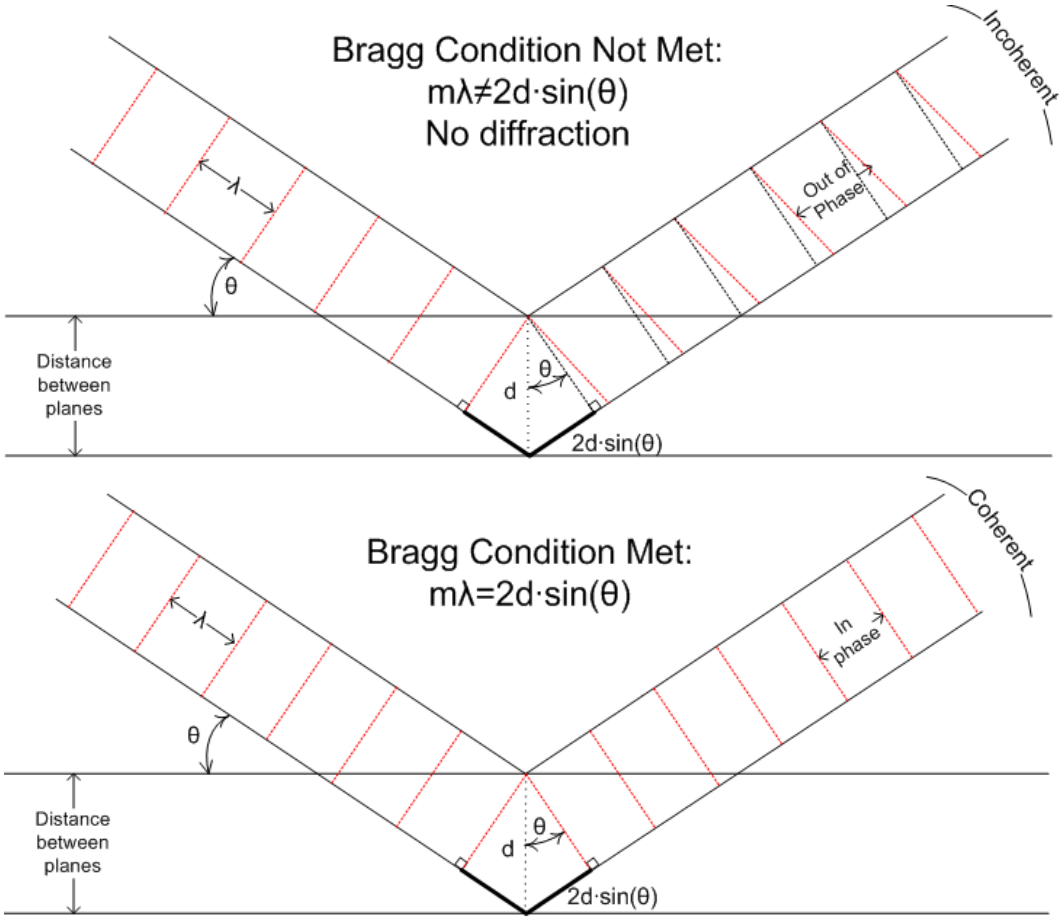

Figure 1-3 Meeting the Bragg condition is required to obtain diffraction patterns.

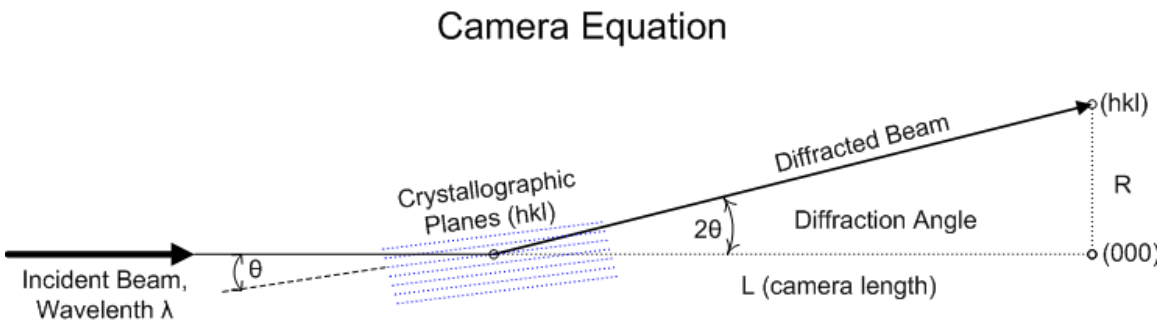

Figure 1-4 Diffraction patterns undergo geometric magnification as they travel to the detector. The magnification is described by the camera equation, and relates the measured ring sizes to the interplanar distances.

Heating and the Debye-Waller Effect

Elementary condensed matter theory leads the theory of diffraction from perfect crystals to the theory of diffraction heated crystals, both perfect and imperfect, which includes the Debye-Waller effect[11]. Though heating short of a phase change does not alter the overall diffraction pattern beyond that due to thermal expansion, the relative intensities of spots from different orders are changed by an exponential factor depending upon the difference in orders, and the difference in temperatures: $I\left(hkl,T\right)=I_0\left(hkl\right)\times\exp\left(-k_BT\mathbf{G}^2/m\omega^2\right)$, where k_BT captures the thermal energy of the average motion, and $\mathbf{G}^2$ holds the (hkl) crystal plane dependence, including the order of diffraction. The other parameters represent the mass and the local restoring force, approximated as harmonic via ω^2, which can be estimated from the experimental values of the Debye temperature: $\hbar\omega_D=k_BT_D$.

UPED produces jitter-free Bragg diffraction patterns, from both single crystal and polycrystalline thin films, which are accumulated by long time exposures of the MCP (microchannel plate) image intensifier with a Peltier-cooled CCD camera. Comparison

of relative intensities of diffraction spots under different laser heating conditions determines the temperature changes via $\log\left(I_1^*/I_2^*\right)/\log\left(I_1/I_2\right) = T^*/T$, where the starred measurements are the heated ones, or $\log\left(I_1^*/I_1\right) \propto -\Delta T\mathbf{G}^2$ which requires a single diffraction order. The availability of multiple orders of diffraction allows for self-consistency checks, as well as providing information about the directionality of the bonding, measures of relative stress, etc.

Advancing the pump pulse in small steps (300 μm for each picosecond) gives a temporal profile of the ion heating induced by the pump pulse. Temporal resolution is limited by the duration of the pump and probe pulses, and any jitter between them. Essentially, we can make an ultrafast movie of structural changes and heat transfer within a material being struck by an ultrafast laser pulse.

An Ultrafast Photo-Electron Diffractometer

Ultrafast photoelectron diffraction (**UPED**) is a temporally short probe/long detector experiment. A short laser pump pulse induces a transformation in the sample, and a short pulse of electrons probes it. For each shot, corresponding to one time delay, a slow detector collects the entire diffraction pattern. When performed at high repetition rates, the detector integrates the results of many shots for each time delay.

Application of a femtosecond laser pulse to matter gives rise to an ultrafast laser-matter interaction involving electrons and ions. This dynamic regime requires temporal measurements on the time scale of femtoseconds and thus is based on correlation phenomena of the femtosecond laser pulse with itself.

Ultrafast Photo-Electron Diffraction has had many successes in this regard [10 12 13]. By harnessing the faster pulses of a relatively stable kilohertz laser and accumulating thousands of shots, we can directly study electron-phonon coupling at the femtosecond

time scale by using the Debye-Waller effect, which relates changes in diffraction intensity to changes in temperature, as well as surface dynamics.

The current approach is illustrated by **Figure 1-5**,which shows the original pulse being split into a pump pulse (and associated delay line), and the probe pulse. Though the probe line process of multiple frequency conversion is quite inefficient with laser power, it is sufficient to drive the photocathode and obtain a pulsed electron beam. The electron pulse is a near replica of the laser pulse, though somewhat temporally broadened[14 15], expanding longitudinally as it propagates.

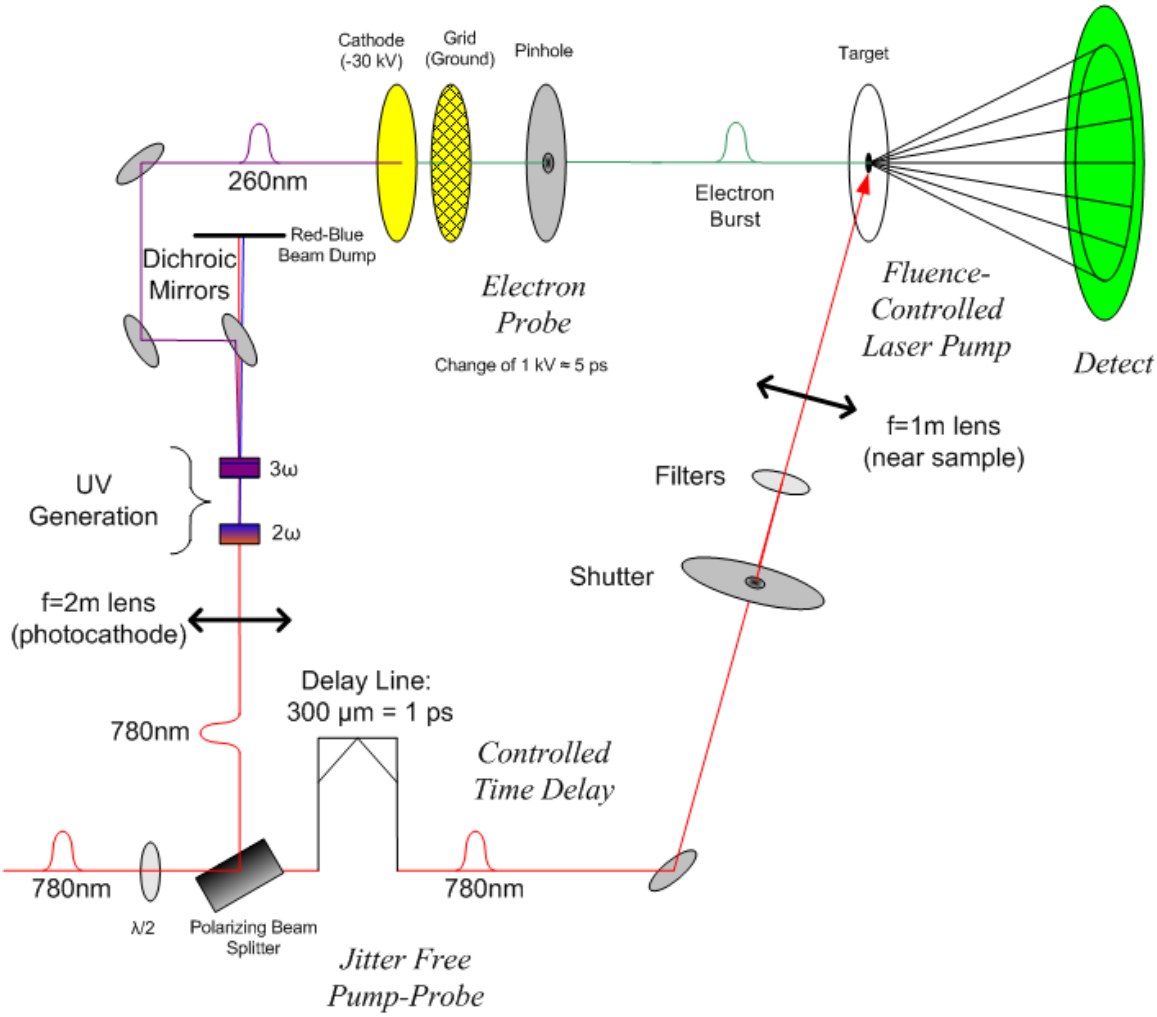

Figure 1-5 Schematic of a sub-picosecond electron diffraction apparatus.

The laser system is an ultrafast Ti:Sapphire, a Clark-MXR Model 2001, generating 150 femtosecond pulses trains in the near infrared, centered at 780 nm, with typical pulse energy of 800 μJ at a repetition rate of 1,000 Hz. The pulse-to-pulse energy stability is within 1% RMS.

Once the laser has delivered a pulse, all of the following optical processes used are jitter-free, so splitting a single ultrafast laser pulse generates jitter-free pump and probe pulses. A half-wave plate followed by a thin-film polarizing beam splitter facilitates setting the relative energy of the two pulses. The probe pulse starts in the near infrared, centered at 780 nm, and is passed through a BBO frequency-doubling crystal to generate 390 nm (blue), and both the blue and the fundamental go through a BBO frequency mixing crystal to generate the third harmonic centered at 260 nm. A series of dichroic mirrors is used to select the UV component and guide it into the vacuum chamber; the other wavelengths pass through the mirrors (95%) and are discarded. When the photocathode is struck by the now-UV pulse it emits a near-replica electron pulse.

The resulting jitter-free Bragg diffraction patterns are accumulated by a long time exposure of the MCP (microchannel plate) image intensifier with of a Peltier-cooled CCD camera. Introduction of any temporal jitter between the pump and the probe reduces the temporal resolution achievable.

The electron gun voltage controls the speed of the electron pulse. The gun is designed for 15 to 30 kV, with the electrons travelling at up to 1/3 the speed of light. The system has an optical delay line for the pump pulse, and an adjustable electron speed for the probe pulse. The pump delay line must make up for the 3-to-1 pump-to-probe speed differential, 300 μm of delay line for each picosecond of temporal delay.

Temporal Resolution

For UPED, the time-resolution is limited essentially by the probe duration. For a photo-electron gun the jitter is due to energy mismatch between the laser pulse and the work-function, and variations due to polycrystalline structure. A high static extraction field, on the order of 5 MV/m as shown in **Figure 1-6**, limits chromatic aberration (a source of jitter) and yields electron bunches of < 200 fs.[16] In general, jitter comes from having trigger events; but simply splitting a laser pulse induces relative delay, not jitter. Since the passive optical elements are all jitter-free, the system as a whole has very low jitter. Temporal resolution is then limited by pulse widths.[17]

UPED has already been performed at 1 ps time-resolution. The probe duration at the sample is mainly due to the photoelectron energy spread ~100 meV, and space charge effects. Other factors include broadening due to the photocathode thickness, the differing path lengths of the electrons, and pump/probe (geometric) mismatch can be kept to less than 10 fs. The energy spread can be very low if the wavelength of the light pulse is matched with the photocathode work function as is done here. A very high extraction field can in addition be applied to the electron gun by pulsing it. The space charge effect occurs mainly in the drift region; and shortening the drift to less than 10 cm can strongly reduce this broadening. Calculations from Qian and El Sayed-Ali[14] show that it is possible to obtain temporal resolution better than 100 fs.

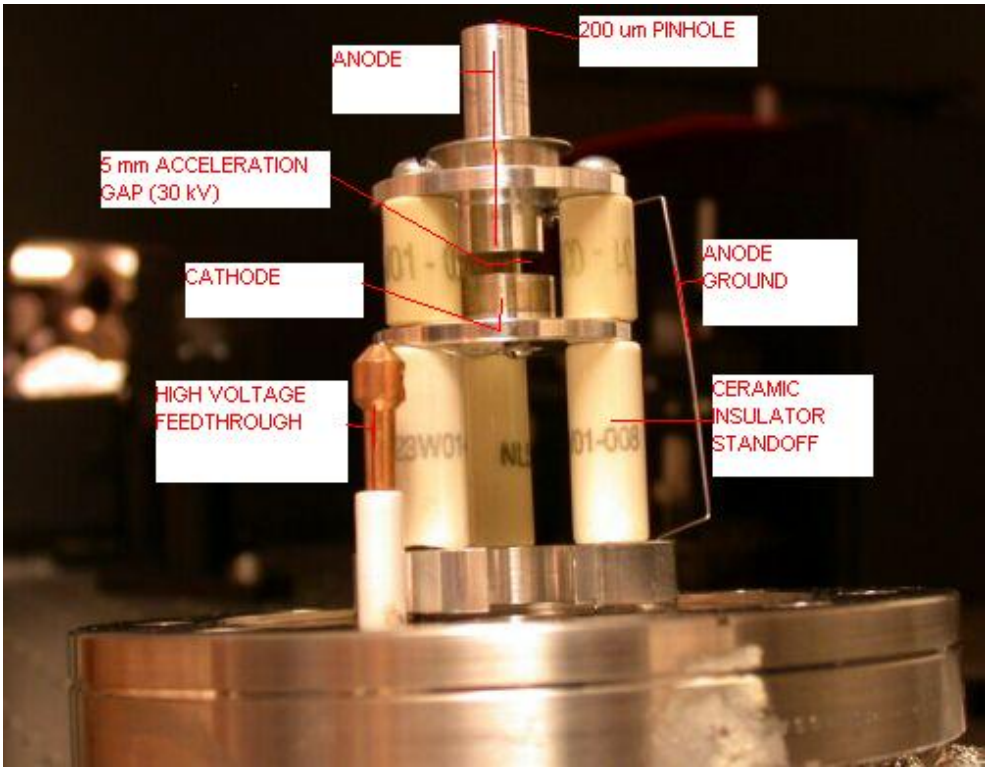

Figure 1-6 Electron Gun designed and built by Ibrahim El Kholy, showing the short gap (5 mm) between photocathode and anode. This design minimizes the space charge effects and hence energy spread.

Chapter 2

Crystal Theory

Crystal Structure

Observation of naturally occurring minerals and cleaving facets of gems showed that crystals have an internal structure that determines their external appearance. ***Steno's Law of constancy of interfacial angles,*** described in 1669[18] by the geologist-physician Nicolaus Steno[19] (1638-1686), expresses this law of external appearance; the angle between corresponding faces of the same mineral is always the same, regardless of the size of the faces. This implies that the mineral is built up from an endless repetition of identical primitive cells. The crystallographer René-Just Haüy[20] (1743-1822) showed how this construction could be carried out, obtaining the required interfacial angles, in 1784. ***Haüy's Law of rational intercepts,*** which states that the faces of a crystal intercept the crystal axes are simple rational fractions, also follows from this construction.

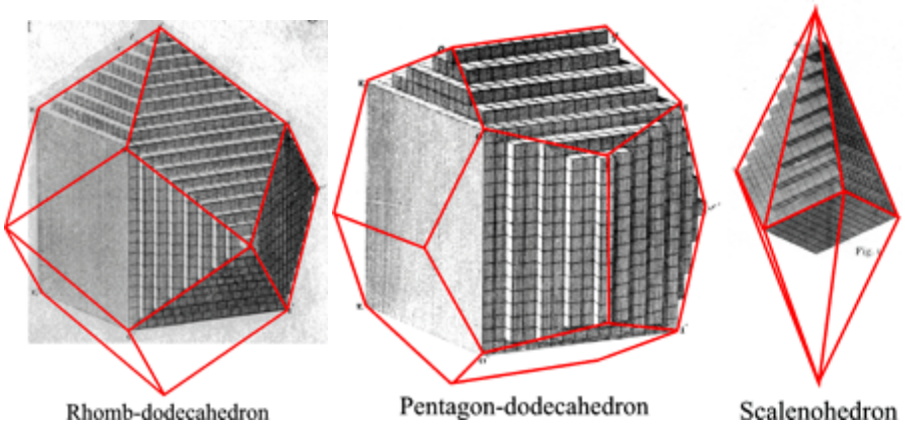

Figure 2-1 Crystal forms for garnet, pyrite, and calcite, built up from uniform primitive cells; (Models from Haüy's *Traité de Minéralogie* (1801) - the crystal forms have been redrawn in red)[21].

There are six crystal systems based upon parallelepipeds, which are prisms with parallelograms as base and sides, and a seventh with a trigonal (rhombohedral) or hexagonal base. These are further elaborated by the interlacing of the crystal systems by centering on their faces (face-centered-cubic, FCC), on their centers (body-centered-cubic, BCC), or on their bases (base-centered-orthorhombic). August Bravais[22] (1811-1863) correctly enumerated the fourteen unique space lattices, which describe the possible translational symmetries of the crystal, in 1845. Point symmetries including rotation, reflection, inversion, and their combinations define 32 crystal classes. When each of the seven crystal systems has its possible point symmetries enumerated, and taking account of the multiple Bravais lattices of that crystal system, there are 230 possible space groups.

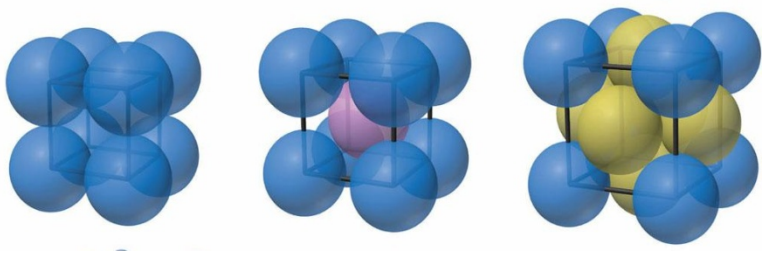

Figure 2-2 Cubic crystals:[23] simple cubic, body centered (BCC), face centered (FCC).

A convenient notation for the identification of crystal faces are the Miller indices[24] published in 1839 by the mineralogist and crystallographer William Hallows Miller[25] (1801-1880). This system takes advantage of Haüy's law of rational intercepts and by using the reciprocals of the intercepts identifies each possible face with a set of three integers. The integers are (almost) always single digit, so the convention is to omit punctuation; if the number is negative, it is so denoted by an over-bar: $(1\,\bar{1}0)$.

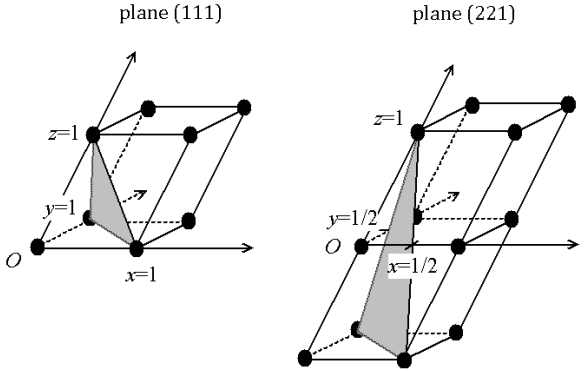

Figure 2-3 Miller indices[26] are determined from reciprocal intercepts with the crystal axes.

Constructing the Unit Cell

The unit cell is endlessly repeated throughout the crystal, and there is always more than one way to construct it. If it is the smallest possible cell by volume it is called a primitive unit cell. Larger cells are often used because they exhibit the point symmetry of the crystal more clearly; their volume will be an integral multiple of the primitive unit cell. For example, the conventional face-centered-cubic cell has four times the volume of its primitive unit cell. A vector representation requires three crystal axes, typically non-orthogonal and of differing lengths, often representing the direction of growth of the crystal. Let the crystal axes $\mathbf{A},\mathbf{B},\mathbf{C}$ define a unit cell; then these form the ***direct lattice basis*** since for any integer u,v,w the vector $\mathbf{R}_{uvw} = u\mathbf{A} + v\mathbf{B} + w\mathbf{C}$ will identify a lattice point. This is abbreviated with the index notation $[uvw]$; removal of common factors

leaves the direction unchanged. Translation along any of the crystal axes puts you in a different cell, but identical in every way to the previous one.

In order to describe the elements of a unit cell the positions of the constituent atoms and molecules must be specified. The notation of Warren[27] conveniently labels the crystal axes numerically: $\mathbf{A_1}, \mathbf{A_2}, \mathbf{A_3}$, and the n elements of the unit cell are described by a set of vectors $\mathbf{R}^n$. Starting from an arbitrary origin within the crystal, each unit cell can be accessed by a triple of integers $m = m_1 m_2 m_3$ by $\mathbf{R}_m = m_1\mathbf{A}_1 + m_2\mathbf{A}_2 + m_3\mathbf{A}_3$. Putting these together gives access to every element of every cell as $\mathbf{R}_m^n = m_1\mathbf{A}_1 + m_2\mathbf{A}_2 + m_3\mathbf{A}_3 + \mathbf{R}^n$.

A Geometric View of Vector Products

Vectors have geometric properties independent of coordinate systems. We will exploit these geometric properties in order to work within the non-orthogonal environment of the crystal lattice. The vector dot product $\mathbf{A}\bullet\mathbf{B} = AB\cos(\theta_{AB})$ projects the length of $\mathbf{A}$ onto the direction of $\mathbf{B}$. This operation is linear over vector addition, and the definition is symmetric, so the dot product is commutative, $\mathbf{A}\bullet\mathbf{B} = \mathbf{B}\bullet\mathbf{A}$. It is used to determine angles between vectors as well as lengths and distances. The condition $\mathbf{A}\bullet\mathbf{B} = 0$ is a test for orthogonality.

The geometrical meaning of the vector cross product $\mathbf{A}\times\mathbf{B} = AB\sin(\theta_{AB})\hat{\mathbf{n}}_{AB}$ is obtained by sliding vector $\mathbf{A}$ along the length of vector $\mathbf{B}$, always remaining in their joint plane, and with $\mathbf{A}$ remaining parallel to itself. This is done by hooking the right hand thumb about vector $\mathbf{B}$ as a guide, and then pushing with that hand to mark out the area of a parallelogram. The "right hand rule" orients $\hat{\mathbf{n}}_{AB}$ with your right thumb, making it normal to the plane of the parallelogram. So in addition to the determination of areas and angles, the creation of the unit vector $\hat{\mathbf{n}}$ determines the orientation of the plane formed by the two

vectors. This operator is linear over vector addition, but note that when the operational order is reversed, your right hand thumb takes the opposite orientation; $\mathbf{B}\times\mathbf{A}=-\mathbf{A}\times\mathbf{B}$. The condition $\mathbf{A}\times\mathbf{B}=0$ is a test for parallelism.

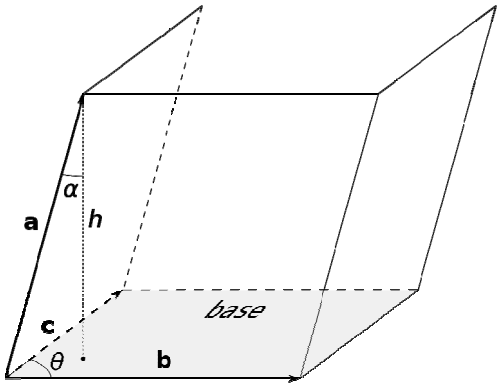

Figure 2-4 Parallelepiped[28] with volume $\mathbf{a}\bullet\mathbf{b}\times\mathbf{c}$

The volume of the parallelepiped defined by the three vectors $\mathbf{A},\mathbf{B},\mathbf{C}$ is found by $V=\mathbf{A}\bullet\mathbf{B}\times\mathbf{C}=\mathbf{A}\bullet\left(\mathbf{B}\times\mathbf{C}\right)=\mathbf{A}\bullet\left(BC\sin\left(\theta_{BC}\right)\hat{\mathbf{n}}_{BC}\right)=ABC\sin\left(\theta_{BC}\right)\cos\left(\theta_{A,B\times C}\right)$.where the height is encoded by the dot product $\mathbf{A}\bullet\hat{\mathbf{n}}_{BC}=A\cos\left(\theta_{A,B\times C}\right)$. The volume will be negative if the ordering is not right handed; this means that $\hat{\mathbf{n}}_{BC}$ was pointing the wrong way. Since the volume is the same regardless of the ordering of the edges, cyclic permutations are equivalent: $\mathbf{A}\bullet\mathbf{B}\times\mathbf{C}=\mathbf{C}\bullet\mathbf{A}\times\mathbf{B}=\mathbf{B}\bullet\mathbf{C}\times\mathbf{A}$, as are interchanges of the operations: $\mathbf{A}\times\mathbf{B}\bullet\mathbf{C}=\mathbf{C}\times\mathbf{A}\bullet\mathbf{B}=\mathbf{B}\times\mathbf{C}\bullet\mathbf{A}$. Non-cyclic permutations change the implied order of the vector cross product, and hence change the sign. Repetition of a vector within the triple product is a case of parallelism, and the result is zero.

Reciprocal Space

The distance between parallel faces of a parallelepiped is $\mathbf{A}\bullet\hat{\mathbf{n}}_{BC} = A\cos\left(\theta_{A,B\times C}\right)$ for the $\mathbf{B}\times\mathbf{C}$ face. $\mathbf{C}^* = \dfrac{\mathbf{A}\times\mathbf{B}}{\mathbf{C}\bullet\mathbf{A}\times\mathbf{B}} = \dfrac{AB\sin\left(\theta_{AB}\right)\hat{\mathbf{n}}_{AB}}{AB\sin\left(\theta_{AB}\right)\mathbf{C}\bullet\hat{\mathbf{n}}_{AB}} = \dfrac{\hat{\mathbf{n}}_{AB}}{C\cos\left(\theta_{C,A\times B}\right)}$ and its cyclic permutations defines an alternative set of vectors $\mathbf{A}^*,\mathbf{B}^*,\mathbf{C}^*$ with magnitude which is the reciprocal of this distance between faces. These vectors are normal to the planes of the unit cell, and form the ***reciprocal lattice basis***. Reciprocal lattice elements can be denoted $\mathbf{H}_{hkl} = h\mathbf{A}^* + k\mathbf{B}^* + l\mathbf{C}^*$, with common integral factors removed, and is abbreviated $\left(hkl\right)$. As is shown later, this similarity to the Miller index notation is intentional. An important property which follows directly from this definition is that the direct and reciprocal basis vectors are orthonormal: $\mathbf{C}\bullet\mathbf{C}^* = 1$ and $\mathbf{C}^*\bullet\mathbf{A} = \mathbf{C}^*\bullet\mathbf{B} = 0$ for each pair. Furthermore, the direct lattice can be recovered from the reciprocal lattice with $\mathbf{C} = \dfrac{\mathbf{A}^*\times\mathbf{B}^*}{\mathbf{C}^*\bullet\mathbf{A}^*\times\mathbf{B}^*}$ by direct substitution and application of the vector identity $\left(\mathbf{A}\times\mathbf{B}\right)\times\left(\mathbf{C}\times\mathbf{D}\right) = \left(\mathbf{A}\bullet\mathbf{B}\times\mathbf{D}\right)\mathbf{C} - \left(\mathbf{A}\bullet\mathbf{B}\times\mathbf{C}\right)\mathbf{D}$ [29]; they are mathematically dual spaces. The volume of the reciprocal space unit cell $V^* = \mathbf{A}^*\bullet\mathbf{B}^*\times\mathbf{C}^* = \dfrac{1}{\mathbf{A}\bullet\mathbf{B}\times\mathbf{C}} = \dfrac{1}{V}$ is the reciprocal of the corresponding direct lattice cell volume. Forming matrices column-wise from the basis vectors, the orthonormal condition means that $\left[\mathbf{ABC}\right]^{-1} = \left[\mathbf{A}^*\mathbf{B}^*\mathbf{C}^*\right]^T$, and as their determinants are the volumes, it follows that the volumes are reciprocals.

Distance Between Planes

By construction $\mathbf{H}_{hkl} = h\mathbf{A}^* + k\mathbf{B}^* + l\mathbf{C}^*$ is normal to the plane (hkl) with magnitude equal to the reciprocal of the distance from the origin: $|\mathbf{H}_{hkl}| = \frac{1}{d_{hkl}}$. Evaluating the left hand side, $|\mathbf{H}_{hkl}|^2 = \left(h\mathbf{A}^* + k\mathbf{B}^* + l\mathbf{C}^*\right)^2 = \frac{h^2}{A^2} + \frac{k^2}{B^2} + \frac{l^2}{C^2} + 2hk\mathbf{A}^*\bullet\mathbf{B}^* + 2hl\mathbf{A}^*\bullet\mathbf{C}^* + 2kl\mathbf{B}^*\bullet\mathbf{C}^*$; this can be evaluated directly if the dihedral angles are known; otherwise use the vector identity $(\mathbf{A}_1\times\mathbf{A}_2)\bullet(\mathbf{A}_3\times\mathbf{A}_4) = (\mathbf{A}_1\bullet\mathbf{A}_3)(\mathbf{A}_2\bullet\mathbf{A}_4) - (\mathbf{A}_1\bullet\mathbf{A}_4)(\mathbf{A}_2\bullet\mathbf{A}_3)$ after transforming back to the direct lattice. For cubic systems the reciprocal lattice basis vectors are orthogonal and of equal length, and so the expression reduces directly to $|\mathbf{H}_{hkl}|^2 = \frac{1}{A^2}\left(h^2 + k^2 + l^2\right)$ and so $d_{hkl} = \frac{A}{\sqrt{h^2 + k^2 + l^2}}$ for cubic crystals such as for gold, platinum, aluminum, and silicon.

Direct Lattice Planes to Reciprocal Lattice Points

Every plane of the direct lattice can be represented by an element of the reciprocal lattice. Starting with crystal axes $\mathbf{A},\mathbf{B},\mathbf{C}$ representing a unit cell of volume $V = \mathbf{A}\bullet\mathbf{B}\times\mathbf{C}$, and the direct lattice direction $[uvw]$, define a vector $\mathbf{n}$ which is normal to the plane which connects their tips, and divide by the unit cell volume. The normal direction is given by the vector cross product of the vectors the tips of $u\mathbf{A}$ *to* $v\mathbf{B}$ and $u\mathbf{A}$ *to* $w\mathbf{C}$:

$\mathbf{n} = \frac{(v\mathbf{B} - u\mathbf{A})\times(w\mathbf{C} - u\mathbf{A})}{V} = uv\frac{\mathbf{A}\times\mathbf{B}}{\mathbf{C}\bullet\mathbf{A}\times\mathbf{B}} + vw\frac{\mathbf{B}\times\mathbf{C}}{\mathbf{A}\bullet\mathbf{B}\times\mathbf{C}} + uw\frac{\mathbf{C}\times\mathbf{A}}{\mathbf{B}\bullet\mathbf{C}\times\mathbf{A}}$, where the volume has been replaced by different cyclic permutations of the triple vector product on the right hand side. The three terms remaining on the right hand side represent important physical vectors: by construction their sum is normal to the plane of the axial intercepts, while each one is perpendicular to the face defined by that pair of axes, with magnitude equal to

the reciprocal of the distances between faces. These terms are members of the reciprocal lattice: $\mathbf{n} = uv\mathbf{C}^* + vw\mathbf{A}^* + uw\mathbf{B}^*$.

Reciprocal Lattice Points to Direct Lattice Planes

The points of the reciprocal lattice represent families of planes in the direct lattice. By removal of common factors this expression for the normal of the direct lattice plane is reduced to lowest integer form, and the reciprocal lattice element $\mathbf{H}_{hkl} = h\mathbf{A}^* + k\mathbf{B}^* + l\mathbf{C}^*$ denoted (hkl), is shown to be equivalent to the Miller index by transforming each term from the reciprocal space to the direct lattice space: $l\mathbf{C}^* \Rightarrow \dfrac{h\mathbf{A}^* \times j\mathbf{B}^*}{l\mathbf{C}^* \bullet h\mathbf{A}^* \times j\mathbf{B}^*} = \dfrac{\mathbf{C}}{l}$, and similarly $h\mathbf{A}^* \Rightarrow \dfrac{\mathbf{A}}{h}, k\mathbf{B}^* \Rightarrow \dfrac{\mathbf{B}}{k}$. From analytic geometry we know these to be the intercepts of the plane $\dfrac{x}{\left(A/h\right)} + \dfrac{y}{\left(B/k\right)} + \dfrac{z}{\left(C/l\right)} = \dfrac{hx}{A} + \dfrac{ky}{B} + \dfrac{lz}{C} = 1$ when the directions are measured in the same units; when these are scaled by the three axial vectors the Miller indices for the plane (hkl) are obtained, and the equation of this plane in the direct lattice space becomes $hx + ky + lz = \text{constant}$; the constant is no longer unity due to the rationalization and the scaling. The left hand expression also appears in the dot product $\mathbf{H}_{hkl} \bullet \mathbf{R}_{uvw} = \left(h\mathbf{A}^* + k\mathbf{B}^* + l\mathbf{C}^*\right) \bullet \left(u\mathbf{A} + v\mathbf{B} + w\mathbf{C}\right) = hu + kv + lw$, so $(hkl) \bullet [uvw] = \text{constant}$ is the condition that direction $[uvw]$ is parallel to plane (hkl). If the constant is zero, then $[uvw]$ is a zone axis, and lies in the plane (hkl).

Crystal Planes and Diffraction

Real crystals are made up of atoms or molecules within the unit cells, and can be probed by means of coherent radiation, though the coherence requirement (temporal and spatial) is limited to a very small interaction volume. The Bragg hypothesis[30] is that the crystal planes act as partially reflecting mirrors, and when the angle of the beam with a stack of parallel planes supports constructive interference of that beam, that stack of planes will produce a diffracted beam. The diffraction condition is well known to require path lengths that differ only by integer multiples of the wavelength. The specifications available are the beam wavelength λ, the direction $[uvw]$ from which it approaches the crystal, and the orientation of the crystal which provides the (hkl) family of planes with spacing $d_{hkl} = \frac{1}{|\mathbf{H}_{hkl}|}$. The density of atoms on the planes becomes sparser as the distance becomes closer; thus the principal (low index) planes will diffract more than the high index planes.

In reciprocal space it is convenient to take the beam directions as unit vectors, then scale them to reciprocal length: $\frac{\mathbf{S}_0}{\lambda}$ is the incoming beam, defining the origin as the first plane it strikes, and $\frac{\mathbf{S}}{\lambda}$ is the specularly reflected beam with unchanged wavelength; thus both vectors make the same glancing angle θ with the plane (hkl), so that $\mathbf{S}_0 \bullet \mathbf{S} = \cos(2\theta)$.

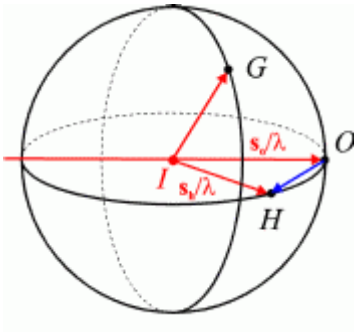

Figure 2-5 Ewald sphere[31], from the IUCr Online Dictionary of Crystallography; S_h (our S) is the reflected beam; H and G are nodes of the reciprocal space on the surface of the sphere, and will diffract.

It is convenient to construct the Ewald sphere of radius $\frac{1}{\lambda}$ with the incident and the reflected beams originating its center, and with the wave vector $\frac{\mathbf{S}_0}{\lambda}$ striking the origin of the reciprocal lattice. The appearance of a reflected beam is determined by the (hkl) family of planes which is struck; only those reciprocal lattice points on (or very near) the surface of the sphere are candidates, and the reflected wave vector $\frac{\mathbf{S}}{\lambda}$ must land on one of the $\mathbf{H}_{hkl}$ for diffraction to occur. Thus the diffraction condition on the Ewald sphere is $\frac{\mathbf{S}_0 - \mathbf{S}}{\lambda} = \mathbf{H}_{hkl}$, which is the Laue diffraction equation. As the wavelength is made much smaller than the interplanar distances the surface of the Ewald sphere grows larger, and the surface curvature flattens so that it appears to be a plane projection with many diffraction spots. This is especially apparent as the energy of an electron beam is increased.

An alternative notation for wave vectors is to include a factor of 2π. Then $\mathbf{K} = 2\pi\frac{\mathbf{S}}{\lambda}$ and $\mathbf{K}_0 = 2\pi\frac{\mathbf{S}_0}{\lambda}$ so that the Laue equation becomes $\mathbf{K} - \mathbf{K}_0 = \mathbf{G}$ where $\mathbf{G} = 2\pi\mathbf{H}_{hkl}$ is any reciprocal lattice node on the surface of this rescaled Ewald sphere which is often called k-space. This relates directly to the physics convention for the wave vector $|\mathbf{k}| = 2\pi/\lambda$, such as the wave vector expression of the de Broglie relation $\mathbf{k} = \hbar\mathbf{p}$.

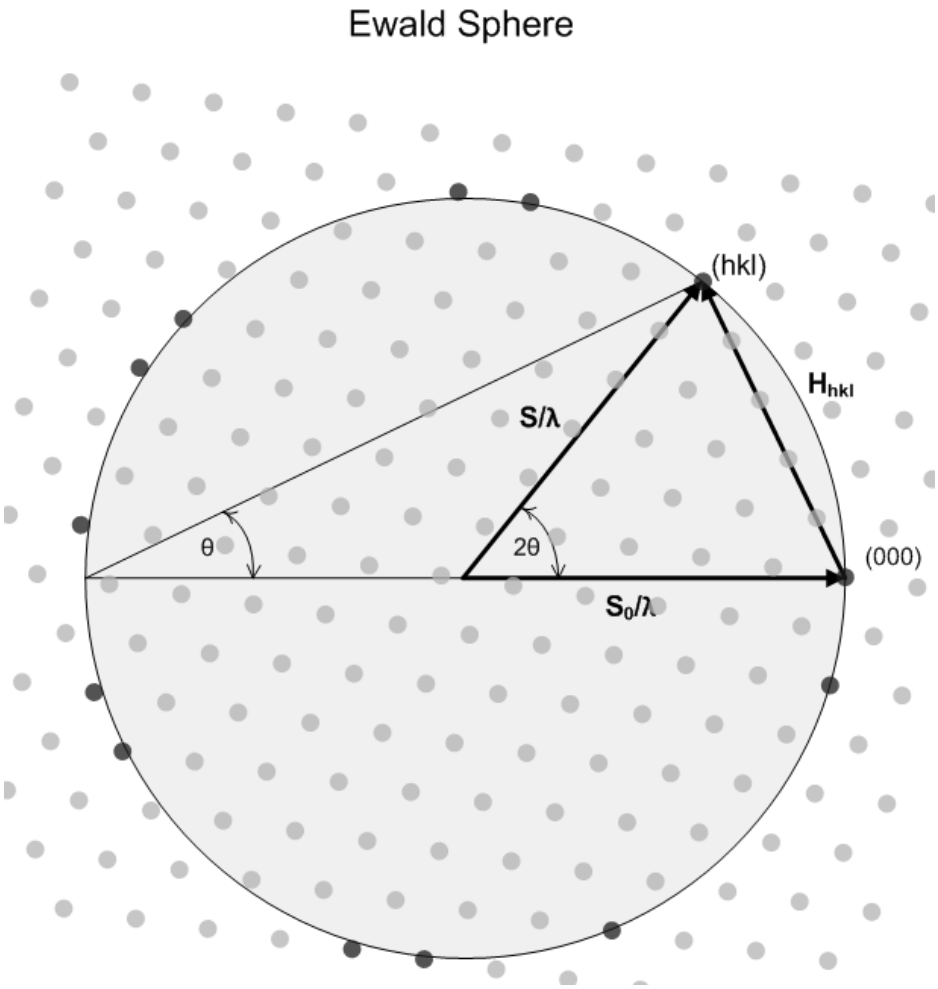

Figure 2-6 Ewald sphere depicted in two dimensions, with multiple reciprocal lattice nodes on or near the circumference. Each of these could appear in the diffraction pattern.

Bragg's law can be derived from the Laue equation, as it is implicit in the magnitudes:

$\left|\frac{\mathbf{S}_0-\mathbf{S}}{\lambda}\right| = \left|\mathbf{H}_{hkl}\right| = \frac{1}{d_{hkl}}$ and rearranging and evaluating the expressions gives

$\lambda = d_{hkl}\sqrt{\left(\mathbf{S}_0-\mathbf{S}\right)^2} = d_{hkl}\sqrt{2-2\mathbf{S}_0\bullet\mathbf{S}} = d_{hkl}\sqrt{2-2\cos\left(2\theta\right)} = d_{hkl}\sqrt{4\sin^2\left(\theta\right)}$, the familiar form $m\lambda = 2d_{hkl}\sin\left(\theta\right)$, with the integer m included for the higher order spots.

Atomic Scattering Mechanisms

The Bragg and Laue equations are kinematical; they conserve momentum, explicitly in the case of Laue, but do not trace the flow of energy, or consider any secondary (multiple) diffraction. It is the general weakness of the scattering that makes it particularly useful and easy to analyze. Diffraction studies generally use beams or pulses of electromagnetic radiation in the form of x-rays, or particles, particularly neutrons and electrons, though we do not consider neutrons here.

Elastic scattering of electrons differs from that of x-rays. Electron-electron scattering is inelastic, but scattering from the net potential well of the atomic core is elastic due to the large mass difference, and so contributes to the diffraction image. Elastically scattered x-rays are mostly from the electron cloud. For light atoms, such as hydrogen, where the electrons can be much delocalized, x-rays cannot be used to monitor the nuclear position; however, for heavy atoms with many core electrons x-rays are an efficient tool for locating the nucleus. Thus, in general, electrons are best for monitoring the position of the nucleus, while x-rays are better suited for monitoring the density of electron states.

The atomic cross-section radius seen by electrons[32] is roughly equal to:

$$\sigma_e = \pi b^2 = \pi \left(\frac{Ze^2}{E} \right)^2 ,$$

with Z the atomic number, E the kinetic energy of the electron, e the electron charge. Ignoring polarization, the atomic cross section seen by an x-ray is roughly equal to:

$$\sigma_X = Z \pi r_e^{\,2} ,$$

where $r_e = \frac{e^2}{m_e c^2}$ is the electron classical radius, depending upon the electron mass and the speed of light in the form of its rest energy, E_0. The ratio of cross sections, electron to x-rays is thus given by:

$$R_{e/X} = \frac{\sigma_e}{\sigma_X} = Z\left(\frac{E_0}{E}\right)^2 .$$

For the system being described, the electron energy is provided by the electric potential of a photo-electron gun designed to work from 15 to 30 kV. A simple relativistic calculation[33] gives the electron velocity: the total energy is just the rest mass energy plus the work done on the electron, $\gamma E_0 = E_0 + E$, and is equal to the rest mass energy times the relativistic Lorentz factor, $\gamma = \left(1-\beta^2\right)^{-1/2}$; isolating and inverting this gives the electron speed as $\beta = \frac{v}{c} = \left(1-\gamma^{-2}\right)^{1/2}$. It also follows that $\frac{E_0}{E} = \left(\gamma - 1\right)^{-1}$, so the ratio of cross sections is simplified to:

$$R_{e/X} = \frac{\sigma_e}{\sigma_X} = Z\left(\gamma - 1\right)^{-2} .$$

For an electron accelerated through 30 kV the Lorentz factor $\gamma = 1.0587$, and the speed is $\beta = 0.328 = \frac{v}{c}$, or 1/3 the speed of light. For a heavy element such as gold, Z=79 we have $R_{e/X} = \frac{79}{0.0587^2} = 2.2\times10^4$. As the relativistic factor increases $R_{e/X}$ decreases; clearly this model favors low speed electrons, which are in fact used for detailed surface studies; as the electron energy increases the electrons gain penetration power, interacting less and less with the material. For this reason most transmission electron microscopes operate in the range 100 to 400 kV; at 512 kV the relativistic factor is $\gamma = 2$, and $R_{e/X} = Z$.

The ratio of intensities is $I_{e/X} = R_{e/X}^2$, so for 30 kV acceleration typically is 10^8. This large ratio has two consequences: (1) x-rays are excellent for thick samples or bulk studies and electrons are excellent for surface, gas, and thin sample studies, and (2) there is a consequence specific to time-resolved diffraction: the electron penetration depth is shorter than the pump light so they can probe a sample excitation uniformly, which is not

generally the case for x-rays; the exception is for x-rays at glancing angles. This latter effect will make a significant contribution towards improvement of the signal-to-noise ratio of the diffracted signal for electrons.

Elastic Scattering from a Crystal

Elastic scattering of electrons or x-rays from the periodic array of a crystal can be analyzed in terms of the scattering amplitude function for each type of atom, $F(\mathbf{K}_0, \mathbf{K})$, in terms incoming and outgoing wave vectors. In this study only elastic scattering conforming to the Laue equation is considered; the illuminating beam is the incoming wave vector $\mathbf{K}_0 = 2\pi \frac{\mathbf{S}_0}{\lambda}$, while the diffracted beam is the outgoing wave vector $\mathbf{K} = 2\pi \frac{\mathbf{S}}{\lambda}$.

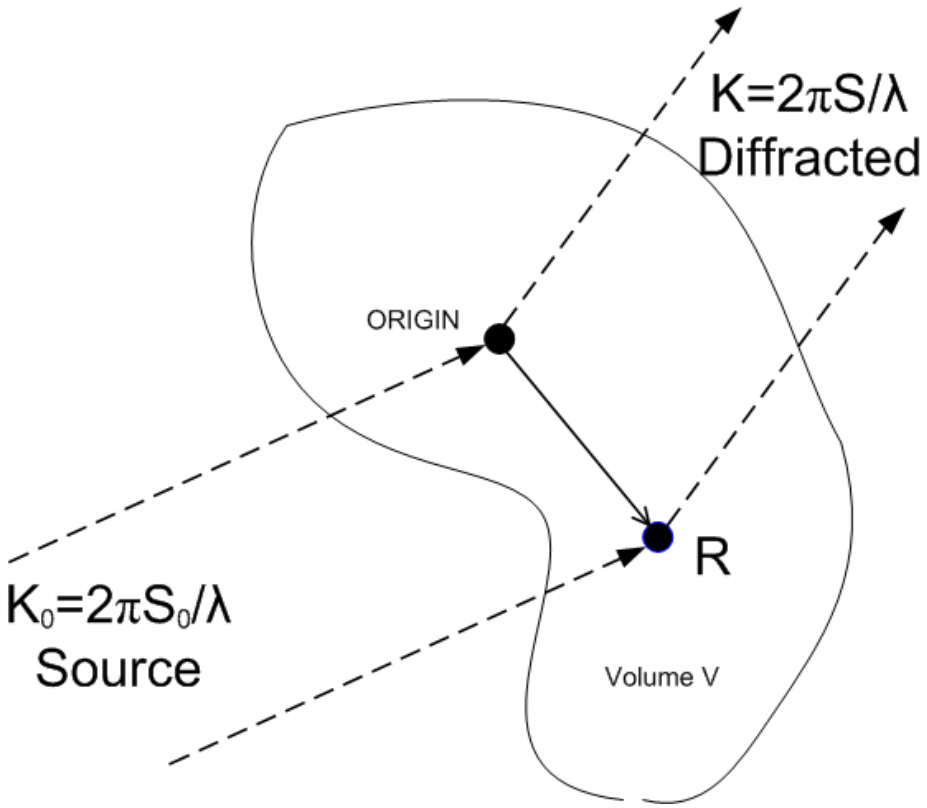

Figure 2-7 Illustration of elastic scattering from multiple sites within a crystal.

This simplified model uses plane waves, with is reasonable because the source and the detector are very distant from the sample in terms of the wavelengths used. Consider Figure 2-7, where the source beam, going in direction $\mathbf{S}_0$, strikes at the origin and an arbitrary cell on the lattice labeled $\mathbf{R}$; a portion of the beam is elastically scattered from each of these cells into the detector, direction $\mathbf{S}$. The diffraction conditions are essentially the same everywhere in the crystal, so the difference in path lengths is the controlling factor: $\mathbf{R}\bullet 2\pi\left(\mathbf{S}-\mathbf{S}_0\right)=\lambda\mathbf{R}\bullet\left(\mathbf{K}-\mathbf{K}_0\right)=\lambda\mathbf{R}\bullet\mathbf{G}$, where $\mathbf{G}=\mathbf{K}-\mathbf{K}_0$ is the alternative notation (Figure 2-6) for the Laue equation in terms of the wave vectors of the Ewald sphere. Multiplying by $\left(i/\lambda\right)$ to convert distance to complex phase gives $\exp\left(i\mathbf{R}\bullet\mathbf{G}\right)$ which along with the amplitude of the atomic scattering factor for each lattice point yields an integral over the crystal volume $F\left(\mathbf{G}\right)=\int_V f\left(\mathbf{R}\right)\exp\left(i\mathbf{R}\bullet\mathbf{G}\right)d\mathbf{R}$.

This is the scattering amplitude in terms of the reciprocal lattice nodes, which are the Bragg planes.

There are several items of note about this integral, beginning with the phase expression $\exp(i\mathbf{R}\bullet\mathbf{G})$ for which we have previously noted that $\mathbf{G} = 2\pi\mathbf{H}_{hkl}$, and thus is 2π times a reciprocal space point; therefore the inner product $\mathbf{R}\bullet\mathbf{G}$ is an integer multiple of 2π so the $\exp(i\mathbf{R}\bullet\mathbf{G}) = 1$ at every crystal lattice point when the Laue condition is satisfied. The integral is also clearly recognized as a Fourier transform of the atomic scattering amplitude; the structure of the integral makes it clear that the crystal lattice is the spatial Fourier transform of the reciprocal lattice, and vice versa. The use of wave vectors $\mathbf{k} = \hbar\mathbf{p}$ to navigate reciprocal space shows that the Laue condition is also a condition on momentum. The volume of integration simply increases the contribution in proportion to the number of cells in the crystal; it is apparent that the fundamental information all lies within the unit cell of the crystal.

Structure Factors

However, we have only taken into account the lattice positions; many crystal structures, including FCC and BCC, include an additional "basis" to describe the off-lattice atoms. These can result in additional constructive and destructive interference. For example, the primitive cell of the FCC structure has an additional basis which can be described by an additional three vectors $\mathbf{R}^1 = \frac{1}{2}(\mathbf{A}+\mathbf{B}), \mathbf{R}^2 = \frac{1}{2}(\mathbf{B}+\mathbf{C}), \mathbf{R}^3 = \frac{1}{2}(\mathbf{C}+\mathbf{A})$ which connect the lattice points to the face centers. This allows the calculation of the *structure factor* for this crystal: $F_{hkl} = \sum_m f_m \exp\left(i\mathbf{G}\bullet\mathbf{R}^m\right)$, where f_m is the atomic form factor for the type of atom at position m. For crystals made up of a single element, such as gold or platinum, the f_m are all the same, though in the rock salt FCC structure they alternate. Expanding the structure factor expression for gold yields four terms, one for the lattice point serving as the origin of the cell, and the three additional basis vectors products : $F_{hkl} = f\left[\exp(0)+\exp\left(i\pi\{h+k\}\right)+\exp\left(i\pi\{k+l\}\right)+\exp\left(i\pi\{l+h\}\right)\right]$. The first term is unity ; the other arguments involve integer expressions which may be positive or negative, depending upon the Miller indices. These exponentials will become +1 if the index sum is even, or -1 if the index sum is odd. Since each index is paired once with each of the others, they will all be even sums if all of the indexes are even, or if all of the indexes are odd; all cases with mixed indices result in two sums being odd, and one even. This produces the index rule for FCC structure factors with a single atomic type such as copper, gold, and platinum: $F_{hkl} = 0$ for mixed index reflections, and these Bragg reflections vanish.

Imperfect Crystals

Imperfect crystals result in deviations from the expressions derived previously; B.E. Warren[27] devotes an entire chapter to the subject, and its sensitivity to imperfections is one of the advantages of electron diffraction[34]. In general, the defect information appears between the Bragg reflections, though some effects, such as beam broadening due to small crystal size (Scherrer formula[35]), or amplitude reduction due to temperature (Debye-Waller effect) impact the Bragg reflections directly. Multiple elastic scattering inside a sample also leads to departures from Bragg's law, though this is not seen with very thin samples.

Temperature and the Debye-Waller Effect

Consider the effects of temperature upon a perfect crystal as discussed by Kittel[22]: the lattice positions $\mathbf{R}^m$ are now averages over time due to the thermal vibrations. Let $\boldsymbol{\delta}^m$ be the instantaneous deviation from the average position. The simplest model is the thermal average energy of an isotropic harmonic oscillator: $\langle U \rangle = \frac{3}{2} k_B T = \frac{1}{2} m\omega^2 \left\langle \left(\delta^m\right)^2 \right\rangle$. Thus the thermal average displacement can be expressed as $\left\langle \left(\delta^m\right)^2 \right\rangle = 3k_B T / m\omega^2$. This depends upon the temperature, the atomic mass, and the restoring forces which in turn determine the oscillation frequency. An estimation of this frequency can be obtained from experimental values of the Debye temperature relationship: $\hbar\omega_D = k_B T_D$.

The structure factor of the heated crystal becomes $F_{hkl} = \sum_m f_m \exp\left(i\mathbf{G}\bullet\left\{\mathbf{R}^m + \boldsymbol{\delta}^m\right\}\right)$ with each term expanding as $\exp\left(i\mathbf{G}\bullet\mathbf{R}^m\right)\exp\left(i\mathbf{G}\bullet\boldsymbol{\delta}^m\right)$. The second factor contains the vibrational effects of the temperature, which are presumed to be random and incoherent

with other atoms of the structure whenever an equilibrium temperature has been reached. The structure factor is not directly observed; most detectors respond to time averaged intensity, so the contribution is a thermal average, with series expansion

$$\left\langle \exp\left(i\mathbf{G}\bullet\boldsymbol{\delta}^m\right)\right\rangle = 1+\frac{i}{1!}\left\langle \mathbf{G}\bullet\boldsymbol{\delta}^m\right\rangle + \frac{i^2}{2!}\left\langle \left(\mathbf{G}\bullet\boldsymbol{\delta}^m\right)^2\right\rangle + \cdots$$

The first order term vanishes due to the randomness of $\boldsymbol{\delta}^m$, and the second order term is $\frac{i^2}{2!}\left\langle \left(\mathbf{G}\bullet\boldsymbol{\delta}^m\right)^2\right\rangle = -\frac{1}{2}G^2\left\langle \boldsymbol{\delta}^m\bullet\boldsymbol{\delta}^m\right\rangle\left\langle \cos\left(\theta\right)^2\right\rangle = -\frac{1}{6}G^2\left\langle \left(\delta^m\right)^2\right\rangle$. Ignoring higher order terms, this sum can be expressed as a new exponential function:

$\exp\left(-\frac{1}{6}G^2\left\langle \left(\delta^m\right)^2\right\rangle\right) = 1-\frac{1}{6}G^2\left\langle \left(\delta^m\right)^2\right\rangle + \cdots$, with the higher order terms matching exactly to our ignored terms if they are harmonic oscillators. Expressed as an experimentally detectable intensity we have $I_{hkl} = I_0\exp\left(-\frac{1}{3}G^2\left\langle \left(\delta^m\right)^2\right\rangle\right)$, where the exponential is the *Debye-Waller factor*. Note that as $\left|\mathbf{G}\right| = 2\pi\left|\mathbf{H}_{hkl}\right| = \frac{2\pi}{d_{hkl}}$ we can make use of Bragg's law to write $\left|\mathbf{G}\right| = \frac{4\pi\sin\left(\theta_{hkl}\right)}{\lambda}$, and this form is often used. Substituting the previously derived thermal expression for $\left\langle \left(\delta^m\right)^2\right\rangle$ gives a useful form for the Debye-Waller factor of $I_{hkl} = I_0\exp\left(-k_B T G^2/m\omega^2\right)$.

The Debye-Waller factor reduces the amplitude of the Bragg peaks; more rapidly as the temperature increases, and more so for the higher-index Bragg planes. This loss of amplitude is due to inelastic scattering, and will appear between the Bragg peaks as increased diffuse reflections.

Temperature information can be retrieved by comparison of the same reflection heated and unheated, or by analysis of a set of Bragg reflections with different Miller indices. This is in addition to changes in peak position due to thermal expansion of the crystal,

which is a bulk property. This also provides a measure of strain as relative change of peak position $\Delta R/R$.

For an FCC crystal with Bragg plane (hkl) we have $G^2 = (2\pi)^2 \frac{h^2+k^2+l^2}{a^2}$, and making use of the Debye temperature formula $\omega_D = \frac{k_B T_D}{\hbar}$ a form is obtained which depends upon the equilibrium temperature, the Bragg plane (hkl) and properties of the crystal: the cell size a, its Debye temperature T_D, and the mass of the atom:

$I_{hkl} = I_0 \exp\left(-\left(\frac{2\pi\hbar}{aT_D} \right)^2 \frac{\left(h^2+k^2+l^2\right)T}{mk_B} \right)$. This FCC approximation provides a tool for analyzing heating effects on diffraction data, and was used to generate **Table 2-1** and **Table 2-2**.

Table 2-1 Reduction of Intensity of Platinum Diffraction, Debye-Waller Effect.

Element	Structure	T_D	Mass	a	$\omega=kT_D/\hbar$
Pt	FCC	240	3.239448E-25	3.9242E-10	3.1421E+13
	(111)	(200)	(220)	(311)	(331)
T (in K)	3	4	8	11	19
200	0.9934	0.9912	0.9824	0.9759	0.9588
225	0.9926	0.9901	0.9803	0.9730	0.9538
250	0.9917	0.9890	0.9781	0.9700	0.9488
275	0.9909	0.9879	0.9759	0.9671	0.9438
300	0.9901	0.9868	0.9738	0.9641	0.9389
325	0.9893	0.9857	0.9716	0.9612	0.9339
350	0.9884	0.9846	0.9695	0.9583	0.9290
375	0.9876	0.9835	0.9673	0.9554	0.9242
400	0.9868	0.9824	0.9652	0.9525	0.9193

Table 2-2 Percentage Change in Intensity from 300 K for Platinum Diffraction.

T (in K)	(111)	(200)	(220)	(311)	(331)
300	0.00%	0.00%	0.00%	0.00%	0.00%
325	-0.08%	-0.11%	-0.22%	-0.30%	-0.52%
350	-0.17%	-0.22%	-0.44%	-0.61%	-1.05%
375	-0.25%	-0.33%	-0.66%	-0.91%	-1.56%
400	-0.33%	-0.44%	-0.88%	-1.21%	-2.08%

Polycrystalline Diffraction

Many materials, especially metals, form as very small crystal grains, and then amalgamate into a polycrystalline structure. Diffraction patterns from small grains broaden the individual diffraction spots beyond the incident beam size, and the presence of many randomly oriented grains results in overlapping sets of diffraction patterns, all with the same origin as they all come from the same incident beam. Typically these results in a complete set of diffraction rings, one for each family of Bragg planes. **Figure 2-8** shows diffraction rings from a thin (20 nm) sample of polycrystalline gold illuminated with a 16 kV magnetically focused electron beam. The bright inner ring is (111), followed by (200), (220), and (311), with (331) visible at the edge. In this case the brightness of the (111) ring is due to preferred orientation due to growth on rock salt (refer to **Table 2-4**).

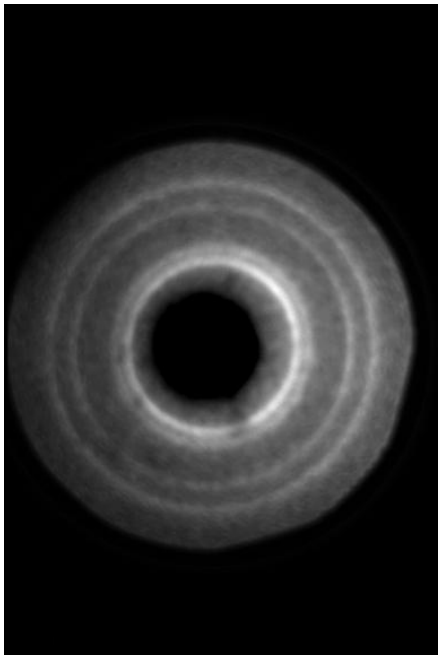

Figure 2-8 Polycrystalline gold diffraction rings.

Multiplicity of Reflections and Ring Brightness

The relative brightness of polycrystalline diffraction rings can be estimated by the multiplicity of diffraction spots that can appear in a given ring, which is essentially a combinatoric problem. The greater the multiplicity, the brighter the ring is.

Table 2-3 Multiplicity is the number of different diffraction spots in a ring.

Pattern	Multiplicity
a00	6
aa0	12
aaa	8
ab0	24
abb	24
abc	48

Table 2-4 Kinematically permitted orders for FCC crystals, and their multiplicity

	Distance			Close
(hkl)	h^2+k^2+l^2	Order	Multiplicity	Pairs
111	3	1	8	14
200	4	2	6	
220	8	3	12	
311	11	4	24	32
222	12	5	8	
400	16	6	6	
331	19	7	24	48
420	20	8	24	
422	24	9	24	30
500	25	10	6	

Brilliance

The definition of probe beam brilliance relevant for time-resolved diffraction is:

$$B = \frac{nN\rho\eta}{\Delta x^2 \Delta\theta^2}$$

where n is the repetition rate, N is the number of photons or electrons emitted by the source at each shot and in a .01% bandwidth, ρ is the geometric factor, i.e. the fraction of the diffraction pattern seen by the detector, η is the quantum efficiency of the detector, Δx is the size of the source, $\Delta\theta$ is the emitting angle of the source. This definition takes into account the whole experimental set-up including the type of detector used in the experiment.

The optimum UPED brilliance can be calculated with the following parameters:

$$\Delta\theta = \left(\frac{\Delta E}{E}\right)^{1/2} = 3 \text{ mrad} \; ; \; \Delta x = 10 \, \mu\text{m} \, ,$$

with the geometric factor ρ and the quantum efficiency η equal to one. The number N of electrons per shot is 1000, which permits a less than 100 fs time-resolution (see later). To create such a small number of electrons, a simple oscillator is sufficient, with a repetition rate of 100 MHz. However, the pump needs a high energy that will keep the repetition rate to a lower value: ~100 kHz. With this value used for the calculation,

$$B = 10^{11} \text{ electrons/s.mm}^2\text{.mrad}^2\text{/ per .01\% bandwidth.}$$

This compares very favorably with first generation synchrotron x-ray sources when the relative electron/x-ray scattering cross sections are taken into account[36]. At 1,000 electrons per pulse, with pulse duration of 100 fs, the periodic electron current at the

sample is about one milli-Ampere; this is millions of times greater than the continuous currents found in transmission electron microscopes.

Technique/ Feature	*UPED: Ultrafast PhotoElectron Diffraction*	*PXD: Plasma Produced x-ray, Thomson scattering*	*SXD: Synchrotron/Streak Camera*
Brilliance Photons or electrons /s.mm^2.mrad^2/0.01% bandwidth	**10^{11}**	**10^4 - 10^5**	**10^{11}**
Temporal Resolution	**< 30 fs**	**~150 fs**	**> 200 fs**
Characteristics	Thin samples Gas reactions Surface studies Probing volume < excited volume	Heavy atoms Bulk studies Probe penetrates deeper than light pump, except at glancing angles	

Figure 2-9 Potential time-resolution of the different techniques; electrons are suited for thinner samples, surface studies, gas reactions, and shorter interaction times. X-rays are more suitable for heavier atoms and bulk studies; for surface studies they are effective when used at glancing angles.

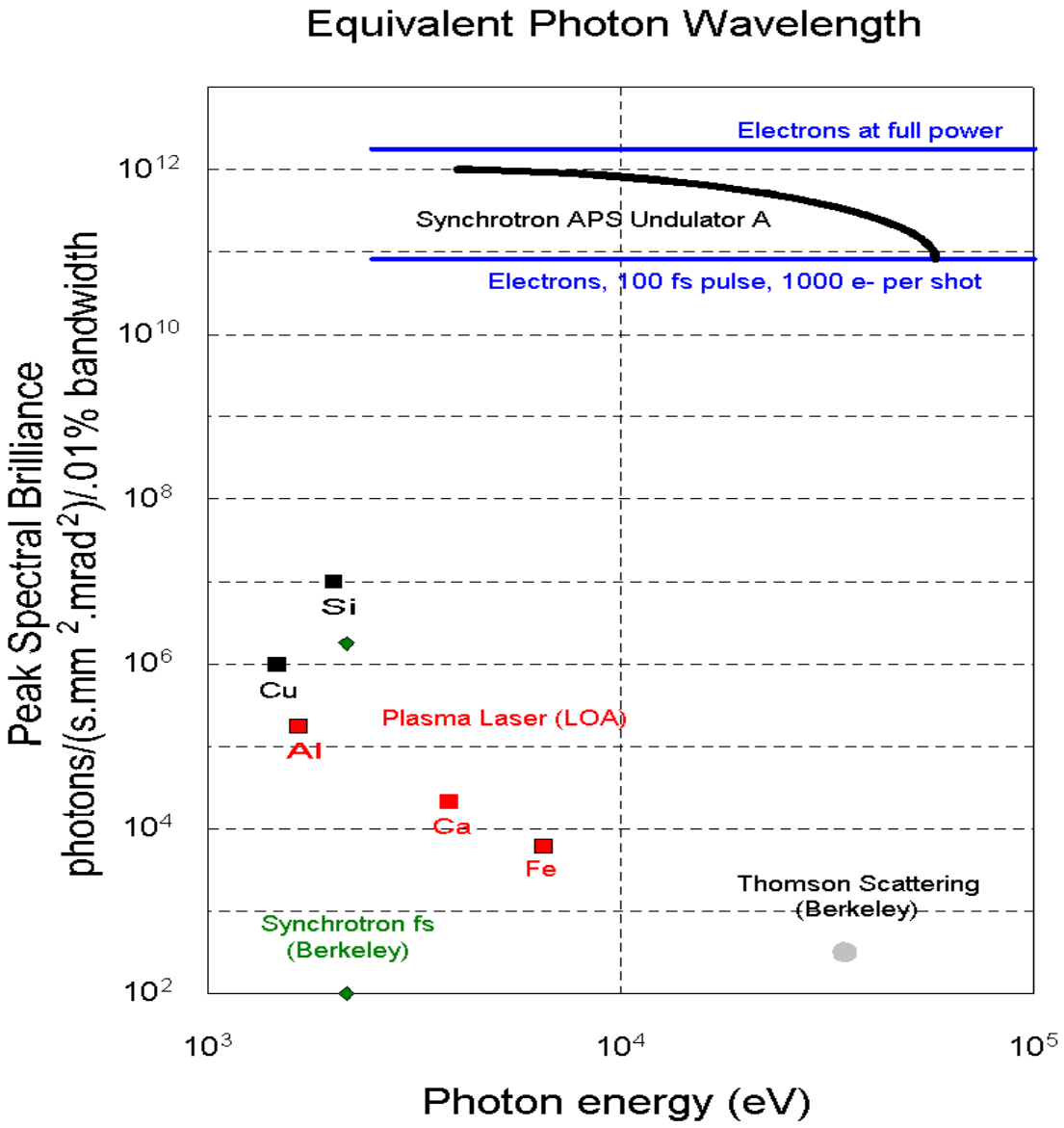

Figure 2-10 Brilliance comparison by equivalent photon wavelength; ultrafast electrons offer superior brightness circa 1999. The synchrotron brilliance is from the first generation; recent improvements have increased synchrotron brilliance to 10^{22}.

Chapter 3

Design of an Ultrafast Photo-Electron Diffractometer

Figure 3-1 Photocathode and anode of the ultrafast electron gun, showing 30 kV electrical contact plate and 30 nm of gold sputtered onto a fused silica negative lens below; the grounded anode tube with 400M gold extraction grid leading up to a 200 um pinhole exit above. Operation requires an ultrahigh vacuum. The small bolts at the top are 0-80.

Basis of an Ultrafast Photo-Electron Gun Design

An ultrafast photo-electron gun[37] is more than a collection of parts. An ultrafast photo-electron pulse is generated by a corresponding laser pulse which causes the photo-electric emission of electrons from a photocathode in vacuum. The wavelength of the laser pulse must be matched to the work function of the photocathode material in order to produce electrons with near-zero initial kinetic energy, while the voltage between the cathode and anode must be applied over a very short distance so that the emitted electrons are swept up rapidly enough that there is no charge accumulation at the cathode. This requires a very high field which implies very strong forces between the coating of the photocathode and the extraction grid of the anode. The electron pulse will exit the anode via a pinhole aperture which defines its diameter, and will self-expand due to Coulomb repulsion as it travels to the sample; fewer electrons in the pulse means that the self expansion will be slower, while minimization of the travel time will also limit the self-expansion and hence the pulse duration at the sample.

Characteristics of the Electron Gun

The current photo-electron gun uses sputtered gold as the photo-cathode material, of approximately 30 nm thickness. The laser pulse is 150 fs centered at 780 nm, and then shifted to 390 nm by means of a BBO frequency doubling crystal, and this is mixed with the fundamental in a BBO mixing crystal to also produce 260 nm (UV). The UV pulse is separated with a series of dichroic mirrors which are designed to reflect 97% of the 260 nm light while transmitting at 98% for narrow bands around both 780 nm and 390 nm. It should be noted that the BBO crystal orientations should be individually tuned to maximum efficiency in order to guarantee the best pointing stability. A long focal length lens (2 m) increases the intensity at the BBO crystals, and results in a focal spot of 250

μm FWHM for the UV at the photo-cathode. This has been measured by removing the pinhole from the anode so that UV which is not absorbed by the photocathode could be diffracted by the 500 LPI extraction grid in use at that time. The resulting optical diffraction pattern was captured by the MCP detector (see **Figure 3-2** and **Figure 3-3**); use of the camera equation gives an accurate measure of the internal distance from the extraction grid to the MCP detector.

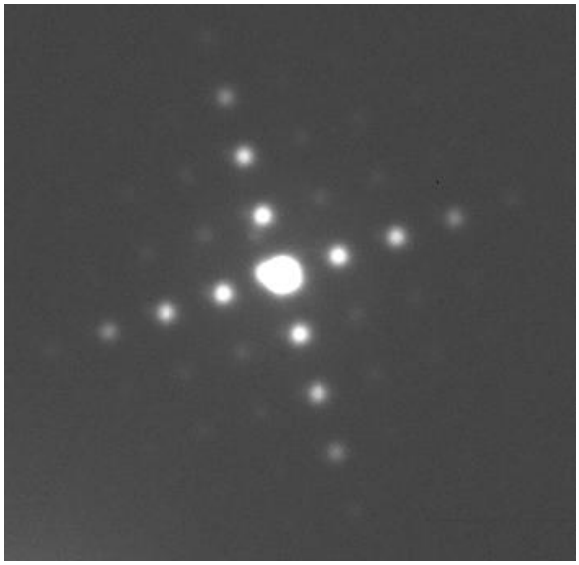

Figure 3-2 Optical diffraction of 260 nm UV pulse by 500 LPI extraction grid.

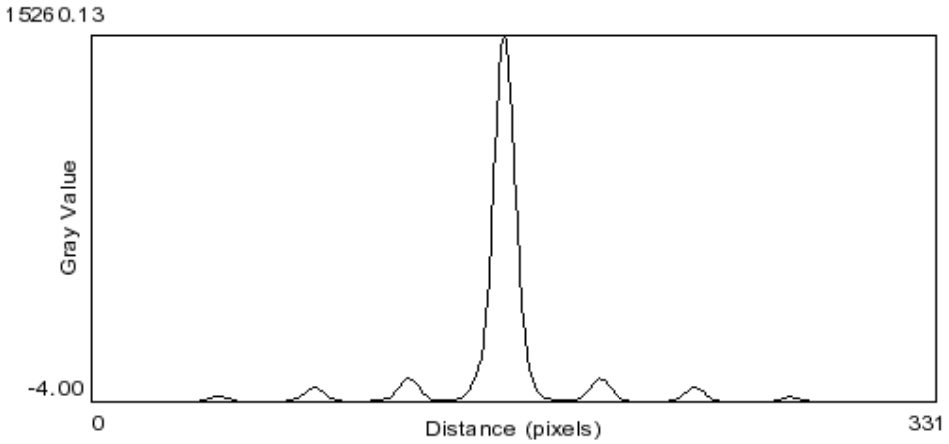

Figure 3-3 Peak spacing for 260 nm UV diffraction; FWHM= 350 μm.

It should be noted that the skin depth for 260 nm UV on gold is only 2.2 nm, so at 30 nm thickness, the UV pulse is penetrating over 13 skin depths, and is thus attenuated by e^{-13}, or over 99.999%. The existence of an optical diffraction pattern is due to the high sensitivity of the MCP and its amplification of the low signal, as well as to the very large number of UV photons, about 10^8 in even a very weak pulse.

Control of the intensity of the UV beam is by means of a wave plate and a thin film polarizing beam splitter which divides each laser pulse in a jitter-free fashion, with one pulse delivered to the UV generation line, and the other destined to be used as a pump pulse. The wave plate settings are standardized by means of digital images taken of the phosphor screen output of the MCP. Since these are all linear detectors when operating in the "good" zone, it is possible to use a calibration table based upon integrated image intensity to determine the number of electrons in a given pulse.

The initial calibration was performed by taking a series of images at different wave plate settings, ensuring that there was no "blooming" in the CCD camera by adjusting the integration time. Different voltage settings of the MCP plates where then recorded at each wave plate setting, and relative amplification calculated. These measurements were linear in terms of peak intensity and mean intensity, though with different slopes. Then the anode pinhole was replaced with a Faraday cup, and internal leads were run through connectors on the vacuum flange to a Keithly 610A electrometer capable of measuring currents in picoAmperes. Repeating the wave plate settings, electron beam currents were determined, and dividing by the laser repetition rate of 1000 Hz gives the mean charge per pulse in Coulombs, from which the number of electrons is determined. The efficiency of the particular photocathode was calculated at 3.3×10^{-5} electrons per UV photon, and combining this with the wave plate intensity calibration provides a good estimate of the number of electrons per pulse. Since the detectors are linear, integrated intensity or peak intensity measurements of the electron beam can be used update the calculated number of electrons per pulse for replacement photocathodes without

repeating the Faraday cup/electrometer measurements. Rotation of the wave plate settings gives a relative change by a factor of from 100% down to 1% intensity.

Wave Plate Analysis of November 17, 2007: 26 kV (200 um pinhole)

Wave Plate Setting for UV	Ratio	e-beam Mean Intensity
WP020	96.66%	2589
WP030	100.00%	2678
WP040	74.30%	1990
WP050	38.16%	1022
WP060	15.08%	404
WP070	3.56%	95
WP080	2.79%	75

Table 3-1 Electron beam relative intensity by wave plate setting, November 17, 2007.

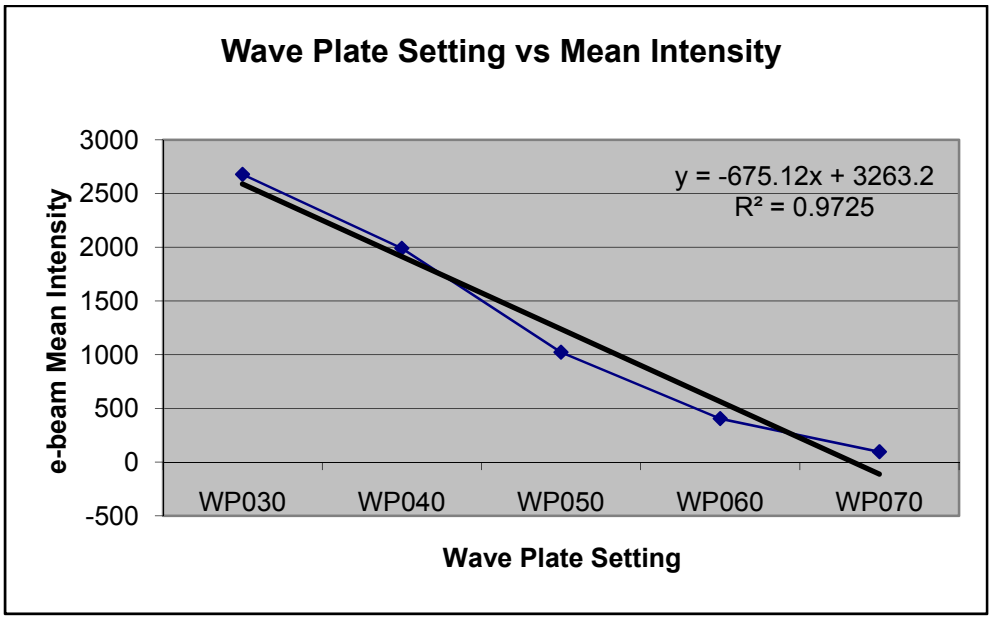

Figure 3-4 Wave Plate Setting vs. Mean Intensity is very close to linear when the two end points are omitted.

Calculating Electron Pulse Duration

Electron pulse duration depends upon the number of electrons in the pulse, the applied voltage and length of the cathode-anode region, and the distance from the extraction grid to the sample[14 15], though there is some disagreement between the experts as to the details, for short distances their formulations agree. The derivations depend upon solving the Poisson equation, $\nabla^2\Phi = \rho/\varepsilon_0$, based upon boundary conditions guessed at from the laser pulse striking the photocathode. Having previously established approximate numbers of electrons as described in the previous section, the pulse broadening can be estimated by an analytic formula derived by Qian and Elsayed-Ali[14]: $Nd^2r^{-2}V^{-3/2}$, which is the number of electrons in the pulse times the square of the distance propagated, divided by the radial diameter of the electron bunch squared times the accelerating voltage to the 3/2 power. The broadening is with respect to the initial laser pulse duration, and this form is valid for short distances; otherwise it overstates the broadening.

The radial diameter of the electron pulse is controlled by the anode pinhole, and the accelerating voltage is an important operating parameter of the electron gun. Larger values of the accelerating voltage result in shorter pulse duration; a larger radial diameter means a lower electron density, while a higher voltage means that the pulse is propagating at a higher speed, and thus has less time to self-expand. This is self-evident if one is riding in the rest frame of the pulse. The remaining factors are the number of the electrons times the square of the distance travelled. The distance is determined by how the electron gun is built, and how close the sample can be positioned while still providing access to the pump laser pulse. In the current 30 kV electron gun, the cathode to extraction grid distance is 4.3 mm, for a field strength of 6.9 MV/m, the drift distance from the extraction grid to the sample is 16.3 mm. For an electron pulse with 12,000 electrons the laser-pulse replica starting at 150 fs will broaden to almost 300 fs at the

sample plane. Further broadening as it travels afterwards to the detector is immaterial, for the dynamics of the electron diffraction process are faithfully carried by the expanding pulse.

Self-Chirp

Self repulsion from within the electron bunch results in self-chirping of the electron pulse[15]. The electrons at the leading edge of the pulse are slightly accelerated, and so pull further ahead, while the ones at the back are slightly decelerated, and so fall farther behind. The ones in the middle feel intermediate forces, and seek equilibrium. If the pulse spends enough time drifting it becomes nicely chirped, and some form of compression could be applied to shorten it up significantly. Such a device has been proposed by Qian and Elsayed-Ali[38], though none has been constructed on an appropriate scale for a table-top system. Implementation of a chirp-compressor will permit the electron source to be distant from the target. This allows room for focusing optics, beam steering, and diagnostics such as a Faraday cup. This would make the diffractometer compatible with imaging applications such as an ultrafast TEM. Development of single-shot imaging with 10 nm spatial/10 ps temporal resolution by 5 MeV electrons has been recently proposed.[39] Baum and Zewail[40] propose a technique based on tilted optical wave fronts for the generation of reverse-chirped, self-compressing electron pulses. These and many related issues are examined in detail in a review article[41] by W.E. King *et al*.

Photocathode Fabrication

Photocathodes must be transparent to the 260 nm UV laser pulse. Suitable materials are UV-grade fused silica, and sapphire. The current design uses the curved surface of a 12.6 mm diameter negative lens made of fused silica. Several lenses are purchased at a time

so that spare photocathodes are available when needed. The photocathode is prepared for coating by washing in high purity acetone for 10 minutes in an ultrasonic cleaner to remove any oily contaminants, followed by another 10 minutes in high purity methanol. Gloves are used for handling. The blanks are placed in a Denton sputter coater with a gold target, and after achieving vacuum and then stabilizing the argon pressure, the coater runs a current of 40 mA for 90 seconds to produce a 30 nm coating.

Since electrical contact with the film is made by an electrical contact plate on the front side, the outer region of the coating is made thicker by covering the 90 second coating with a 10 mm diameter sapphire window left over from a previous design, and then applying a further coating of 300 seconds. This thicker film does not tear or wear during the working life of a photocathode which can be up to three months before it ruptures at the point where the UV beam strikes it. Attempting to focus the UV beam below 250 μm FWHM also leads to rapid (or even immediate) rupture, so finer beams depend upon smaller pinhole exits from the anode.

This coating procedure was adequate at 20 kV, but required further steps at 30 kV due to the increased forces of the nearly 7 MV/m electrostatic field which would pull off loosely bound nanoparticles, and then rip the film. The current procedure for toughening the film is to expose it to a germicidal UV lamp (260 nm) for 48 hours. This process improves surface adhesion of the film to the fused silica substrate. TEM examination of "toughened" thin films also showed a slight increase in particle size and an increase in the number of inter-particle connections.

Figure 3-5 Anode structure, with photocathode at left. The cutaway sections allow for close passage of the pump laser beam and allow for a very close target sample.

Anode Fabrication and Alignment

The anode is electrically grounded to the vacuum chamber, which is in turn grounded to a cold water pipe that was tested for a good earth ground. The extraction grid is a 400M gold TEM grid (2.0 mm of grid, with a 1.0 mm thicker border) which is held in place mechanically by a pair of polished tubes, one inside the other, the outermost tube being visible in Figure 3-1. The previous design used a higher density 500 LPI gold mesh and a larger tube system, but the higher forces of the 30 kV potential tended to pull it out of shape so a smaller exposed area was the solution. In addition TEM grids are easily purchased and do not need any preliminary preparation beyond cleaning.

The electron beam exits the anode structure through a pinhole which limits the size of the beam. However it is best if the intensity of the UV is selected so that the beam is barely clipped at all; this is evident from CCD images captured from the phosphor screen. If the

electron beam is overly intense the shape of the beam is clearly non-Gaussian, with the shoulders stripped by the anode pinhole.

Recall that the UV beam is focused to a small spot, and the electron beam exits through a small pinhole. This calls for an alignment of the input UV beam such that the electron beam exits through a tiny aperture. The procedure to achieve this is simple: when testing the alignment prior to a run set the electron gun voltage to 10-12 kV which causes the electron beam spot to broaden, and set the wave plate for a very intense beam. The effect is a very broad and bright electron beam spot which is easy to spot while scanning the photocathode with the final coupling mirror. Once the spot is through the anode pinhole the wave plate is turned to a less intense setting, then the voltage is stepped up, and the beam is aligned. Repeat until the final intensities are as desired, and the beam structure is round with no clipping. Normally the alignment is unchanged from day to day unless the laser has been serviced and the initial beam direction has changed slightly.

A Note on Materials

Originally all metal parts were fabricated from aluminum, and the insulating standoffs were glazed. Problems with cleaning and micro-cracks in the glazing called for a change in materials. The metal parts are now all 316 stainless steel which is robust under cleaning, including the removal of oils, and the standoffs are Macor®, a machinable ceramic which does not suffer from surface cracking. The stainless steel also takes a mirror polish.

Removal of machining oil from parts was simplified when an experienced TEM customer engineer suggested ultrasonic cleaning of the parts in the original “Mr. Clean”, a household cleaning solution which includes water soluble degreasers and surfactants as well as 0.1% NaOH, which makes it unsafe for aluminum because it will vastly increase surface absorption of gases. But it works great for stainless steel and ceramics, including

Macor. Follow this degreasing wash with a long rinse with running water, and then ultrasonic cleaning with acetone, and then methanol to remove the acetone residue.

Previous Electron Gun Designs

The immediate predecessor electron gun shared many of the design features, but was designed for 20 kV and had a substantially longer acceleration gap. When the high voltage feedthrough and cables were upgraded for 30 kV operation a series of tests were performed to establish the maximum voltage which was supported. At 24 kV failure of the extraction grid was common, with the edges of the mesh pulled from its mechanical clamp. In addition, photocathodes had to be replaced almost weekly due to rupture near the edges of the electrical contact. **Figure 3-6** shows a parts explosion for this model. The slot on photocathode fixture is for compression as the slightly tapered fixture is drawn into place; this gives a tight mechanical grip on the photocathode. A light dusting with "*dry moly*", MoS_2, was required to overcome friction and avoid vacuum welding. In order to make electrical contact with the photocathode coating, the coating was applied to the entire fixture in two stages. The first coating was 90 seconds sputtered, and for the second coating the middle of the fused silica flat was blocked and 300 seconds was sputtered over the entire fixture. A good coating would have electrical resistance edge-to-edge of less than 6 Ω. Ruptures would occur where this coating went over the edge of the flat; this was replaced by a contact plate for the later model. **Figure 3-7** shows actual parts. The problem of the gold mesh being deformed by the high field strength was solved by making the extraction area smaller, less than 2.0 mm in diameter, and improving the mechanical compression.

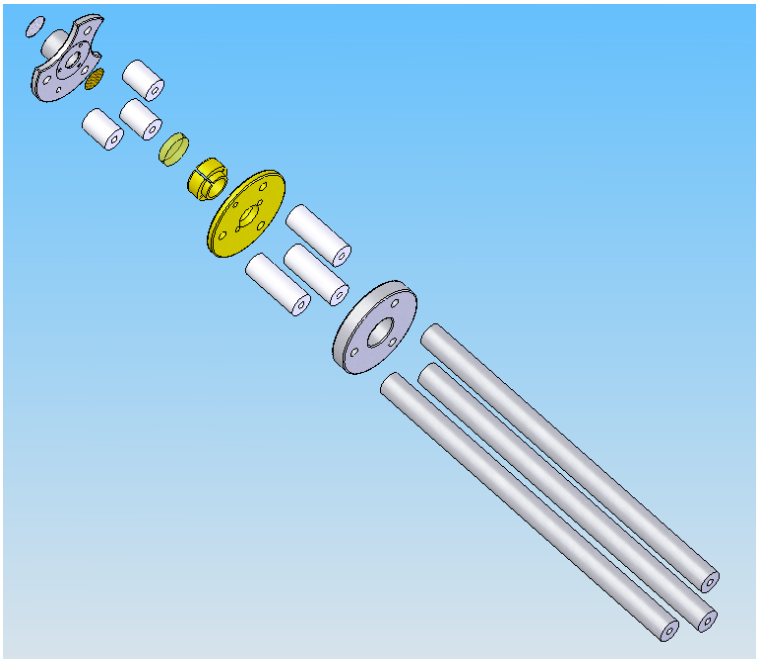

Figure 3-6 20 kV electron gun parts explosion; produced 2-5 ps electron pulses.

Figure 3-7 Left: Photocathode was held in a friction fitting. Right: Anode extraction grid was 500 LPI gold mesh.

The earliest versions included a magnetic focusing solenoid which was mounted external to the vacuum chamber around a nipple midway between the electron gun and the sample. This was used to collimate the electron beam, resulting in finer diffraction patterns as seen in **Figure 2-8**, but required an additional 16” of travel for the electron pulse, making it 200-300 ps in duration. When this became fully understood it was clear

that the magnet would have to go into the vacuum chamber, but the in-vacuo coil was not strong enough to collimate the beam and was abandoned in order to reduce the beam drift distance. The problem was that as the current increased, the Kaptan® polyimide film insulation of the wires out-gassed faster than the pumps could clear it, and the vacuum was degraded. A workable in-vacuo solenoid must be UHV compatible, or else isolated from the vacuum, and probably requires water cooling to remove the heat in either case.

Transmission and Reflection Modes

The description to this point has been of transmission mode, similar to that used in an electron microscope. With a few adjustments it is also possible to operate in reflection mode, similar to a RHEED system. These adjustments were made in order to accommodate a bismuth sample provided by Davidé Boschetto of the *Laboratoire d'Optique Appliquée* LOA-ENSTA, which had previously been used for time-resolved x-ray diffraction experiments. This required addition of high-voltage deflector plates mounted to the flange holding the MCP detector, a new sample holder design that could rotate to grazing incidence with the electron beam, and a modified optical path for the laser pump beam perpendicular to the electron beam. Preliminary bismuth experiments were carried out, but the diffraction pattern was not that of a clean Bi surface – the previous x-ray experiments did not detect a thin layer of bismuth oxide on the sample; however, the electron beam probes only the topmost layers in reflection, and saw only the bismuth oxide.

Additional samples tested include highly ordered pyrolitic graphite (HOPG), see **Figure 3-8** and **Figure 3-9**, and thermally evaporated gold on silicon substrates. RHEED requires very flat samples; the nanostructure of the sputtered gold was not smooth enough to obtain good RHEED patterns.

Figure 3-8 Sample holder with HOPG (highly ordered pyrolytic graphite) sample for reflection mode diffraction. Note the horizontal channel used for grazing incidence.

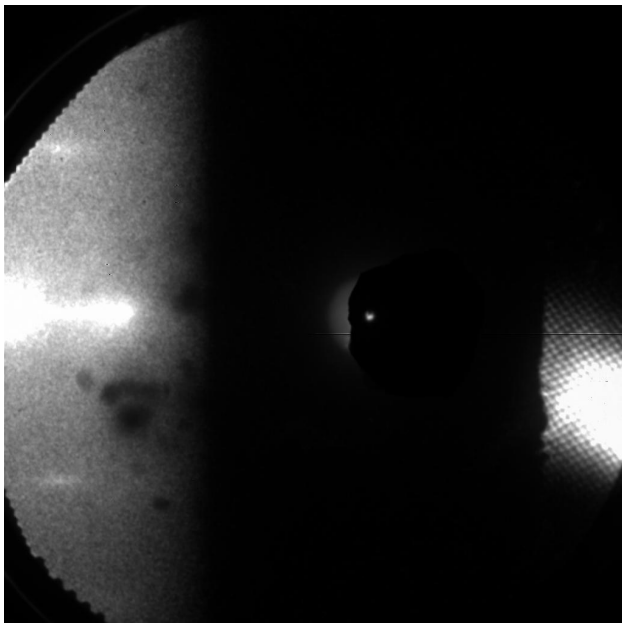

Figure 3-9 HOPG RHEED streaks at left; the cross hatched region at the right is a focused image of the extraction grid due to mis-focus of the electron gun.

Chapter 4

Experimental Determination of Time-Zero

Importance of Time-Zero

In order to make sense of any time-resolved experiment the before-and-after time series must be clear. The division point is "time-zero", and there is real information to be gained if it can be established independently of the experiment:

- Acts as a check on the proper operation of the entire system; it is a diagnostic experiment
- As a diagnostic, it verifies the pump-probe alignment; the following experiment uses the same setup after a vertical shift
- Allows collection of data over an appropriate time period prior to "the event", sufficient for background statistics and the calculation of signal-to-noise ratios
- Ensures capture of any "pre-event" effects, perhaps due to laser pre-pulses or residual heating or material breakdown
- Facilitates setting the time step appropriate to the dynamics being monitored, with perhaps finer steps closer to the start
- Helps in setting up a re-run, even if changes have been made to the internal or external setup because the fundamental conditions can be repeated

With an all-optical setup, time-zero is established with an arrangement similar to an autocorrelator: both pulses are sent through the same location of a doubling crystal, at oblique angles, and when the pulses overlap in time an additional, frequency doubled beam appears midway between the original beams. When the doubled beam is brightest spatial and temporal overlap is best. Unfortunately this technique does not work when one is a laser pulse and the other an electron pulse. Direct Thompson scattering[42] of the

electron pulses by interaction with the laser pulses can be tried, but the cross sections are too small unless the electron density is enhanced along with the laser intensity at the spatial intersection. These conditions are inappropriate for most time-resolved experiments because the increased electron density increases the electron pulse duration greatly, and the overly intense laser pulse will vaporize the sample.

Indirect methods include special features in the system such as a pinhole[43] or a sharply pointed needle[44] which will drive off electrons at the tip when struck by the laser pulse, and the charge buildup will deflect the electron pulse around the tip. Another is to use the laser pulse to ionize some material which will interact with the electron pulse; this is especially convenient for gas phase experiments[45] where it is the gas which is ionized. These methods can be performed without changing the focus of the pump beam; the only change is a temporary increase in the power being admitted to the pump line. The traditional method has been to monitor a target for a solid-to-liquid phase change; this requires repetitions of single-shot experiments, and their associated target manipulator. Another method that has been suggested[46] is to use a photoconductive switch so that the laser pulse "connects" the amplified electron beam charge to an external oscilloscope, allowing a rapid determination of time zero as the pump delay line is rapidly scanned. Other ingenious approaches will no doubt be found, as has been shown in "Clocking Femtosecond X-Rays"[47]; SLAC was able to compress an ultra relativistic (28.5 GeV) electron bunch electron with over 10^{10} electrons to 80 fs using a magnetic chicane.

Optical Alignment

Optical stability is crucial. The alignment of the pump laser beam includes reflection from a cube-corner style retro-reflector mounted on a computer controlled translation stage. The laser beam must enter and leave parallel to the optical table, and to its own path. This ensures that the pump beam focal point won't wander about as the stage is

translated. This is verified by monitoring the pump laser illuminating the cut wire target; no motion whatever is observed.

Determination of Time-Zero

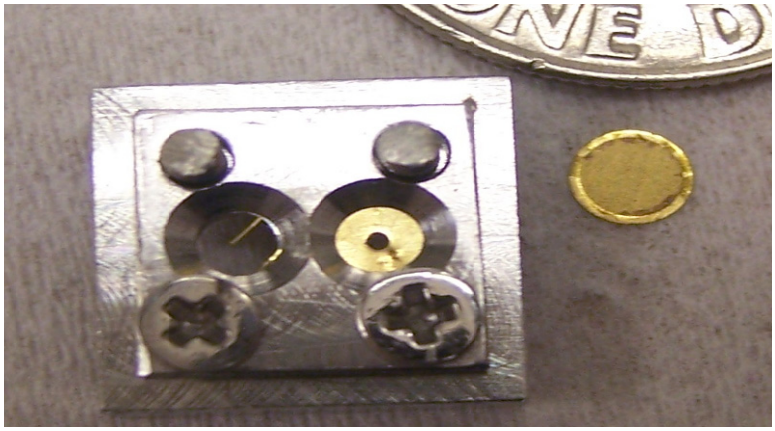

Figure 4-1 10x10 mm sample cartridge. Right: 600 um aperture w/gold film. Left: cut wire target for time-zero. The bolts are size 0-80.

The method used[48] is a variation of the ionization process, though the original intent was more like the sharply pointed needle. It begins with the requirement to spatially align the system, for which an aperture mounted a fixed vertical distance from the target sample is used; see **Figure 4-1** and **Figure 4-2**. The electron beam has previously been aligned as described in Chapter 3, and is treated as a fixed beam. The sample manipulator is used to roughly center the beam on the lowest target, which is a 400M gold TEM grid. The target is then lowered 5 mm to bring the gold 600 μm TEM aperture to the electron beam, and aperture is moved vertically and horizontally until it is exactly centered on the electron beam. Since the pump and probe beams enter with a 45 degree angle between them, the sample holder is rotated slightly to split the angle evenly between them. The pump beam is now unblocked, and if the setup is unchanged from previous days it will already be centered on the aperture; if not, the sample holder is raised 5 mm to the 400M TEM grid, and the pump laser beam is roughly centered on that.

Figure 4-2 Rear view of sample holder with cartridge mounted. The bottom most aperture holds a gold 400M TEM grid; 5.0 mm above it is a gold 600 µm TEM aperture, and above that is the sample cartridge. Each of the TEM grid holder cells is centered on the same vertical line.

The TEM grid diffracts the pump beam, and the diffracted beamlets are collected by a lens which focuses them onto the heavily filtered CCD chip of a small auxiliary camera. This produces an image of the pump beam illuminating the TEM grid, and having once brought this image into focus it will remain so. From this image the pump beam diameter at the sample plane, FWHM, can be determined by simply counting the TEM grid squares, and combining this with the power of the beam and the laser rep rate of 1000 Hz, the fluence of the pump beam applied to the sample can be calculated in mJ/cm^2. This is typically under 5 mJ/cm^2 in order to avoid damage to the material during a long data collection run.

If the pump laser beam is not found by the camera directly, another small camera which images from the face of the sample holder is used to find where the pump laser beam is striking, and the coupling mirror is slightly adjusted to put the beam through the TEM grid. The alternative is to use an IR viewer and look around inside the vacuum chamber; cameras are much easier and safer because the eyes are never exposed to stray reflections.

Having spatially aligned the beams, and if necessary measured the pump beam diameter, the sample holder can be lowered further if the cut wire target is being used for time-zero determination. This is from a special TEM grid made of 80 μm parallels, most of which have been cut away by means of a razor blade under a microscope, leaving a cut wire of 80 μm diameter with the tip roughly centered in the aperture. When this cut wire is used it replaces one of the target samples. Since the beams are co-centered at this point of the procedure, it is only necessary to bring the wire tip into the center of the pump beam using the sample plane imaging camera. This automatically brings the tip into the electron beam, though this can be verified by increasing the intensity of the electron beam by means of the wave plate setting. Next the tip is moved slightly so that it is closer to the edge of the electron beam, and the laser beam is manipulated to bring its center back onto the tip. This results in the greatest deflection of the electron beam, and hence is easiest to interpret.

It is worth noting that the same time-zero is determined regardless of the intensity of the electron beam; the detection is approximately the front edge of the pulse, and the front edges are the same regardless of the number of electrons in the pulse.

The cut wire worked very well at first, but then the deflection effect slowly grew less and less. The same had been noted when the target was the edge of the 600 μm aperture, and

later with the 400M grid. The reason for this decay was not obvious at first, but eventually it became apparent that in each case the dominant process was not multi-photon emission, or induced currents, but instead it was a surface ionization process, a form of laser cleaning process. As the surface became cleaner and cleaner, there was less debris available to ionize and knock off, so the deflection signal became weaker and weaker. It is easy to restore a target: just aim the laser at a fresh spot, or replace the target, or brush it with a (tiny) bit of colloidal silver paste and acetone.

Having prepared the run, it is now necessary to take a series of shots, alternating with the pump beam blocked and unblocked. The CCD camera records an image of the central electron beam; the remainder of the image field need not be recorded. The camera integration time can be as fast as one second; better results are obtained by repeating each position five times, or not quite as good, increasing the integration time to five seconds. The time required to scan 140 ps is less than an hour, followed by a brief analysis of the data. Pump power is adjusted to generate a fluence of 5-10 mJ/cm^2 at the target; this typically results in pump beam intensity slightly above 10^{10} W/cm^2.

The data are analyzed by calculating the centroid (first moment) of the intensity distribution of the central beam image for each shot of each position. If shots have been repeated, the centroids are averaged together. From them the difference in the centroids between the heated and unheated shots is computed and the time series is plotted. A typical deflection chart is shown in **Figure 4-3**. Time-zero is the last point prior to where the deflection has started.

Extensive experience with this technique has shown that changes in the measured time-zero are less than one picosecond from day to day; when multiple shots are taken at each step and the positions averaged, then the change is on the order of 0.5 ps.

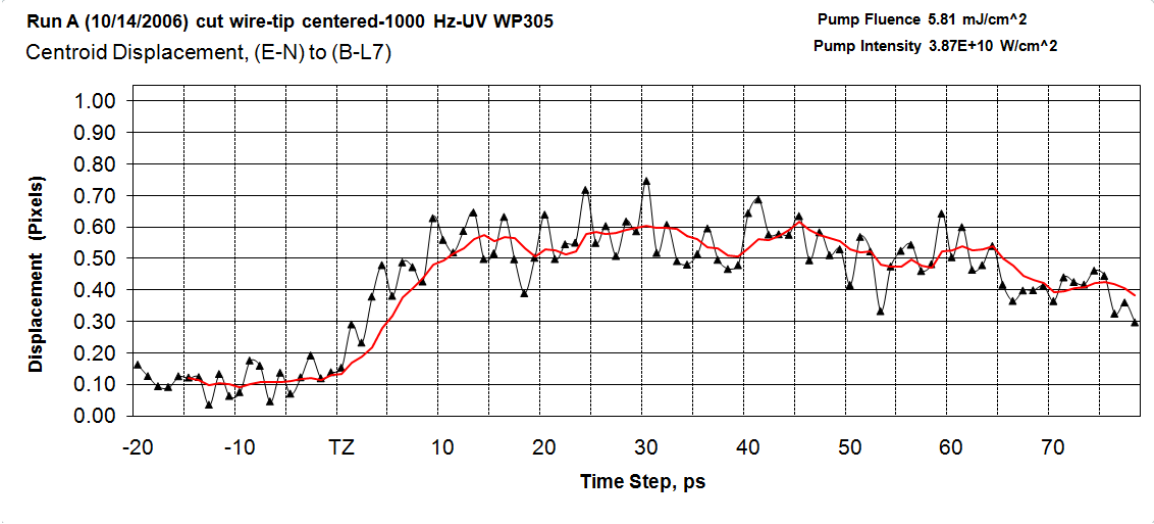

Figure 4-3 Picosecond time resolution for a 300 fs electron pulse of ~9,000 electrons. Time-zero is at T=221 ps on this centroid deflection chart. The red line is a 5 point moving average.

Figure 4-3 clearly shows the effects of heating, but it is difficult to determine time-zero precisely from the graph. An alternative presentation, where the actual centroids are plotted on an XY chart is more easily analyzed, see **Figure 4-4**. Time-zero is the last point inside the smaller "circle of confusion" on the right; these are the motions of the beam centroid prior to the pump pulse hitting the target. The circle of confusion to the left is significantly larger; the transition time of 3 ps is much longer than the actual pulse duration which is estimated at 300 fs for this pulse of about 9,000 electrons. The transition times are consistently repeated for a given electron beam intensity and hence are related to the number of electrons in the pulse, and the pulse durations, but the exact relationship has not been worked out. Systematic testing has shown that time-zero is not shifted by changing the electron beam intensity, though the transition times increase with the number of electrons. Changes to the electron gun potential do shift time-zero as expected, about 4 ps per kV near 30 kV.

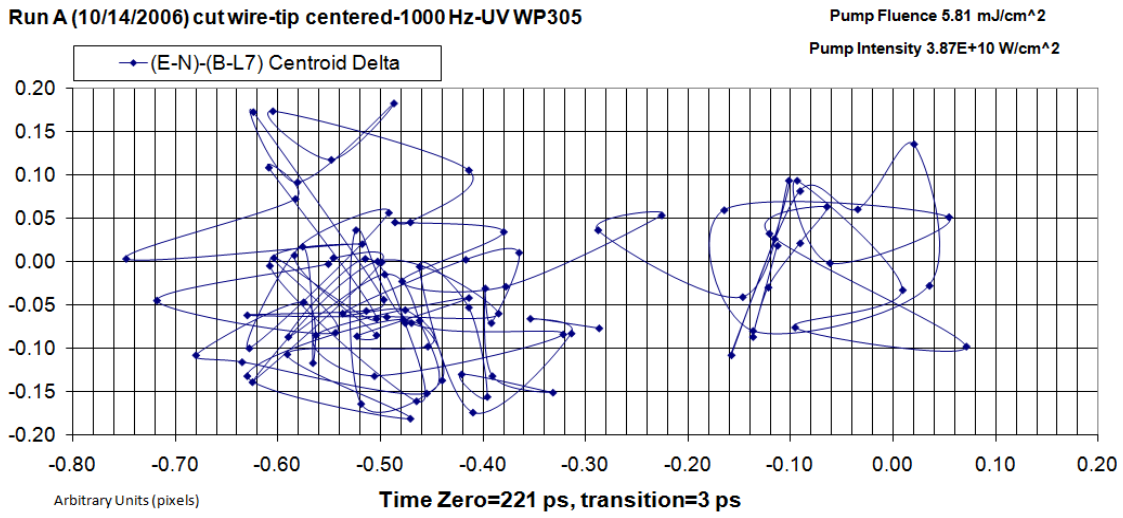

Figure 4-4 Beam centroid moves from right-to-left on this motion-tracking chart. The total motion is about 30 um (0.5 camera pixels), or about 10% of the electron beam FWHM diameter. The changeover took 3 ps.

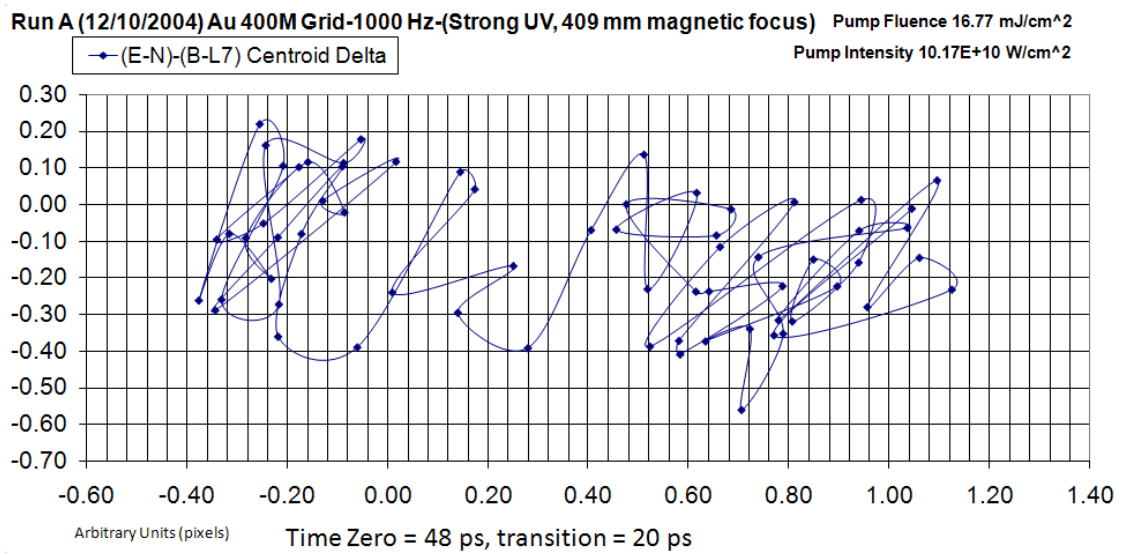

Figure 4-5 Beam centroid motion for 20 ps pulse from older electron gun design running at 19 kV; number of electrons was over 250,000, the drift distance was 409 mm, and the changeover was much longer at 20 ps.

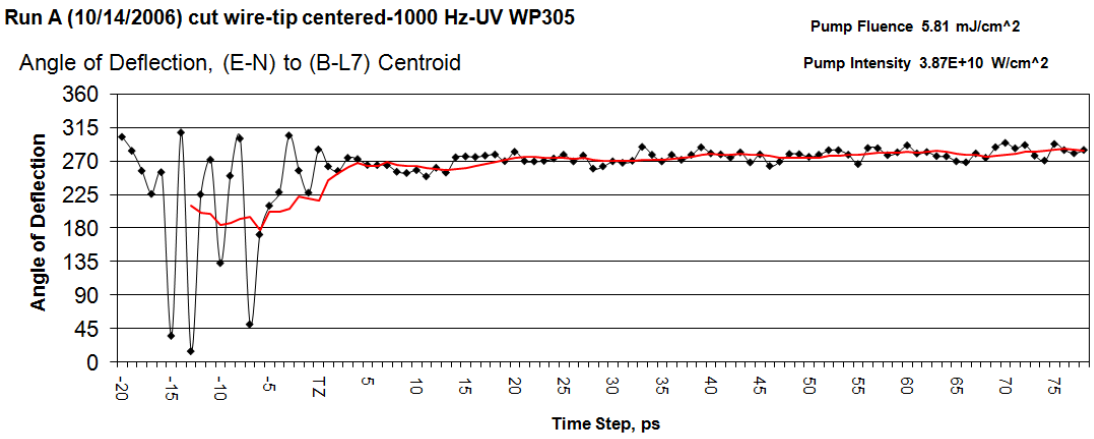

Figure 4-6 Angle of deflection chart showing a definite direction of motion for the centroid after time-zero. The red line is a 5 point moving average.

Though the actual deflection builds up slowly, the direction of the deflection holds a constant bearing for up to 100 ps or more; prior to time-zero there are small fluctuations in direction of the beam centroid; see example in **Figure 4-6**.

Finding Time-Zero When Lost

A spreadsheet is maintained which has the absolute positions of each mirror and lens on the optical table, recorded to the nearest 1/8" to the actual beam path. From this information the beam times are calculated for both pump and probe, starting at the beam splitter. Both beams are followed into the vacuum chamber, where allowance is made for the differences in speed between electrons and photons. This "dead reckoning" system allows time-zero to be rapidly found after optical changes are made, or the electron gun is modified. Time-zero is usually within an inch of the calculation.

However when the entire lab was shifted to a nearby room a subtle error was made in the transcription of the new optical layout to the spreadsheet which resulted in the total loss of time-zero. An alternative method was employed to find its physical location[49]. The

vacuum chamber was opened to the air by removal of the electron gun anode and cathode, as well as the detector. A very short focal length lens was installed in the pump beam close to the tip of the electron gun which ionized a small volume, which appears as a bright “bead of air”.

Time-zero was found by “moving” this ionization bead into the path of the probe beam and imaging this point onto a camera. This showed an interference pattern between the probe beam and the ionization bead when the delay line was moved to the correct relative position, see **Figure 4-7**. Movement of the delay stage showed that the ionization bead was 600 fs in duration; calculating the center, and allowing for the speed of the electron beam, the actual value of time-zero was recovered, and the error in the spread sheet was found and corrected. The x-y coordinates of two adjacent mirrors had been inverted, leading to an error of 15”.

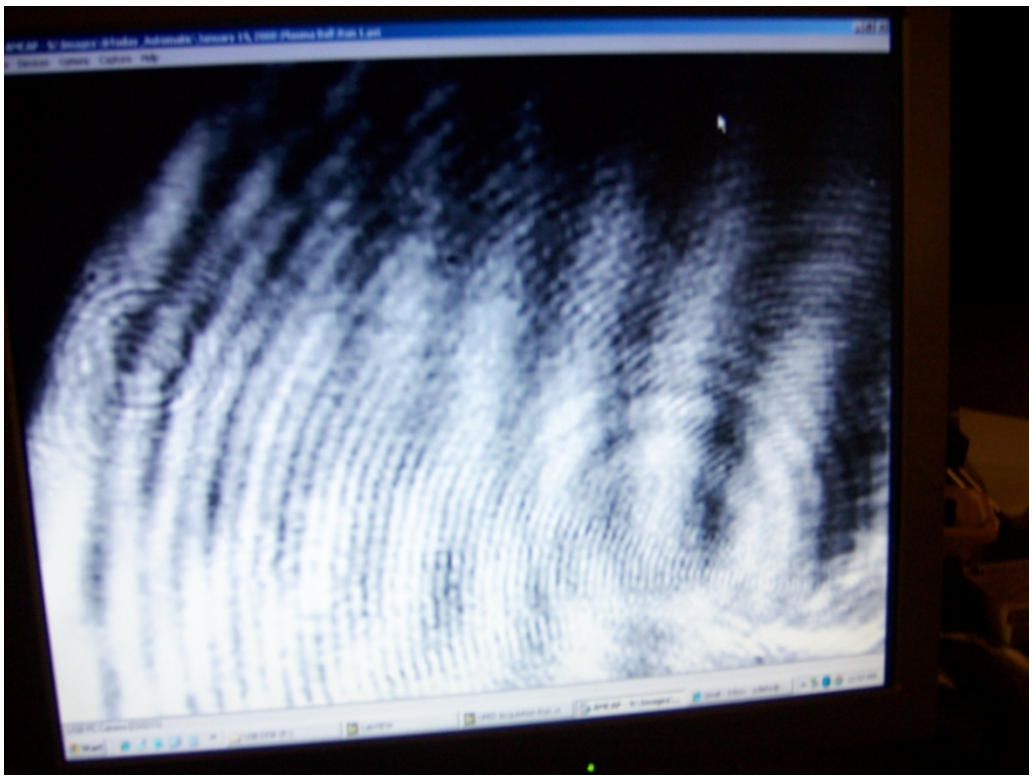

Figure 4-7 Self-interference of the probe beam as it passes through the ionized air bead. The interefernce bars of interest are the large zebra stripes; the circular patterns are from the camera optics.

Chapter 5

Ultrafast Experimental Results

Analysis of Experimental Data

Ultrafast photo-electron diffraction is a field under continuous development, and data has been acquired at various stages of development of the technique. Each of the experimental runs described here had a similar aim: to detect the transient effects of non-destructive laser heating of a thin film by means of changes in the electron diffraction pattern. In particular, the data was examined for changes in peak position (indicating strain or thermal expansion) and changes in peak amplitude (Debye-Waller effect due to heating) for each of the statistically significant peaks, as well as changes in the proportion of intensity scattered between the peaks.

A number of experimental runs were made in 2003, prior to the development of an independent method for the determination of time-zero. A 15 nm sputtered gold on amorphous carbon film was subjected to an intermittent laser fluence of 5 mJ/cm^2 with the pump being advanced 10 ps per step. The (311) peak from **Figure 5-1** shows heating of about 25 °C, based on the relative reduction of the peak amplitude. The electron pulse was about 200 ps in duration, and the data were quite noisy, in part due to the use of copper TEM grids. The excess noise with the copper grids was later traced to a coating applied by the manufacturer to prevent oxidation; the laser heating pulses ionized portions of the coating which was amplified by the MCP detector. Following the analysis of this dataset two goals were established: reduce the noise, and reduce the pulse

duration. It took about a year to accomplish both goals; in addition, the method for finding time-zero (Chapter 4, page 54) was developed and successfully tested.

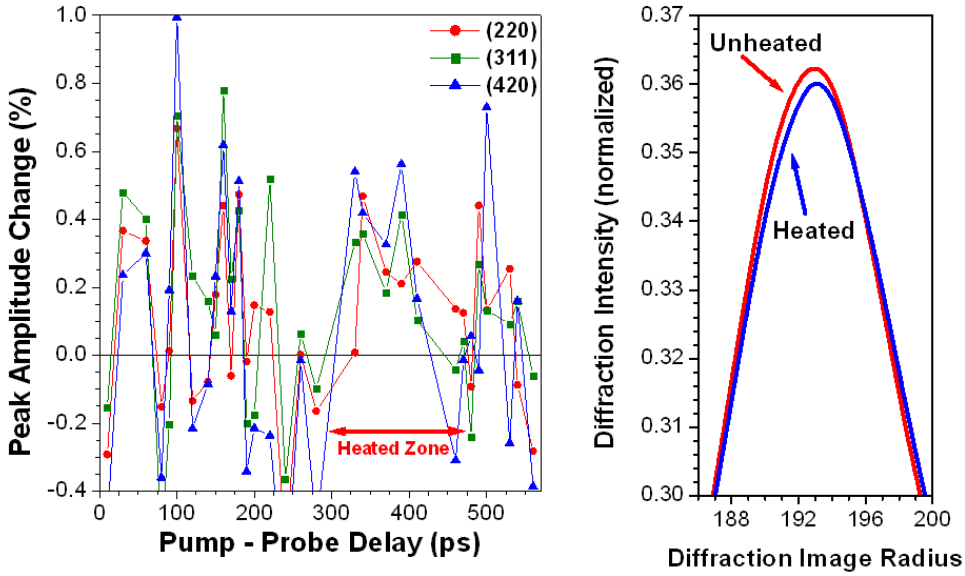

Figure 5-1 Debye-Waller heating of ~25 °C with 200 ps electron pulse. Error bars were not calculated. The graph on the right is for the (311) peak, and shows a reduction in peak amplitude.

Dataset from 9 nm Platinum Film

After a number of improvements to the electron gun, and significant improvements to the S/N ratio, a series of time-resolved heating experiments were run in October-November 2006. These were unsuccessful due to problems with the polycrystalline gold films and the electron gun. The lab was moved in December 2006 and further improvements were carried out on the electron gun intermittently with the search for the lost time-zero. Time-zero was recovered in January 2008, and upon completion of repairs to the MCP and preparation of improved samples in platinum by Codrin Cionca[50], time-resolved experiments resumed in April, 2008. Good results were obtained quickly for a laser fluence of 2 mJ/cm^2 and a target of 9 nm thick polycrystalline platinum mounted on a 400M gold TEM grid. The electron gun was operated at 30 kV, and the wave plate

setting and integrated intensity estimates are 50,000 electrons per pulse, which corresponds to an electron pulse of ~600 fs.

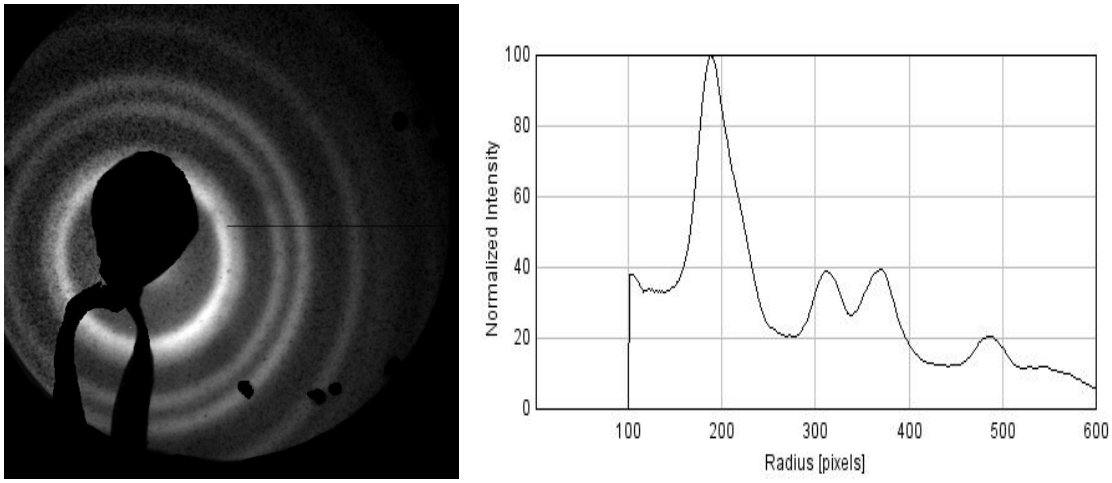

Figure 5-2 Polycrystalline platinum film, 9 nm. Diffraction image and integrated amplitudes for (E-N) images. Rings (111), (220), (311), and (331) are very clear; (200) is on the shoulder of (111).

Preliminary Time-Series Analysis

Having generated the azimuthal averages (**Figure 5-2**) for the heated and unheated platinum images, the data of each type were averaged together for each time step and plotted as a time-series. **Figure 5-3** shows the diffraction amplitude data near the (311) peak for several different pixels, corresponding to slightly different diffraction angles.

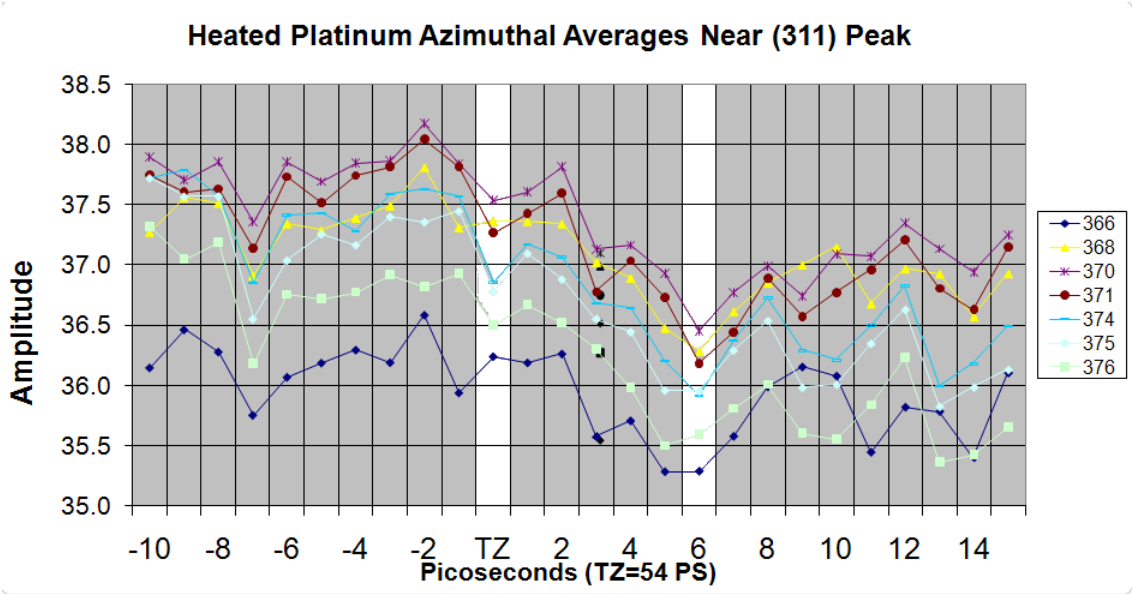

Figure 5-3 Azimuthal averages for heated platinum film, 9 nm, from April 16, 2008 run. Laser fluence was 2 mJ/cm^2. Time-zero was previously and independently determined to be 54 ps. The white background highlights the changes over the first six picoseconds.

Prior to time-zero at 54 ps there is a small jiggling of the relative amplitudes of the pixels; this is possibly caused by shot-to-shot variations in the laser pulse energy. Starting at 54 ps, the independently determined time-zero, all of the intensities decline by about 5%, reaching a maximum loss after 6 ps. Different pixels recover at different rates, and there appear to be some oscillations. The film thickness is 9 nm, and the speed of sound in platinum is 2680 m/s = 2.68 nm/ps. Thus a round trip through the film is about

6.5 ps. The conclusion is that this feature is acoustic in origin – perhaps the film is being driven by the pressure of the light pulse.[51]

In addition there is some jiggling of the sequence of the pixels, so there may be some heating going on, causing the diffraction peak to shift. Consideration of the relative shift of pixel 366 against pixel 375 supports the idea that the crystal is expanding. This run was not long enough to determine the total relaxation time, and the time steps were not fast enough to track the oscillations.

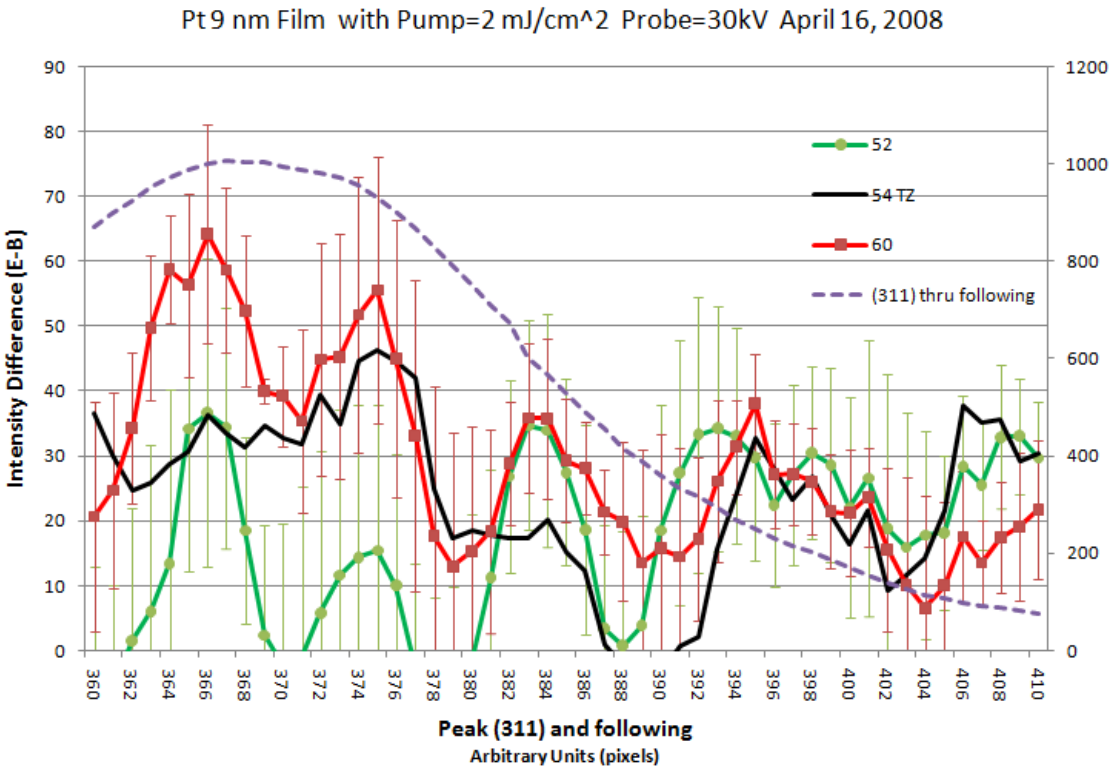

Figure 5-4 Error bars (2 x Standard Error) for diffraction intensity of three different times. April 16, 2008 dataset. The lines correspond to times at 52 ps, 54 ps (time-zero), and 60 ps; 60 ps is the time of maximum change.

Figure 5-4 shows the diffraction amplitudes for the (311) peak (and the zone past that peak shown as a dashed line) for three different times: (52 ps) is prior to time-zero, and shows less variation, (54 ps) is time zero, and is shows an increase at the peak, but not in the trough, while (60 ps) shows a larger variation, and a marked increase in the near-

trough, which is the recipient of any diffuse scattering. The lack of overlap in the error bars of the (52 ps) and the (60 ps) traces indicates statistical significance of at least 95% confidence for two standard errors. This is based on the analysis of ten shots heated, and ten shots unheated at each time step; the values shown above are the differences in the amplitude, unheated minus heated, abbreviated (E-B) on the chart.

Reflectivity Data

Samples of ultrathin platinum films, free-standing on gold 400M TEM grids, were subjected to 2 mJ/cm^2 fluence pump pulses, and then probed at increasing time delays in a reflectivity experiment[52] (see **Figure 5-5**). Similar results were obtained for the reduced fluence of 0.5 mJ/cm^2. The coherent oscillations are very clear for the first 25 ps; they are much too slow to be phonons. The longitudinal and transverse speed of sound in platinum at 20 °C of 3260 m/s and 1730 m/s[53]; an impulsive longitudinal wave launched by the arrival of the pump pulse has a round-trip time through the 10 nm film and back of 6 ps. None of these fit the temporal profile.

Similar results were obtained with silver nanoparticles embedded in a glass substrate.[54] These were explained in terms of the "breathing mode" vibrations of the nanoparticles as they exchanged energy with the surrounding matrix; they disappear then thermal equilibrium is achieved.

Generalizing this explanation to the somewhat loosely connected nanoparticles of an ultrathin film, we suggest that the network of roughly 10 nm sized platinum nanoparticles is exchanging energy via the connections of the network. **Figure 1-2** shows an ultrathin gold film; the platinum network is similar for the thinnest films.

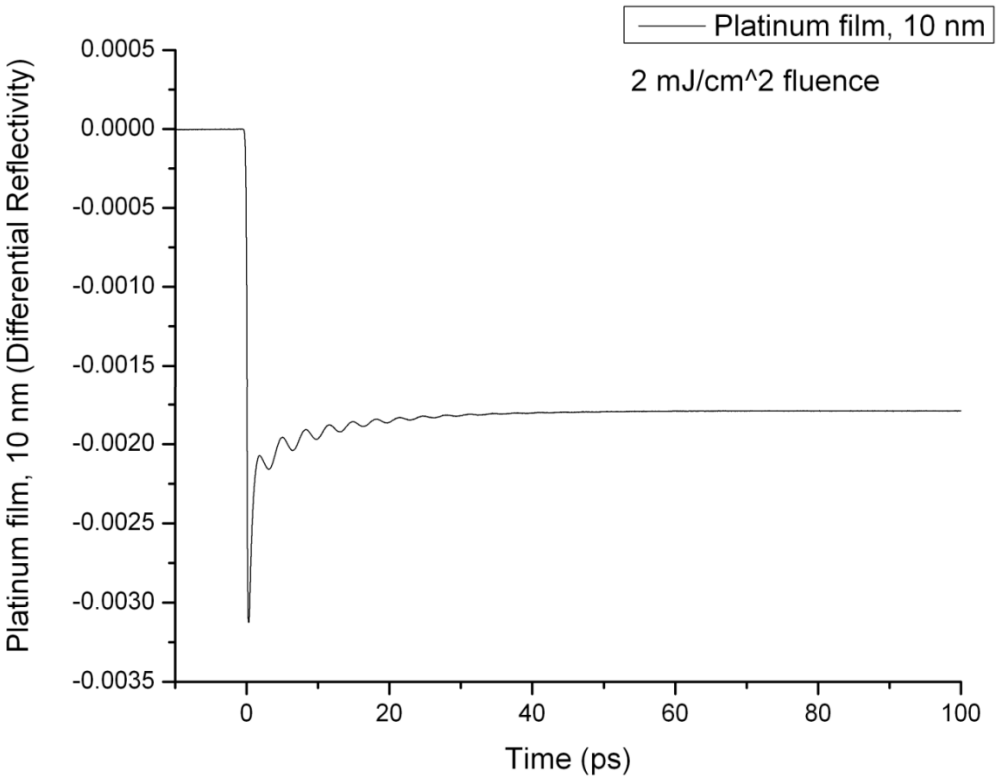

Figure 5-5 Reflectivity for 10 nm platinum film showing an impulsive decrease, followed by a series of 3 ps oscillations and a slow recovery.

Debye Relation for Acoustic Phonon Dispersion

Vibrations of a crystal lattice can occur in a very organized fashion; the simplest motions are thermal and acoustic. Thermal motion is random, but centered about the fixed points of the lattice. Acoustic motion has an organized wave structure with the displacements occurring in the same direction for successive atoms, as though they are connected by an elastic string. The lattice supports a longitudinal acoustic (LA) mode, and two transverse acoustic modes (TA). When the acoustic motion is considered at the microscopic level it

is clear that the minimum wavelength in direction $[hkl]$ is twice the interplanar separation; the nodes and antinodes each require something to displace.

When quantized these acoustic modes are called acoustic phonons. Debye developed a simple dispersion relation which is valid for acoustic phonons in the long-wavelength limit by considering a single speed of sound: $\omega(\mathbf{k}) = \mathrm{u}\bullet k$, where u is the speed of sound in the material, $\mathbf{k}$ is the k-space direction with $k = 2\pi/\lambda$, and $\omega(\mathbf{k})$ is the circular frequency in that direction, $\omega = 2\pi f$. In terms of reciprocal space $\mathbf{k} = 2\pi\mathbf{H}_{hkl}$ with $|\mathbf{H}_{hkl}| = 1/d_{hkl}$. For the minimum wavelength in each direction this yields $f(G_{hkl}) = u/2d_{hkl}$. For platinum at room temperature, 25 ˚C, the speed of sound is u=2680 m/s = 2.7 nm/ps.

Table 5-1 shows the minimum wavelength, frequency, and per cycle duration for the low index directions in platinum.

Platinum	**[111]**	**[200]**	**[220]**	**[311]**	**[331]**	**[420]**
Wavelength λ=2 d(hkl)	4.5313 Å	3.9242	2.7748	2.3664	1.8005	1.7550
Frequency, f =u/λ	5.914 THz	6.829	9.658	11.325	14.884	15.271
Per cycle duration, τ = 1/f	0.169 ps	0.146	0.104	0.088	0.067	0.065

Table 5-1 Debye acoustic phonon dispersion calculations for low-index platinum directions.

Analysis of Integrated Peak Position and Intensity

The raw data was analyzed as to the relative stability of the peak positions. By establishing a bracket about the nominal peaks corresponding to their FWHM, the centroid of the pixel position with respect to the corresponding intensity was calculated $PeakPosition = \sum\left(position_k \times intensity_k \right) / \sum intensity_k$; this serves as a proxy for the peak position. The integrated intensity over this interval serves as the peak intensity. This computational process smoothes fluctuations in the raw data and provides time-series values for position and intensity for each of the diffraction peaks.

Figure 5-6 shows the temporal evolution of the (111) and (311) peak positions as a relative percentage compared to the reference (unheated) data. The thermal expansion of platinum is β=8.8×10^{-6} / K , and the change in temperature is found from $\Delta R/R = \beta\Delta T$. The maximum change of the (311) peak position is 0.060% , so $\Delta\mathrm{T} = 0.00060/\beta = 68\mathrm{K}$, and occurs 10 ps after time-zero. The oscillations prior to time-zero are about $10\mathrm{K}$.

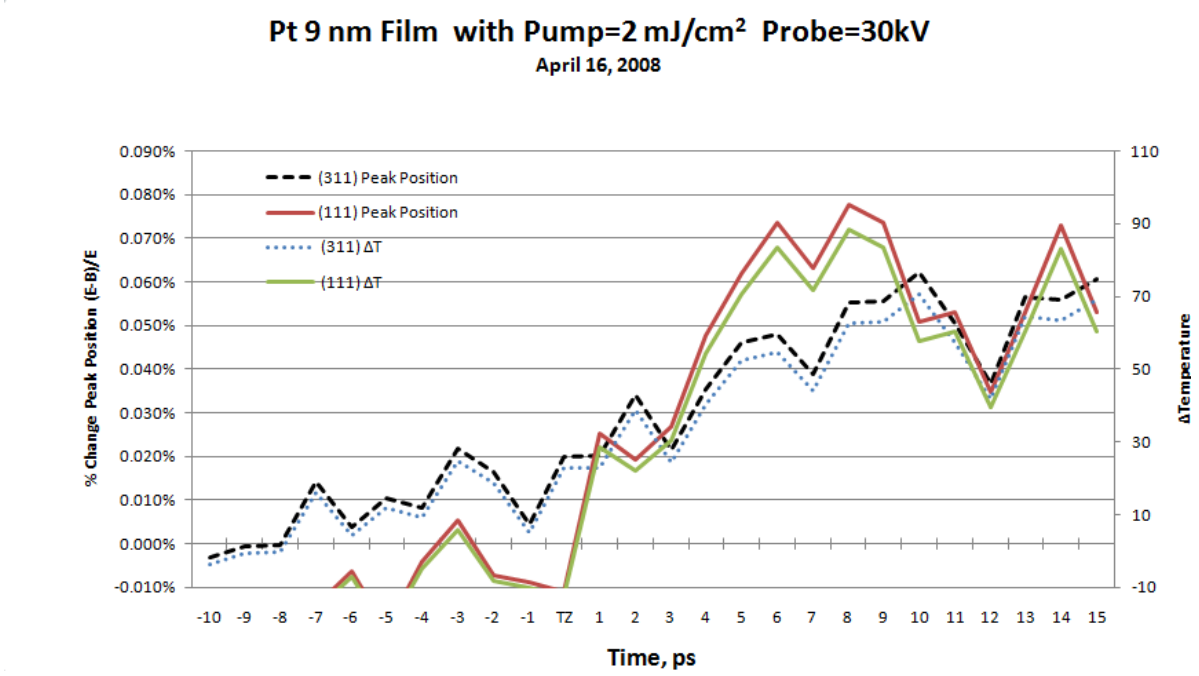

Figure 5-6 Peak (111) and (311) relative change of position with time, and corresponding change in temperature.

The (111) peak position achieves a maximum within 6 ps of time-zero, corresponding to an acoustic wave making a round trip through the film. The maximum change of the (111) peak position is 0.074%, so $\Delta T = 84K$, and occurs 10 ps after time-zero. This change is in addition to the thermal expansion; within an additional 6 ps the temperature profiles of the (111) peak and the (311) peak are the same. The observed strain along these directions is similar thereafter. Apparently the longer-wavelength [111] phonons thermalize more quickly, and also contain more energy as the maximum temperature is obtained in this direction.

The rate of change of strain for both the (111) and the (311) peaks shows steady growth beginning at time-zero. This implies that the heating process is impulsive, as a piano hammers the strings rather than displacive, which is how a harpist plucks them.

Experimental Results for Platinum	**[111]**	**[311]**
Thermal peak time, Δt	**6 ps**	**10 ps**
Peak temperature, ΔT	**84 K**	**68 K**
$\Delta t \cdot \tau = \Delta t / f$ (cf. **Table 5-1**)	**1.01**	**0.97**
Rate of Temperature change per cycle: $(\Delta T/ \Delta t) / \tau$	**83 K/ps/ps**	**86 K/ps/ps**

Table 5-2 Experimental results from 9 nm platinum film, showing temperature changes and time elapsed for maximum strain in the [111] and [311] directions. The rate of temperature change per phonon cycle time is the same for both.

The maximum thermal effects occur at different times for different crystal directions. For the data taken from **Figure 5-6** there is a curious relationship summarized in **Table 5-2**: the product of time to achieve maximum strain and phonon pulse duration are equivalent for the phonons shown. This observation lead to a search for a physical explanation. Since the rates of change of strain and temperature are nearly linear over these initial time intervals, the temporal rate of change of temperature was compared to the phonon frequency; the temperature is increasing at a constant rate per phonon cycle. That is, though the thermalization rate for the phonons differs by direction, the rate is the same when adjusted for the phonon temporal periods, $(\Delta T/ \Delta t) / \tau$, for this polycrystalline platinum film.

Figure 5-7 shows the evolution of the integrated peak intensity for the (311) peak; there is a $\pm 2\%$ oscillation prior to time-zero, rapidly increasing from 6% to 10% within 3 ps, and then decreasing over the next 7 ps; the (111) peak behaves similarly. These intensity changes would indicate very large Debye-Waller temperature increases; however, they are inconsistent with the peak position analysis. This is in large part due to poor background removal for this dataset, and exacerbated by fluctuating background noise to

which the peak positions are less sensitive. An additional factor is the impact of the acoustic wave traversing the thin film.

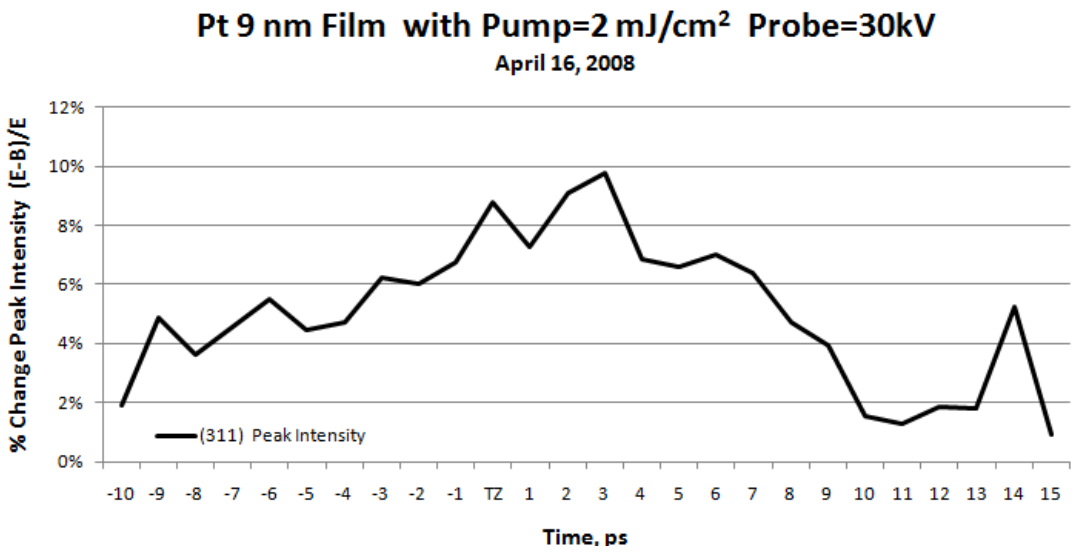

Figure 5-7 Peak (311) relative change of integrated intensity with time.

Chapter 6

Summary and Conclusions

Summary

An ultrafast photo-electron diffractometer has been built and described in detail. This device depends upon an ultrafast laser to deliver optical pulses to "pump" a sample, as well as to "probe" the structure by means of photo-electrons. An in-situ method for the determination of time-zero - the time when the optical pump and electron probe pulses are temporally coincident at the sample - has been developed and tested. The method reliably determines time-zero to within half a picosecond.

Experiments have been conducted in transmission mode with unsupported polycrystalline thin films (9 to 15 nm) of gold and platinum, as well as reflection mode experiments with bismuth (oxide) and highly ordered pyrolitic graphite (HOPG). These experiments show that it is possible to probe dynamically for structure changes caused by intense but non-destructive laser pulses at the sub-picosecond time scale.

Information which can be obtained includes the rate at which the optical energy of the pulse, which is captured primarily by the free electrons of metals, is transferred to acoustic phonons, transient strain and bond softening. This work also shows how phonon

energy transforms into thermal energy. Changes in surface reflectivity were measured which can be explained in terms of the nanostructure of the ultrathin films.

Proposed Future Experiments

The experiments conducted with free-standing ultrathin films, as described in Chapter 5, exhibited unexpected results which may be connected to the nanostructure of the materials. A series of further experiments are proposed which may elucidate these properties:

- Preparation of ultrathin platinum films made by different techniques, and fully characterized by SEM, TEM, and AFM
- Repetition of the ultrathin platinum experiments, conducted with different fluences for both ultrafast diffraction and reflectivity

Further experiments with various materials are proposed:

- Ultrafast diffraction experiments with few-layer graphene, to see if layers are ejected under impulsive pump pulses
- Ultrafast diffraction of $TiSe_2$ a layer type compound, to see how charge waves appear
- Ultrafast diffraction of GaAs to monitor the desorption of oxides and then As; this material is known to exhibit a stick-slip operation with microscopic, molten Ga droplets
- Ultrafast diffraction with magnetic thin films, such as Ni or Fe, looking for spin waves
- Ultrafast diffraction with CdTe, to study electron phonon scattering, and thermal transport

Proposed Improvements to the Diffractometer

Improvements in operation are to be found in three areas: (1) generation of a finer, more collimated electron beam, (2) delivery of a shorter, more temporally focused electron beam, (3) reduction of system background noise.

An improved electron beam requires a smaller source; in the current design the electron source is ~250 μm, which is due to the UV spot size. One approach is to expand the UV beam, and then sharply focus it onto the photocathode with a lens mounted within the framework of the electron gun. A provision for this has been made, though experiments have shown that as the UV is focused more finely it tends to cause the polycrystalline gold film of the photocathode to rupture. An alternative approach is to use a thermal field emission filament, heated somewhat below the emission threshold, and initiate an electron pulse by means of a laser pulse to the cathode tip. This would result in a precise release of electrons from a very small source spot, resulting in greater spatial coherence. For example, a cold field emission tip compatible with ultra high vacuum, and made of tungsten can have a cathode radius of under 100 nm, operate at room temperature, and have an energy spread at the cathode of 0.2 eV.

Better collimation is achieved by means of magnetic lenses, implemented by the fringing fields of a solenoid. These can be used to produce a slightly converging electron beam with the focus not at the sample but at the detector plane. This provides better separation of the diffraction pattern. The difficulty in the current system is that good electron optics takes space, and the additional drift distance increases the temporal length of the electron pulse. The response has been to lower the number of electrons per pulse, which increases the duration of an experiment proportionally, or to eliminate the focusing optics, which results in a diverging beam due to radial Coulomb repulsion. This lowers the quality of the recorded diffraction pattern. Making room for good electron optics can be achieved if temporal compression is performed immediately before hitting the sample to be probed.

If given sufficient time, an electron pulse will self-chirp; the self-repulsion of the electrons in the pulse will cause it to spread out evenly, somewhat like a set of springs in equilibrium. The velocity (and energy) distribution is then linear, in proportion to its position in the pulse. A chirped pulse can be compressed by a variety of means including

a magnetic chicane or an electrostatic compressor which retard the speeds of the faster electrons while the laggards catch up. The most elegant approach is to reverse-chirp[40] the electron pulse during its creation, and allow it to compress itself as it approaches the sample. In this case the slowest, lowest energy electrons are generated at the head of the electron pulse, and as the increasingly faster electrons of the pulse follow them, the mutual repulsion acts as a traffic jam, and deliver the maximally compressed pulse at the sample. In order to achieve this, the design of the system would have to optimize the distance and the accelerating voltage (together these determine the travel time), and the degree of reverse chirping possible.

Limiting the operation of the detector to the time when the electron pulses should be arriving improves the signal-to-noise ratio by removing stray ions generated in the continuous high voltage fields of the electron gun and the ion pump. It also removes any ions generated from the pump laser interaction with the sample. "Fast gating" the detector is achievable at the 10 ns or better time scale, coordinated with the pump laser pulse by an optical switch. The current system is ungated; all background events are recorded, along with the data.

With the increased distance available, and the requirement for improved electron optics, a system based upon a TEM column appears feasible and desirable. This implies the availability of ultrafast electron imaging as well as diffraction. Such instruments have previously been built, including the DTEM at LLNL[55] with temporal resolution of 15 ns.

Experiments that commend themselves include the determination of electron-phonon coupling parameters in metallic films, but also the properties of graphene. Graphene is a two-dimensional crystal, consisting of a single (or very few) planes of graphite, and has only recently begun to be characterized[56]. Clearly there are many things to be learned from a time-resolved studies of graphene.

Appendices

Appendix A

Sample Preparation and Evaluation

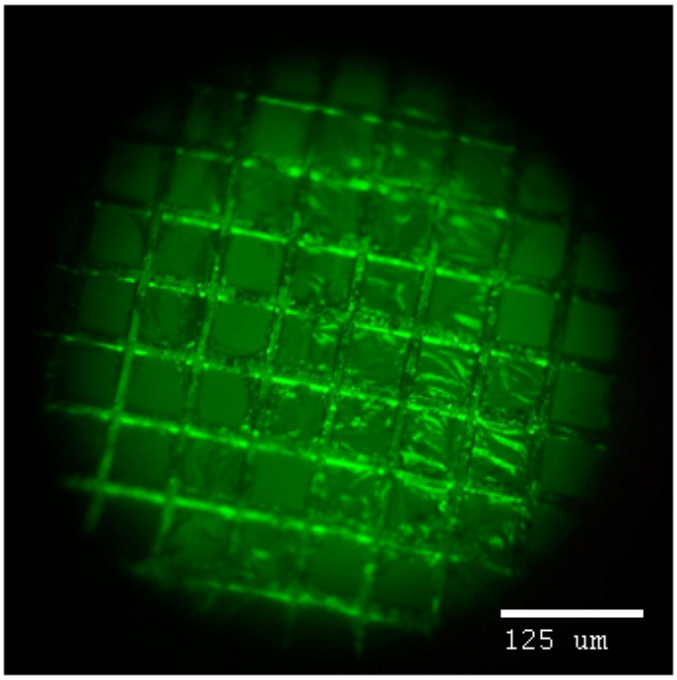

Figure A-1 Polycrystalline gold film, 15 nm thick, mounted on 400M TEM grid; false color.

Considerations for Samples

Electron diffraction in transmission requires very thin samples, and as the accelerating voltage is decreased they must become thinner still. At 20 kV gold and platinum must be under 15 nm thick for good images, and slightly thicker at 30 kV. Increasing the electron

beam intensity will allow use of somewhat thicker samples, but this increases the pulse duration and so is not useful for an ultrafast Diffractometer. Working samples in polycrystalline platinum were from 9 to 12 nm thick.

At least one sample from each film should be examined with a TEM in order to characterize nanoparticle size (see **Figure A-2** and **Figure A-3**) and the expected diffraction pattern. The nanoparticles from the sputtered gold films appear to be polycrystalline under selected area diffraction. General film quality can be determined with an optical microscope for the remaining samples. Note that for gold films this thin will appear blue due to their optical transparency; the golden color dominates as they approach 20 nm.

Making Samples

Preparation of polycrystalline samples is conveniently performed by sputtering onto a rock salt flat at room temperature. The rock salt flats must be free of dust prior to coating; this can be accomplished with a can of "dry air" and a brief rub with a Kim Wipe or similar tissue, or a clean piece of flannel. The sputtered film can be saved for an extended period in a dry box. It is floated off in a mixture of 20% methanol with 80% deionized water. The methanol is used to reduce the surface tension of the water which otherwise tends to break up the film during the floating off process. It also seems to reduce breakage during the drying process. The floating-off process is best performed by deliberately sliding the rock salt into the water, film side up, and allowing the surface tension to dislodge the film. It only takes a second or so, and the substrate can be withdrawn from the water. If the rock salt is allowed to dissolve in the water tiny crystalline grains of rock salt will contaminate the sample; these will generate additional diffraction spots and/or rings. These can be clearly seen with a TEM examination, **Figure A-2**. For this reason the water-methanol mix should be discarded after each float-off.

Earlier samples were usually deposited on amorphous carbon which had been deposited on freshly cleaved mica slips; see **Figure A-4**. This process was abandoned due to failures of the support film when subjected to the pump laser pulses, and the presence of amorphous diffraction rings coinciding with the gold diffraction rings at 20 kV.

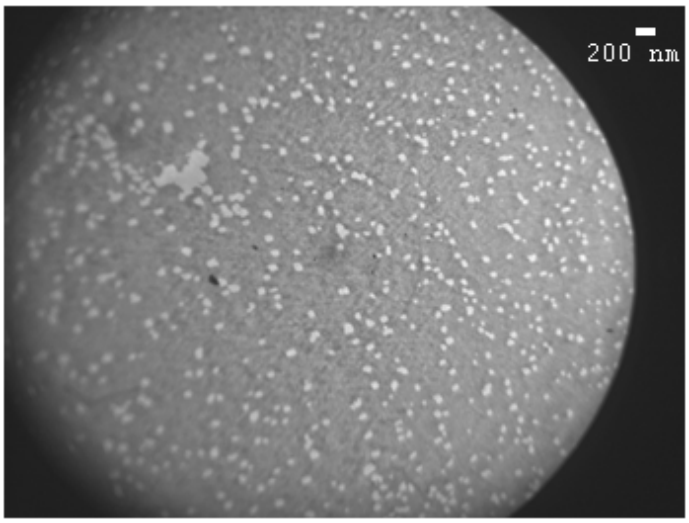

Figure A-2 TEM image of polycrystalline gold thin film contaminated by dissolved rock salt from the substrate; M=30,000.

Once the films are floated off they can be "scooped up" onto a TEM grid or TEM aperture with the aid of a set of anticapillary tweezers with sharp tips; this type of tweezers helps to drain the water from the sample. The drop that remains can be removed quickly by touching it to the edge of any absorbent paper or tissue.

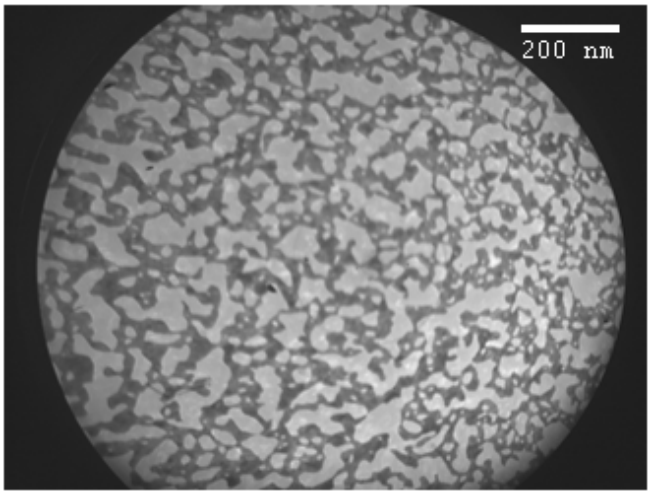

Figure A-3 TEM image of polycrystalline gold film, 10 nm thick, showing nanoparticle structure; M=82,000. The low-contrast areas are voids.

There are a great variety of TEM grids and apertures available, with the least expensive being made of copper. Unfortunately these copper grids have an unspecified coating applied to prevent oxidation tarnish, but when the pump laser beam strikes them it creates an ionized debris trail which contributes overwhelming noise to the MCP detector. When this was clearly understood all sample and target TEM grids and apertures were replaced by more expensive gold versions. This conversion made a dramatic improvement in signal-to-noise ratio.

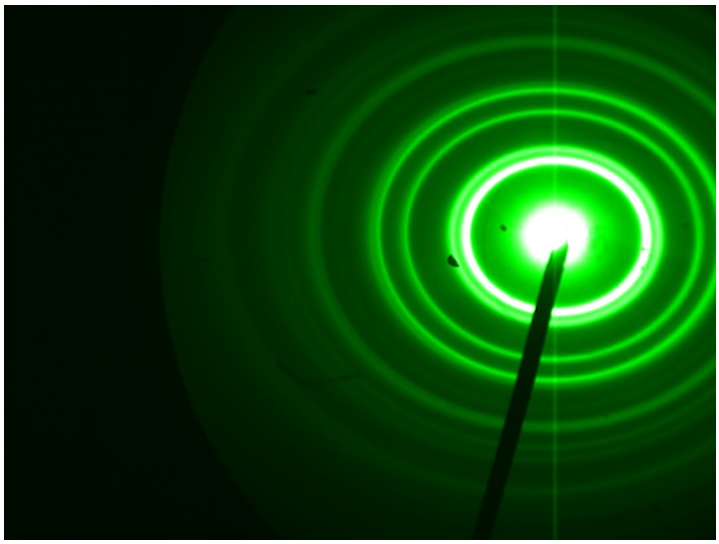

Figure A-4 TEM diffraction pattern for polycrystalline gold thin film, 10 nm. Substrate is amorphous carbon which is responsible for some weak amorphous rings.

Free Standing Thin Films

Free standing thin films as thin as 10 nm can be successfully transferred to TEM grids of 400M or less, and even to TEM apertures of up to 600 μm diameter with no other support; see **Figure A-5**. These are difficult to make because the film ruptures as it dries, but when successful they work well in the TEM, and also in the diffractometer. However, they tend to rapidly deteriorate when laser heating is applied, even at low fluences; this may be due to induced vibrations. Thus most of the work carried out has been on 400M TEM grids.

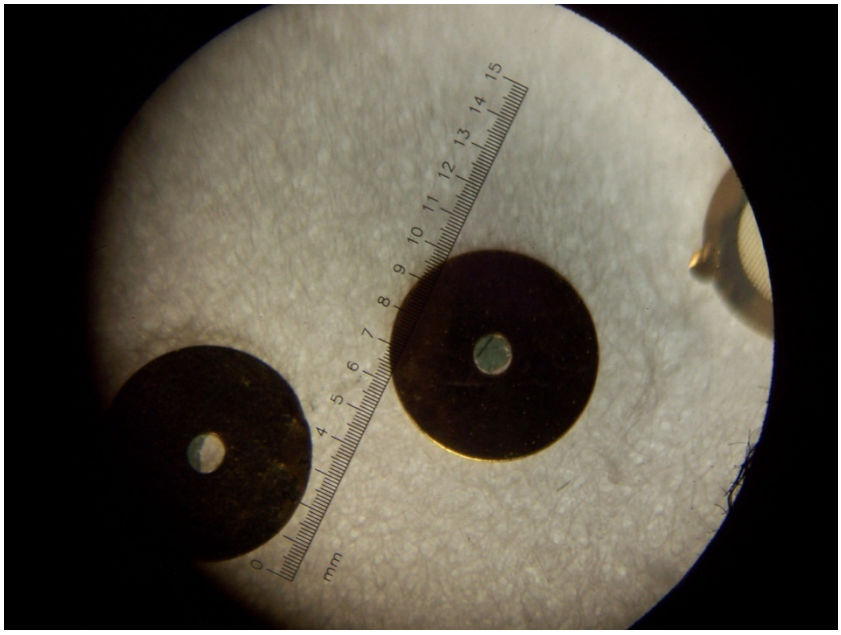

Figure A-5 Polycrystalline gold thin films, 10 nm thick, free standing on 600 um aperture.

Appendix B

Program Code

Program Code for Ring_Profile_Peak Finder

```
import ij.*;
import ij.plugin.filter.PlugInFilter;
import ij.plugin.*;
import ij.process.ImageProcessor;
import ij.process.*;
import ij.gui.*;
import java.awt.*;
import java.io.*;
import ij.io.*;
import java.util.*;
import ij.text.*;


/* Portions based upon Radial_Profile.java, by  Paul Baggethun, 2002/05/01 */
/* Adapted and extended by Peter Diehr, University of Michigan, 2002/09/23 */
/* Major rewrite by Peter Diehr, University of Michigan, 2008/11/22 - removed unused
code, added auto-find of best fit rings */
/* ******************************
Description: This ImageJ plugin produces a profile plot of normalized integrated
intensities around concentric circles as a function of distance from a point in the image.
The position of this point, or the radius of integration, can be modified in a dialog box.
The intensity at any given distance from the point represents the sum of the pixel values
around a circle.
This circle has the point as its center and the distance from the point as radius. The
integrated intensity
is divided by the number of pixels in the circle that is also part of the image, yielding
normalized comparablevalues. The profile x-axis can be plotted as pixel values or as
values according to the spatial calibration of input image.
```

```
Radial profiles are useful for measurement of x-ray powder diffraction patterns as well as
electron diffraction patterns.
****************************** */

public class Ring_Profile_Peak implements PlugInFilter
{
/*debug*/ // TextWindow tw = new TextWindow("Distances", "", 700, 200);
        ImagePlus imp;
        boolean canceled=false;
        static boolean done=false;
        int  X, Y;
        static int nC = 3;                                                          // #
of contrast pairs
        static double X0;
        static double Y0;
        static double mR, mRI;
        static double mLimitLo, mLimitHi;
        static double mC1a;
        static double mC2a;
        static double mC1b;
        static double mC2b;
        static double mC1c;
        static double mC2c;

        static double mScan;
        static boolean doNormalize = true;
        static boolean doReportAll = false;
        static boolean doMaxContrast = false;

        int nBins=100;
        double max, max_r, maxPeak, maxPeakValue;
        double maxC, maxCPeakValue;
        double maxX0, maxY0;
        double mX0, mY0;
        double [] cMax = new double [4];
        double [] cMin = new double [4];
```

```
double [] cContrast = new double [4];
double [] mContrast = new double [4];
double [] mC1 = new double [4];
double [] mC2 = new double [4];

public int setup(String arg, ImagePlus imp)
{
    this.imp = imp;
    return DOES_ALL+NO_UNDO;
}

public void run(ImageProcessor ip)
 {
    // could not make static arrays work!
    mC1[1] = mC1a;
    mC2[1] = mC2a;
    mC1[2] = mC1b;
    mC2[2] = mC2b;
    mC1[3] = mC1c;
    mC2[3] = mC2c;

    // Get circle ROI from stored points  (center and radius)
    if(!done) GetCircleROI();

    IJ.makeOval((int)(X0-mR), (int)(Y0-mR), (int)(2*mR), (int)(2*mR));
    doDialog();

    // pass array information back to static holders
    mC1a = mC1[1];
    mC2a = mC2[1];
    mC1b = mC1[2];
    mC2b = mC2[2];
    mC1c = mC1[3];
    mC2c = mC2[3];

    // Redraw, with altered radius
    IJ.makeOval((int)(X0-mR), (int)(Y0-mR), (int)(2*mR), (int)(2*mR));
```

```
        if (canceled) return;

        doRadialDistribution(ip);
    }

    // Read Circle coordinates and radius for the circular ROI
    public void GetCircleROI()
     {
        // Only do this the first time ... remember what was read in
        done=true;

        TextReader tr = new TextReader();
        ImageProcessor ip = tr.open(".//RingProfilePeak.txt");
        if (ip==null)  return;
        int width = ip.getWidth();
        int height = ip.getHeight();

        if (width <13 || height!=1)
         {
            IJ.showMessage("Ring_Profile_Peak", "Need Center (X,Y), Scan distance,
Radius(Inner, Outer),  Level (Lo/Hi), 3 x Contrast(Begin/End) - all on one line to make the
circle: found ["+width +" "+ height+"]");
            return;
        }
        X0 =   ip.getPixelValue(0, 0);
        Y0 =   ip.getPixelValue(1, 0);
        mScan = ip.getPixelValue(2, 0);
        mRI = ip.getPixelValue(3, 0);
        mR = ip.getPixelValue(4, 0);
        mLimitLo=ip.getPixelValue(5, 0);
        mLimitHi=ip.getPixelValue(6, 0);
        mC1[1] = ip.getPixelValue(7, 0);
        mC2[1] = ip.getPixelValue(8, 0);
        mC1[2] = ip.getPixelValue(9, 0);
        mC2[2] = ip.getPixelValue(10, 0);
        mC1[3] = ip.getPixelValue(11, 0);
        mC2[3] = ip.getPixelValue(12, 0);
```

```
        }

        private void doDialog()
        {
            canceled=false;
            GenericDialog gd = new GenericDialog("Radial Distribution...",
IJ.getInstance());
            gd.addNumericField("X center (pixels):",X0,1);
            gd.addNumericField("Y center (pixels):", Y0,1);
            gd.addNumericField("Distance to Scan:",mScan,0);
            gd.addNumericField("Inner Radius (pixels):", mRI,0);
            gd.addNumericField("Outer Radius (pixels):", mR,0);
            gd.addNumericField("Minimum Level :", mLimitLo,0);
            gd.addNumericField("Maximum Level :", mLimitHi,0);
            gd.addNumericField("Begin Contrast 1 (pixel):", mC1[1],0);
            gd.addNumericField("End Contrast 1 (pixel):", mC2[1],0);
            gd.addNumericField("Begin Contrast 2 (pixel):", mC1[2],0);
            gd.addNumericField("End Contrast 2 (pixel):", mC2[2],0);
            gd.addNumericField("Begin Contrast 3 (pixel):", mC1[3],0);
            gd.addNumericField("End Contrast 3 (pixel):", mC2[3],0);
            gd.addCheckbox("Normalize?", doNormalize);
            gd.addCheckbox("Report All?", doReportAll);
            gd.addCheckbox("Optimize Contrast?", doMaxContrast);
            gd.showDialog();
            if (gd.wasCanceled())
            {
                canceled = true;
                return;
            }
            X0=gd.getNextNumber();
            Y0=gd.getNextNumber();
            mScan=gd.getNextNumber();
            mRI=gd.getNextNumber();
            mR=gd.getNextNumber();
            mLimitLo=gd.getNextNumber();
            mLimitHi=gd.getNextNumber();
            mC1[1]=gd.getNextNumber();
```

```
    mC2[1]=gd.getNextNumber();
    mC1[2]=gd.getNextNumber();
    mC2[2]=gd.getNextNumber();
    mC1[3]=gd.getNextNumber();
    mC2[3]=gd.getNextNumber();
    doNormalize = gd.getNextBoolean();
    doReportAll = gd.getNextBoolean();
    doMaxContrast = gd.getNextBoolean();

    if(gd.invalidNumber())
     {
        IJ.showMessage("Error", "Invalid input Number");
        canceled=true;
        return;
    }
}

// doRadialDistribution
private void doRadialDistribution(ImageProcessor ip)
{
    nBins = (int) (3*mR/4);
    int nSkipBins = (int)( (3*mR/4)*mRI/mR);
    int thisBin;
    int k;
    double[][] mAccumulator = new double[2][nBins];
    double[][]   Accumulator = new double[2][nBins];

    // Fetch data from the image only once

    int[][] intPixels = (int [][])ip.getIntArray();

    int nRows = ip.getHeight();
    int nCols = ip.getWidth();

    double R;
    double D;
    double xmin,xmax,ymin,ymax;
```

```
                double mPixel;

                // Initialize the "Peak" values ... we will scan the center (X0,Y0) thru a box
2*mScan on a side
                maxX0 = X0;
                maxY0 = Y0;
                maxPeak = 0.0;
                maxPeakValue = 0.0;
                maxCPeakValue = 0.0;
                double dSteps = (2*mScan)*(2*mScan);
                double dStep = 0;
                // Scan the region centered on (X0,Y0) as boxed by mScan
                for (mX0 = X0 - mScan; mX0 <= X0 + mScan; mX0++)
                {
                   for (mY0 = Y0 - mScan; mY0 <= Y0 + mScan; mY0++)
                   {
                    dStep++;
                    IJ.showProgress(dStep/dSteps);
                    for (k=0; k<nBins;k++)                                                    //
clear the accumulators
                    {
                         Accumulator[0][k] = 0;
                         Accumulator[1][k] = 0;
                    }
                    // Set the bounds for checking
                    xmin=mX0-mR;
                    xmax=mX0+mR;
                    ymin=mY0-mR;
                    ymax=mY0+mR;

                    if( xmin < 0) xmin = 0;
                    if( xmax > nCols - 1) xmax = nCols - 1;
                    if( ymin < 0) ymin = 0;
                    if( ymax > nRows - 1) ymax = nRows - 1;

/* debug */  //       tw.append("Scanning ("+ mX0+","+mY0+")="+maxPeakValue+"
xmin="+xmin+" xmax="+xmax+" ymin="+ymin+" ymax="+ymax+" mR="+mR);
```

```
                    // Integrate the rings based on the trial center (mX0,mY0)
                    for (double i=xmin; i<xmax; i++)
                    {
                        for (double j=ymin; j<ymax; j++)
                        {
                            if( i < 0 || i > nCols - 1 || j < 0 || j > nRows - 1)
                              D = 0.0;
                            else
                              D=(double)intPixels[(int)i][(int)j];

                            if( (mLimitLo <=D) & (D <= mLimitHi) )
                            {
                              R = Math.sqrt((i-mX0)*(i-mX0)+(j-mY0)*(j-mY0));
                              thisBin = (int) Math.floor((R/mR)*(double)nBins);
                              if (thisBin==0) thisBin=1;
                              thisBin=thisBin-1;
                              if (thisBin>nBins-1) thisBin=nBins-1;
                              Accumulator[0][thisBin]++;       // [0]=Good pixels for this ring
                              Accumulator[1][thisBin]+=D;     // [1]=Integrated counts for this ring
                            }
                        }
                    }
                    max = maxPeakValue;
                    max_r =maxPeak;
                    maxC = maxCPeakValue;

                    for (int kk=1; kk<= nC; kk++)
                    {
                        cMax[kk] = ip.getMin();
                        cMin[kk] = ip.getMax();
                    }
/* debug */     //   tw.append("LocalPeak ("+ mX0+","+mY0+")="+ IJ.d2s( max,1) + " @ "+
IJ.d2s( max_r,1) + " PrevMax="+ IJ.d2s( max,1));

                    int intNewPeak = 0;
                    // Find the peak, and the peak value for (mX0,mY0)
```

```
                for (k=0; k<nBins;k++)
                {
                    mPixel = mR*((double)(k+1)/nBins);
                    if (k < nSkipBins)
                         Accumulator[1][k] = 0;
                    else
                        Accumulator[1][k] =  Accumulator[1][k] / Accumulator[0][k];
            // Average counts around the ring
                    Accumulator[0][k] = mPixel;
                        // Record ring ID
                    if ( max < Accumulator[1][k] )
                    {
                        max = Accumulator[1][k];
                    // Value for this ring
                        max_r = Accumulator[0][k];
                    // Note the ring ID
/* debug */     //          tw.append("LocalPeak ("+ mX0+","+mY0+")="+ IJ.d2s( max,1) + "
@ "+ IJ.d2s( max_r,1));
                        intNewPeak++;
                    }
                    // Find peaks and valleys for ring contrast calculations
                    for( int kk = 1; kk<= nC; kk++)
                    {
                        if( mC1[kk] <= mPixel && mPixel <= mC2[kk]  )
                        {
                          if(cMax[kk] < Accumulator[1][k]) cMax[kk]  = Accumulator[1][k];
                          if(cMin[kk]  > Accumulator[1][k]) cMin[kk]  = Accumulator[1][k];
                        }
                    }
                }
                Accumulator[1][nBins-1] = Accumulator[1][nBins-2];
            // Fix anomaly on last bin

                // Calculate total contrast for this center
                maxC = 0.0;
                for( int kk = 1; kk<= nC; kk++)
                {
```

```
                    cContrast[kk] = 100.0 *  (cMax[kk]-cMin[kk])/(cMax[kk]+cMin[kk]);
                    maxC += cContrast[kk];
                }
                maxC /= nC;
                if( maxCPeakValue < maxC )
                {
                    if( doMaxContrast ) intNewPeak = -1;
                    maxCPeakValue = maxC;
                }

                if( maxPeakValue < max )
                {
                    if( !doMaxContrast ) intNewPeak = -1;
/* debug */  //          IJ.showMessage("MaxPeak ("+ mX0+","+mY0+")="+ IJ.d2s(
maxPeakValue,1));
                }
                if( intNewPeak < 0 )
                {
                    maxX0 = mX0;
                    maxY0 = mY0;
                    maxPeakValue = max;
                    maxPeak = max_r;
                // Ring ID of the peak value
                    for (k=0; k<nBins;k++)
                // Copy the entire distribution for later
                    {
                         mAccumulator[0][k] = Accumulator[0][k];
                         mAccumulator[1][k] = Accumulator[1][k];
                    }
                    for (int kk=1; kk<= nC; kk++)
                    {
                        mContrast[kk]= cContrast[kk];
                    }

                }
                if( doReportAll && intNewPeak < 0) doPlot(ip, mAccumulator); // Plot all
new peaks
```

```
        }     // inner scan
    }    // outer scan

    // Update parameters for next run ...
    X0 = maxX0;
    Y0 = maxY0;
    if( !doReportAll) doPlot(ip, mAccumulator);
        // Omit plot if already done
}

// doPlot ...  generate plot of diffraction results
private void doPlot(ImageProcessor ip, double[][] mAccumulator)
{
    String sMsg;
    String sContrast = " [";
    PlotWindow pw;
    double[][]   plotAccumulator = new double[2][nBins];

    for (int k=0; k<nBins;k++)
        // Copy the entire distribution for later
    {
         plotAccumulator[0][k] = mAccumulator[0][k];
         plotAccumulator[1][k] = mAccumulator[1][k];
    }

    // Report peak contrast for this center
    for( int kk = 1; kk<= nC; kk++)
    {
        sContrast += IJ.d2s(mContrast[kk],1)+ " ";
    }

    sMsg = imp.getTitle();
    if (sMsg.startsWith("Result of ") )
        sMsg = sMsg.substring(10);
    if(sMsg.endsWith(".fit"))
        sMsg = sMsg.substring(1,sMsg.length()-4);
```

```
            sMsg =sMsg +  ": Peak@" + IJ.d2s( maxPeak,1)  + " = " + IJ.d2s(
maxPeakValue,1)  + sContrast + "%] C=(" + maxX0 + ", " + maxY0 + ")  Limits=" +
(int)mLimitLo + "/" + (int)mLimitHi+ " Scan="+(int)mScan;


            if (doNormalize )
            {
                for (int i=0; i<nBins;i++)
                 {
                    plotAccumulator[1][i] /= 0.01*maxPeakValue;
                }
                pw = new PlotWindow(sMsg, "Radius [pixels]", "Normalized Intensity",
plotAccumulator[0], plotAccumulator[1]);
            }
            else
            {
                pw = new PlotWindow(sMsg, "Radius [pixels]", "Intensity",
plotAccumulator[0], plotAccumulator[1]);
            }
            pw.draw();
        }
}
```

Appendix C

Experimental Procedures

Running an Ultrafast Photo-Electron Diffractometer

Since changing samples requires that the vacuum chamber be opened, a full vacuum chamber bake out at 375 °F is required to drive out the water vapor, followed by a cool down to room temperature is required. Final vacuum should be with the ion pump alone, and should be better than $5x10^{-9}$ Torr. This takes about two days, and should be followed by an experimental determination of time-zero. The samples are previously prepared and installed as described in ***Sample Preparation and Evaluation***. Beam alignment is carried out as previously described in ***Determination of Time-Zero***.

The actual sample should have been previously evaluated optically and with a TEM. The diffraction quality of the installed sample should be verified again when it is in the diffractometer. This allows a determination of the camera integration time, and the corresponding MCP amplification level. The sample should also be tested at the intended laser fluence to ensure that it is robust enough to test.

When everything is ready, the automated experimental software can be initiated, and the process runs by itself. Since things can go wrong, it needs to be monitored.

Determination of Electron Beam FWHM

The electron beam intensity distribution is essentially Gaussian when it reaches the MCP detector as long as it is not too bright. This is easily determined by recording an image and taking a line profile. As previously noted, pulses containing fewer electrons have shorter pulse durations, so for most experiments weak beams are preferred, and thus longer integration times. It is necessary to know the electron beam diameter so that the laser heating beam is wide enough to ensure even heating across the portion of the sample illuminated by the electron beam.

Beam divergence can be partially controlled by magnetic focusing, but the current system eliminated the focusing coils in favor of a very short drift region; thus the beam diameter as recorded by the MCP detector is irrelevant; the diameter at the sample plane is needed.

Two methods are available for measuring the electron beam at the sample plane. The first is the use of a "knife edge", the flat part at the bottom of the sample holder. A series of beam images are recorded, the first with the beam fully in view, and the final with the beam fully occluded, in 50 μm vertical translation steps. This spatial series is then transformed into a series of intensities by integrating the intensity counts of each image. The resulting curve is analyzed to find the 90-10 cutoff values for total intensity; the interpolated distance between these limits is 1.07 times the $1/e^2$ beam diameter, multiply by 0.59 to get the FWHM beam diameter. This gives consistent results with the direct method, see **Figure C-1**. The direct method is to image the electron beam passing through a clean 400M grid at the sample plane. The direct method works best with a single microchannel plate; when two are used in chevron fashion the details are blurred. Due to the very short drift distance beyond the anode pinhole exit the value obtained is approximately that of the pinhole diameter.

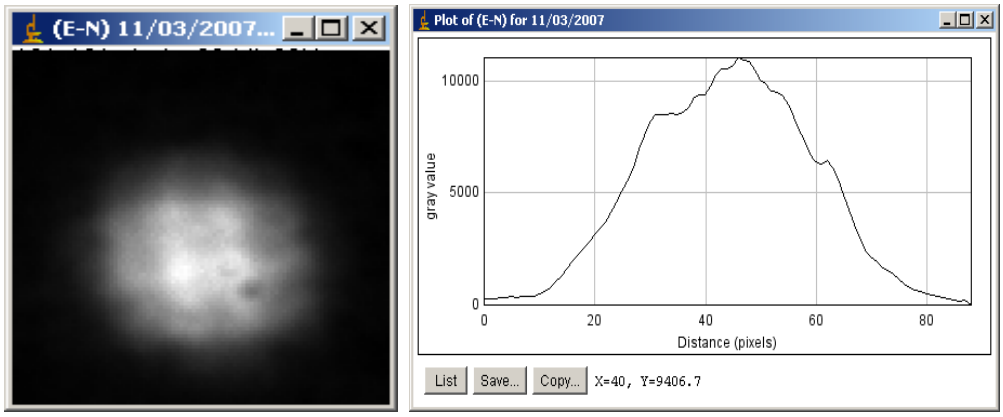

Figure C-1 Electron beam calibrated by 400M grid at sample plane as captured by single plate MCP; FWHM is ~200 um. The corresponding line profile shows the TEM grid bars.

Calibrating Pump Pulse Intensity

The pump beam must provide uniform heating of that portion of the sample which is covered by the electron beam; clearly it needs to have a larger FWHM. The experiments described herein are nondestructive, and require a great number of repetitions to accumulate sufficient statistics to improve the signal-to-noise ratios to acceptable limits. A single experimental run takes ten to twenty hours, and may be repeated with the same sample a number of times. This results in millions of pump laser shots per hour. There is no accumulated damage to the thin films used when the fluence used is less than 5 mJ/cm^2.

The exact fluence and intensity can be measured prior to each experimental run by means of the following procedure, see **Figure C-2**:

- Pump beam power level is set by means of a neural density filter wheel
- Pump beam is focused onto sample plane by 1.0 m lens
- Pump beam passes thru 400M Au TEM grid, and is optically diffracted
- Diffracted beam is collected by 4F system, imaging grid onto CCD
- Resulting images use 400M grid to calibrate beam size

- Retracting the TEM grid provides a pump beam image without the grid.
- Line plot is used to calculate FWHM of pump beam at sample plane
- Intensity is power/rep rate/pulse duration/spot size ~ 10^10 W/cm^2
- Fluence is power/rep rate/spot size ~ 5 mJ/cm^2 results in no damage

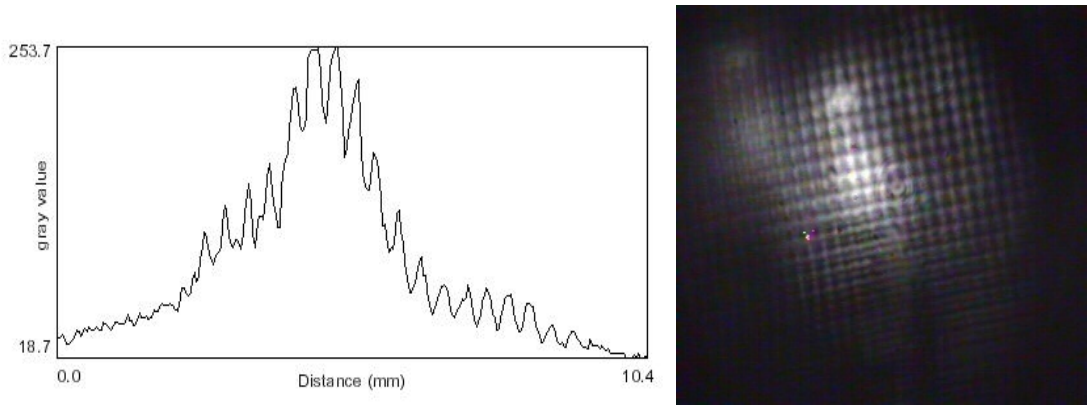

Figure C-2 Calibration of the pump pulse intensity depends on recording an image of the sample plane illuminated by the pump beam. A 400M TEM grid provides a scale, 63.5 um bar-to-bar.

A spreadsheet is used to carry out the calculations; the fluence is based upon the $1/e^2$ diameter of the pump beam.

Automated Experimental Software

The automated experimental software is written in LabVIEW, a National Instruments product. The actual software was written by Paul Van Rompay when he was working as a post doctoral fellow in our research group. The basic design is to record a series of CCD images of the diffraction patterns amplified by the MCP detector. The software allows the camera integration time to be set, and controls the external shutter which alternately blocks and unblocks the pump laser beam. Any number of images can be recorded for a single delay line position; when the correct number has been taken the

delay stage is advanced the specified number of steps. The steps have been calibrated to the time delay, and convenient step sizes are 400 fs (10 steps) and 1 ps (25 steps). In addition, the automated experimental software can check maximum and minimum intensity levels on each image, and if out of range will save the image with an error tag, and automatically take a replacement. This has been valuable when the electron gun has a discharge, or when somebody turns on the room lights by mistake.

Prior to starting the run a set of background images are taken. Some have the electron beam blocked; of these the most important are the ones labeled "N" for *no beams active*, and the one labeled "L" for *laser-beam only* active. These will be directly subtracted from the actual images during later processing.

As the run progresses each image is written out as a separate image file with timestamp and specific run information coded in the file names. The shots with the pump beam blocked are labeled "E" for *electron beam only*, while the unblocked shots are labeled "B" for *both beams active*. Thus each heated diffraction pattern is accompanied by a baseline comparison shot which was not heated, but which has the same history.

Post-Experimental Processing of Diffraction Image Data

The image files are processed by a series of Java plugins written by Peter Diehr, and integrated with ImageJ[57], an image processing an analysis program. One of the main programs is used to determine the center of the diffraction pattern based upon contrast between consecutive rings. Another uses the specified center and specified, and a mask which is hand-crafted for each data run, and which masks out all features which are not part of the diffraction pattern, such as the rotatable beam blocker, the edges of the MCP, as well as camera and MCP defects. This program subtracts the "N" background from each of the "E" shots, applies the image mask, and then performs a circular integration on

the remaining information in order to produce a line profile of the polycrystalline diffraction pattern. A similar procedure is carried out on the "B" shots, from which the "L" background is subtracted.

The result is a time-series of background-corrected diffraction amplitudes, similar to the 2θ plots generated by an x-ray diffractometer, but instead indexed by camera pixel. The unheated set consists of the "E-N" images, while the heated set consists of the "B-L" images. The portion of the time-series prior to time-zero should be essentially the same, except for a bit of pump-laser induced scattering noise, while the following time series permits an analysis of changes of the peak amplitudes, peak positions, peak broadening, and changes to the diffuse inter-peak scattering.

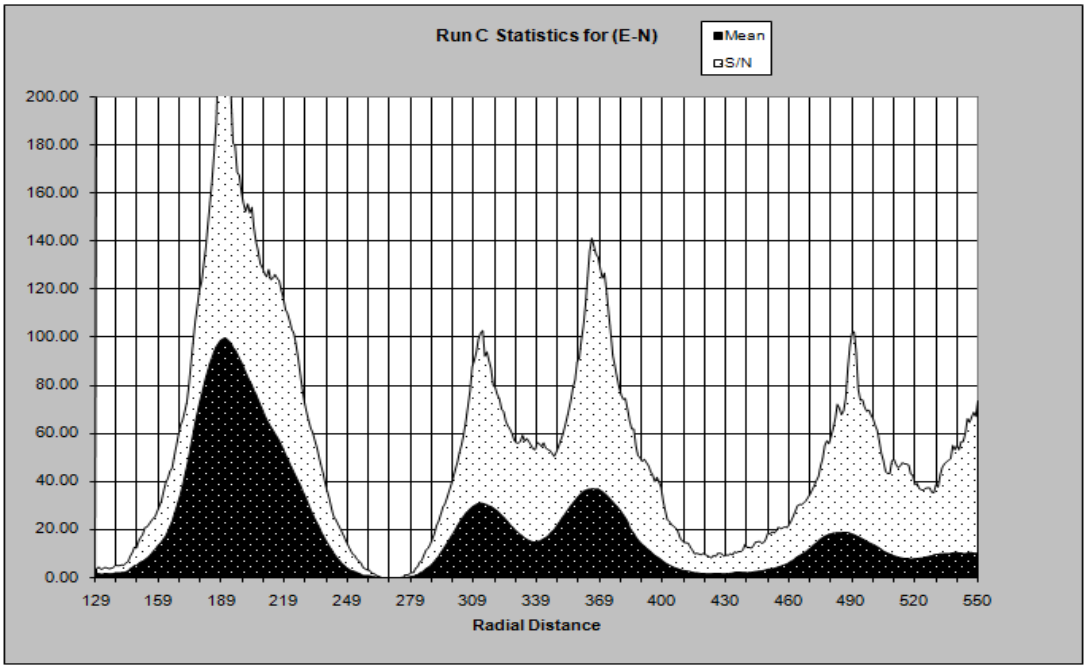

Figure C-3 Signal-to-Noise ratio aligned with mean integrated diffraction amplitudes for 9 nm platinum film; data from April 16, 2008. S/N is better than 100:1 for most peaks.

Signal-To-Noise

When a series of measurements are taken of the same or similar items, the mean value is best estimate of the value, and the standard deviation describes can be used as an estimator of the noise. The signal-to-noise ration, S/N, is the mean divided by the standard deviation. Because the Debye-Waller effect is only a few percent for integrated intensity, a S/N ratio of over 100 is required. See **Figure C-3** for recent results.

Equipment Manifest and Notes

Laser: Clark-MXR CPA 2001. 780 nm Ti:Sapphire output at 1000 Hz rep rate, 800 μJ per pulse, or about 0.8 Watts into a power meter; beam is ~ 5 mm diameter, and well collimated, with < 1% RMS noise in the pulse-to-pulse energy. Pulse duration is ~150 fs, and when well maintained rarely drops even a single pulse.

Laser Shutter: Uniblitz, 50 ms duty cycle, controlled by computer program.

Camera: AndOr, 1024x1024 Peltier-cooled CCD. With f 55 mm Micro-Nikkor-P lens. Images the air-side of the optical fiber coupler of the MCP detectors phosphor screen.

High Voltage: Glassman High Voltage, Inc. EL30N1.5, 30 kV Regulated DC Power

Low ripple < 0.03% at full load

Beam blocker: Hand made from oxygen free copper sheet, mounted to a manual rotary feedthrough.

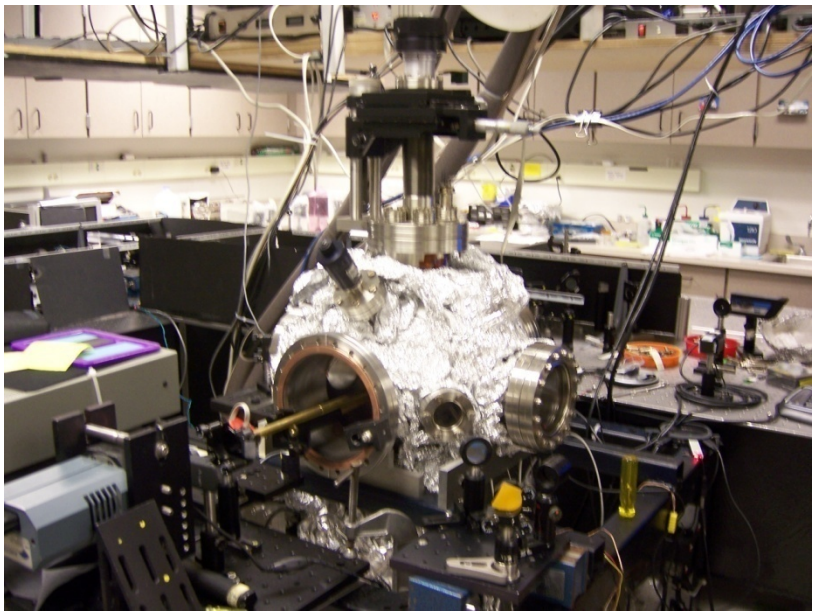

Figure C-4 Vacuum chamber (open to atmosphere) showing XYZ translation stage and partial aluminum foil wrap for bake out.

Vacuum system: ultrahigh vacuum, all seals are conflat, oxygen-free copper. Originally a rotary vane pump and a small turbo pump with a 12" diameter spherical chamber made of 304 SS with opposing 8" horizontal ports for detector and electron gun mounts, and 6" ports on the other horizontal axis, a 6" port at the top for the Vacuum Generators XYZ-theta stage, and long extension downwards with some small ports for gauges on the sides, a 4.5" port for the turbo pump, and at the very bottom an 8" port for an ion pump. There are also 2.5" ports at 45 degrees on the horizontal plane, and two more on the vertical crest at 45 degrees. The rotary vane pump was replaced by a small diaphragm pump after an accident introduced oil into the chamber, resulting in extended downtime and a lot of expense. Operational vacuum was 5e-8 Torr, which was sufficient, but the continual vibrations of the sample holder caused the thin films to deteriorate and disappear after a few weeks. Addition of an ion pump allowed operation with no vibrations, and the samples now last forever. The turbo pump vibrations are large enough that they can be clearly seen in the camera which monitors the pump laser beam.

With the three pump system operation goes: diaphragm on, when it gets to e-0 Torr (2 minutes), turn on Turbo. When pressure gets to e-6 (10 minutes), cover with foil, and start bake out ... start at 35% for 30 minutes, temperature goes to 90 F; then increase to 50% on rheostat, temperature is 170 F in 50 minutes; increase to 70%, temperature is 220 F in 50 minutes, increase to 80% and leave it overnight... by morning the temperature will be ~375 F. The temperature should be reduced slowly, so turn the rheostat down to 50% - but don't remove aluminum foil yet! After 30 minutes the rheostat can be turned to 0% (off), and leave it overnight. In the morning it will be room temp, and the aluminum foil can be removed, and the ion pump started. After about an hour, the gate valve is closed, and if the ion pump holds the pressure at 5e-8, then turn off diaphragm pump and the turbo pump.

Vacuum Generators translation stage: XYZ-theta. Precision stage, micrometers on XY, one turn per mm on vertical, and rotation via manual operation with a locking knob. Sample holder mounts to bottom end of rod, and hence can be adjusted by the stage.

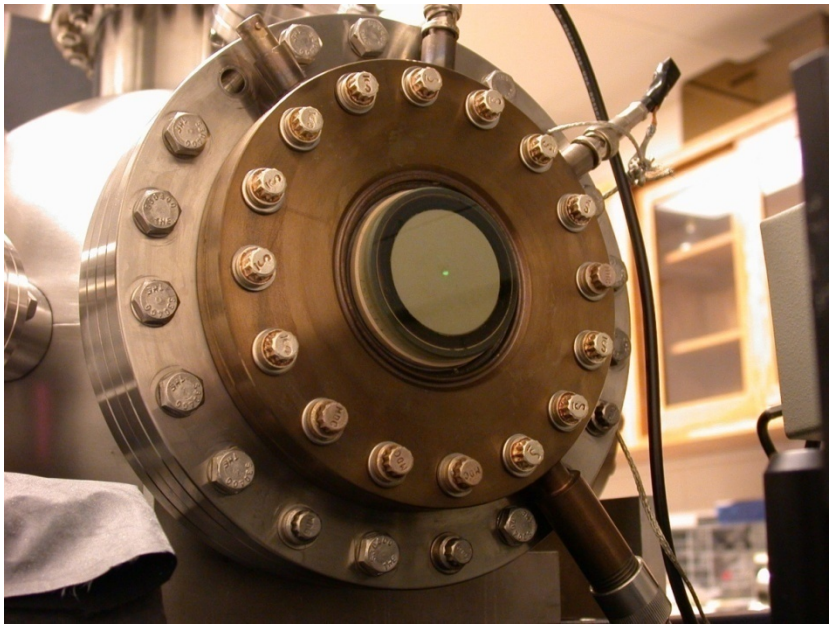

Figure C-5 MCP detector, air side, showing electron beam.

MCP: Burle Long Life image quality chevron microchannel plates, with 40 mm active area. Operated in reverse bias, with the beam encountering negative plate, then grounded plate, then phosphor screen (P20 coating) at positive voltage. Typical is -1500 V/ 0 V/+3000 V. This shields the first detector from low-energy electrons, but does not impede anything that is elastically scattered, or nearly so.

Plates are image quality, 40 mm clear, 12 um center-to-center, 8 degrees bias, chevron pair, 40:1 aspect ratio, uncoated; and amplify up to 10,000 times per plate. They are very linear, and when new, are uniform across the plate, but become non-uniform with use. I mask out the non-uniform spots.

Detector is also sensitive to deep UV, and can track the UV beam that "breaks through" the photocathode. However, it is not sensitive to IR, so scattered laser light is not seen. But positive ions that are generated by gas break down in the electron gun, or in the ion pump are seen, and are a major source of noise. Thus the ion pump is mounted far from

the detector, and has a screen and a grounded deflector plate between them; and the noise declines substantially as vacuum goes from e-7 to e-9 Torr. The noise picks up when the electron gun has voltage applied, and increases rapidly as the voltage exceeds 20 kV unless the sputtered photocathodes are subjected to the 48 hour UV treatment; this appears to be due to particles (debris) escaping from the photocathode surface and edges, and is much worse if the photocathode is recoated without first removing the previous coating from the edges of the lens. This treatment involves ultrasonic cleaning in dilute hydrochloric acid (commercial grade muriatic acid works fine), which must be performed under a fume hood; 20 minutes is sufficient, followed by cold running water rinse for 10 minutes, then regular vacuum cleaning steps of acetone followed by methanol. Then the newly coated, UV treated lens works fine at 30 kV as long as the vacuum pressure is e-9.

MCP plates need to be replaced regularly, as they lose amplification power with extended use, especially in the over-used regions where the central e-beam strikes. In addition exposure to UV leads to little round holes in the amplifiers, as does any hot ion trail that accidentally strikes the plates when activated. Never operate the plates until the vacuum is at least e-6 Torr.

MCP plates are hygroscopic, and tend to crack if not stored correctly due to the glass rims. Rimless plates have very good shelf life, but still wear out with use, and have a new problem if there is insufficient space between the plates ... trapped atmospheric gasses remain even after a bake out, and the applied voltages ionize the trapped gases and these ions are amplified in the hidden rim channels. These really light up, and a portion escapes and causes random brightening and dimming of nearby areas and makes the data unusable. The problem is obvious when the plates are pulled and examined, but appears to be just random noise until the cause has been determined. Lesson: always provide spacers between rimless plates, or just don't use them.

One problem with single plates is the “chicken wire” pattern that shows up in the images; a chevron pair blurs the local detail, but eliminates the chicken wire artifact.

References

[1] X. Liu, D. Du, and G. Mourou. *IEEE J.Quantum Electron.*, vol. QE-**33** (1997) 1706–1716. "Laser Ablation and Micromachining with Ultrashort Laser Pulses"

[2] S.I. Anisimov, B.L. Kapeliovich, and T.L. Perel'man *JETP* **39** (1974) 375. "Electron emission from metal surfaces exposed to ultrashort laser pulses"; M.I. Kaganov, I.M. Lifshitz and L.V. Tanatarov, *JETP* **4** (1957) 173. "Relaxation between Electrons and the Crystalline Lattice"; S.I. Anisimov, A.M. Bonch-Bruevich, M.A. El'yashevich, Y.A. Imas, N.A. Pavlenko, and G.S. Romanov, *Sov. Phys. Tech. Phys*. **11** (1967) 945. "Effect of powerful light fluxes on metals"

[3] P.P. Pronko, P.A. Van Rompay, R.K. Singh, F. Qian, D. Du, and X. Liu, *Mat. Res. Soc. Symp. Proc*. **397** (1996) 45. "Laser Induced Avalanche Ionization and Electron-Lattice Heating of Silicon with Intense Near IR Femtosecond Pulses"

[4] P.P. Pronko, P.A. Van Rompay, C. Horvath, F. Loesel, T. Juhasz, X. Liu, and G. Mourou, *Phys. Rev. B* **58** (1998) 2387. "Avalanche ionization and dielectric breakdown in silicon with ultrafast laser pulses"

[5] Leonid V. Zhigilei, Dmitriy S. Ivanov, *Appl. Surf. Sci.* **248** (2005) 433-439. "Channels of energy redistribution in short-pulse laser interactions with metal targets"

[6] M. Bonn, D.N. Denzler, S. Funk, M. Wolf and S.-S. Wellershoff and J. Hohlfeld, *Phys. Rev. B* **61** (2000) 1101. "Ultrafast electron dynamics at metal surfaces: Competition between electron-phonon coupling and hot-electron transport"

[7] T. Juhasz, H.E. Elsayed-Ali, G.O. Smith, C. Suárez, W.E. Bron, *Phys. Rev. B* **48** (1993) 15488. "Direct measurements of the transport of nonequilibrium electrons in gold films with different crystal structures"

[8] H.E. Elsayed-Ali, T.B. Norris, M.A. Pessot, and G.A. Mourou, *Phys. Rev. Lett*. **58** (1987) 1212. "Time-Resolved Observation of Electron-Phonon Relaxation in Copper"

[9] L. V. Zhigilei and A. M. Dongare, *CMES* **3** (2002) 539. "Multiscale Modeling of Laser Ablation: Applications to Nanotechnology"

[10] G. Mourou and S. Williamson, *Appl. Phys. Lett.* **41** (1982) 44; S. Williamson and G. Mourou, *Phys. Rev. Lett*. **52** (1984) 2364. "Time-Resolved Laser-Induced Phase Transformation in Aluminum"

[11] H.E. Elsayed-Ali, T.B. Norris, M.A. Pessot, and G.A. Mourou, *Phys. Rev. Lett*. **58** (1987) 1212. "Time-Resolved Observation of Electron-Phonon Relaxation in Copper"

[12] X. Zeng, B.Lin, I. El-Kholy, and H.E. Elsayed-Ali, *Surf. Sci*. **439** (1999) 95.

[13] J. C. Williamson, J. Cao, H. Ihee, H. Frey, A. H. Zewail, *Nature*, **386** (1997) 159.

[14] B. L. Qian and H. E. Elsayed-Ali, J. Appl. Phys. **91**, 462 (2002), "Electron pulse broadening due to space charge effects in a photoelectron gun for electron diffraction and streak camera systems"

[15] B. J. Siwick, J. R. Dwyer, R. E. Jordan, and R. J. D. Miller, J. Appl. Phys. **92**, 1643 (2002). "Ultrafast electron optics: Propagation dynamics of femtosecond electron packets"

[16] Mikhail Monastyrskiy, Sergey Andreev, Dmitry Greenfield, Gennadiy Bryukhnevich , Victor Tarasov, and Mikhail Schelev. *SPIE Proceedings*, vol. 5580 (2005) 324-334. "Computer modeling of a sub-femtosecond photoelectron gun with time dependent electric field for TRED experiments"

[17] G. Mourou and W. Knox. *Appl. Phys. Lett.* **36**(8), 523-626 (1980). "A picosecond jitter streak camera"

[18] Nicolas Stenon. *De solido intra solidum naturaliter contento*, Florence, 1669 according to http://reference.iucr.org/dictionary/Law_of_the_constancy_of_interfacial_angles

[19] Steno's law**.** (2009). In *Encyclopædia Britannica***.** Retrieved January 14, 2009, from Encyclopædia Britannica Online**:** http://www.britannica.com/EBchecked/topic/565304/Stenos-law

[20] Essai d'une théorie sur la structure des crystaux, appliquée à plusieurs genres de substances crystallisées [Texte imprimé] / par M. l'abbé Haüy,... Paris : Gogué et Née de La Rochelle, 1784

[21] Image and caption from http://reference.iucr.org/dictionary/Law_of_rational_indices

[22] C. Kittel. Introduction to Solid State Physics. John Wiley & Sons, 7*th* edition, 1996.

[23] Image from http://itl.chem.ufl.edu/2041_f97/lectures/lec_h.html

[24] W.H. Miller. A Treatise on Crystallography. Cambridge, 1839. Available at http://www.archive.org/details/treatiseoncrysta00millrich

[25] William Hallowes Miller. (2009). In *Encyclopædia Britannica*. Retrieved January 22, 2009, from Encyclopædia Britannica Online: http://www.britannica.com/EBchecked/topic/382835/William-Hallowes-Miller

[26] Image from http://en.wikipedia.org/wiki/File:Indices_miller_plan_definition.png

[27] B.E. Warren. X-Ray Diffraction. Dover Publications. Corrected edition, 1990.

[28] Image from http://upload.wikimedia.org/wikipedia/commons/3/3e/Parallelepiped_volume.svg

[29] Weisstein, Eric W. "Cross Product." From *MathWorld*--A Wolfram Web Resource. http://mathworld.wolfram.com/CrossProduct.html

[30] A history of this subject is available from the International Union of Crystallography as a reprint of P.P. Ewald, 50 Years of X-Ray Diffraction, http://www.iucr.org/publ/50yearsofxraydiffraction

[31]Image from http://reference.iucr.org/dictionary/Ewald_sphere

[32] J.D. Jackson. Classical Electrodynamics. John Wiley & Sons, 3*rd* edition, 1998.

[33] Albert Einstein. Relativity. Bonanza Books, New York, 1961.

[34] David B. Williams and C. Barry Carter. Transmission Electron Microscopy. Plenum Press, New York and London, 1996.

[35] A.L. Patterson, Phy. Rev. **56**, 978 (1939). "The Scherrer Formula for X-Ray Particle Size Determination"

[36] The European XFEL and FLASH: http://www.xfel.eu/en/in-comparison/

[37] M. Aeschlimann, E. Hull, J. Cao, C. A. Schmuttenmaer, L. G. Jahn, Y. Gao, H. E. Elsayed-Ali, D. A. Mantell, and M. R. Scheinfein, Rev. Sci. Instrum. **66(2)**, 1000 (1995). "A picosecond electron gun for surface analysis"

[38] Bao-Liang Qian and Hani E. Elsayed-Ali. *Phys. Rev. E.* **65**, 046502 (2002). "An Acceleration Element for Femtosecond Electron Pulse Compression,"

[39] Michael R. Armstrong, Bryan W. Reed, Ben R. Torralva, and Nigel D. Browning *Appl. Phys. Lett.* **90**, 114101 (2007). "Prospects for electron imaging with ultrafast time resolution"

[40] Peter Baum and Ahmed H. Zewail. *Proc Natl Acad Sci USA* **103(44)** 16105–16110 (2006). "Breaking resolution limits in ultrafast electron diffraction and microscopy"

[41] W.E. King, G.H. Campbell, A. Frank, B. Reed, J.F. Schmerge, B.J. Siwick, B.C. Stuart, and P.M. Weber, *J. Appl. Phys.* **97** 111101 (2005). "Ultrafast electron microscopy in materials science, biology, and chemistry."

[42] Christoph T. Hebeisen, Ralph Ernstorfer, Maher Harb, Thibault Dartigalongue,

Robert E. Jordan, and R. J. Dwayne Miller. Optics Letters **31(23)**, 3517 (2006).
"Femtosecond electron pulse characterization using laser ponderomotive scattering"

[43] A. Dolocan , M. Hengsberger , H.J. Neff , M. Barry , C. Cirelli , T. Greber, and J. Osterwalder. Unpublished draft article dated September 29, 2004.
"Electron-Photon Pulse Correlator Based on Space-Charge Effects in a Metal Pinhole"

[44] H. Park, Z. Hao, X. Wang, S. Nie, R. Clinite, and J. Cao. Rev. Sci. Instrum. **76**, 083905 (2005)
"Synchronization of femtosecond laser and electron pulses with subpicosecond precision"

[45] H. Zewail, Annu. Rev. Phys. Chem. **57**, 65–103 (2006).
"4D ultrafast electron diffraction, crystallography, and microscopy."

[46] Steve Williamson, private communication.

[47] L. Cavalieri, D. M. Fritz, S. H. Lee, P. H. Bucksbaum, D. A. Reis, J. Rudati, D. M. Mills, P. H. Fuoss, G. B. Stephenson, C. C. Kao, D. P. Siddons, D. P. Lowney, A. G. MacPhee, D. Weinstein, R. W. Falcone, R. Pahl, J. Als-Nielsen, C. Blome, S. Dursterer, R. Ischebeck, H. Schlarb, H. Schulte-Schrepping, Th. Tschentscher, J. Schneider, O. Hignette, F. Sette, k. Sokolowski- Tinten, H. N. Chapman, R. W. Lee, T. N. Hansen, O. Synnergren, J. Larsson, S. Techert, J. Sheppard, J. S. Wark, M. Bergh, C. Caleman, G. Huldt, D. van der Spoel, N. Timneanu, J. Hajdu, R. A. Akre, E. Bong, P. Emma, P. Krejcik, J. Arthur, S. Brennan, K. J. Gaffney, A. M. Lindenberg, K. Luening, and J. B. Hastings. Phys. Rev. Lett., **94**:114801, (2005). "Clocking femtosecond x-rays."

[48] First attempted in summer 2004; it failed because the TEM apertures used as targets were made from copper with an unknown coating. Laser ablation of the coating generated tremendous noise. Another experiment intervened while Gold TEM apertures were ordered, and when the attempt was next made in November 2004 it was successful on the first try. Subsequent efforts were toward understanding the mechanism, and improving the electron gun performance.

[49] Method due to John Nees of CUOS, who uses a similar technique for an all-optical experiment.

[50] Codrin is a much-appreciated colleague and a research scientist in the Roy Clarke group.

[51] David A. Reis. *Solid State Commun*. 136 (2005) 564-565. "A film of picosecond vibrations of a film", and H. Park, X. Wang, S. Nie, R. Clinite, J. Cao. *Solid State Commun*. **136** (2005). "Direct and real-time probing of both coherent and thermal lattice motions"

[52] Conducted by my colleague, Vladimir Stoica. The setup is described in:
Vladimir A. Stoica, Yu-Miin Sheu, David A. Reis, and Roy Clarke. Optics Express **16(4)** 2322-2335 (2008). "Wideband detection of transient solid-state dynamics using ultrafast fiber lasers and asynchronous optical sampling"

[53] Table 7.9; Michael De Podesta. Understanding the properties of matter, Second Edition. CRC Press, 2002.

[54] N. Del Fatti, C. Voisin, D. Christofilos, F. Valle, C. Flytzanis. *J. Phys. Chem. A* **2000(104)** 4321-4326.

[55] "Taking Ultrafast Snapshots of Material Changes"
https://www.llnl.gov/str/NovDec08/pdfs/11.08.1.pdf

[56] K. S. Novoselov, S. V. Morozov, T. M. G. Mohinddin, L. A. Ponomarenko, D. C. Elias, R. Yang, I. I. Barbolina, P. Blake, T. J. Booth, D. Jiang, J. Giesbers, E. W. Hill, A. K. Geim. *Physica Status Solidi (b)* **255**: 4106 – 4111 (2007). "Electronic properties of graphene"

[57] ImageJ; available at http://rsb.info.nih.gov/nih-imageJ; developed by Wayne Rasband, National Institutes of Health, Bethesda, MD.